LBNL-43409

ERNEST ORLANDO LAWRENCE
BERKELEY NATIONAL LABORATORY

Investigations of the Ground-State Hyperfine Atomic Structure and Beta Decay Measurement Prospects of ^{21}Na with Improved Laser Trapping Techniques

Mary A. Rowe

Nuclear Science Division

May 1999

Ph.D. Thesis

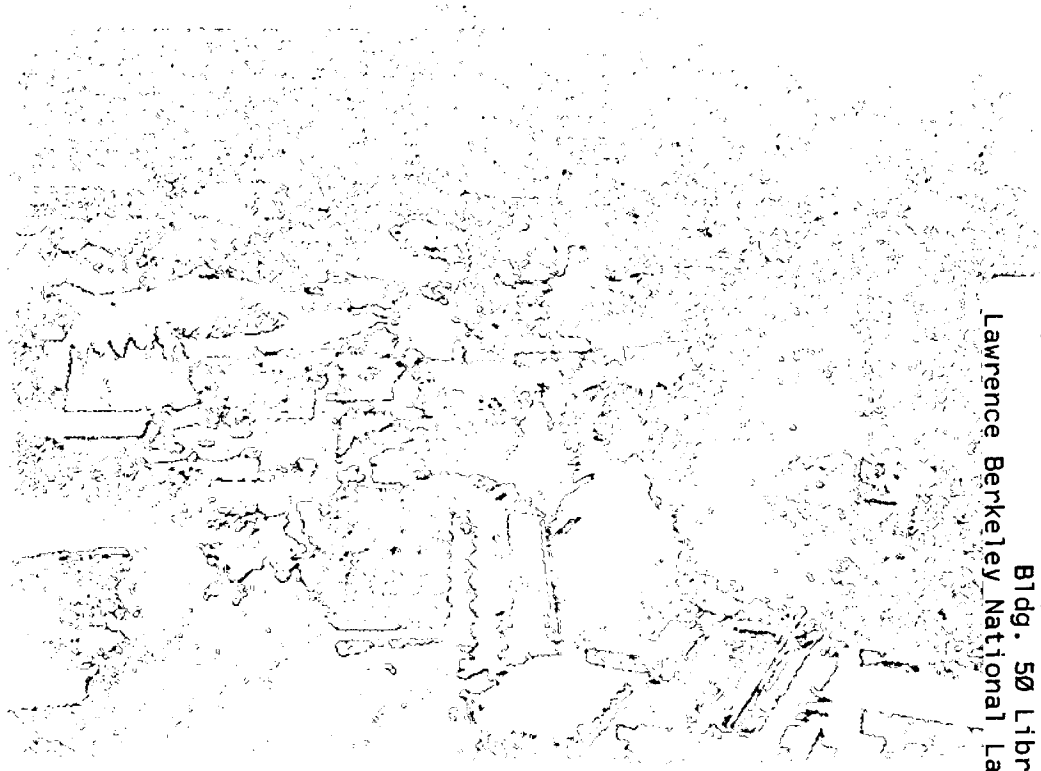

DISCLAIMER

LBNL-43409

Investigations of the Ground-State Hyperfine Atomic Structure and Beta Decay Measurement Prospects of ^{21}Na with Improved Laser Trapping Techniques

Mary A. Rowe
Ph.D. Thesis

Department of Physics
University of California, Berkeley

and

Nuclear Science Division
Ernest Orlando Lawrence Berkeley National Laboratory
University of California
Berkeley, CA 94720

May 1999

This work was supported by the Director, Office of Energy Research, Office of High Energy and Nuclear Physics, Division of High Energy Physics, of the U.S. Department of Energy under Contract No. DE-AC03-76SF00098.

Investigations of the Ground-State Hyperfine Atomic Structure and Beta Decay Measurement Prospects of ^{21}Na with Improved Laser Trapping Techniques

by

Mary Anderson Rowe

B.S. (California Institute of Technology) 1992

A dissertation submitted in partial satisfaction of the
requirements for the degree of
Doctor of Philosophy

in

Physics

in the

GRADUATE DIVISION
of the
UNIVERSITY of CALIFORNIA at BERKELEY

Committee in charge:

Professor Stuart J. Freedman, Chair
Professor Eugene D. Commins
Professor Joseph Cerny

Spring 1999

Investigations of the Ground-State Hyperfine Atomic Structure and Beta Decay Measurement Prospects of ^{21}Na with Improved Laser Trapping Techniques

Mary A. Rowe

Abstract

Investigations of the Ground-State Hyperfine Atomic Structure and Beta Decay Measurement Prospects of ^{21}Na with Improved Laser Trapping Techniques

by

Mary Anderson Rowe

Doctor of Philosophy in Physics

University of California at Berkeley

Professor Stuart J. Freedman, Chair

This thesis describes an experiment in which a neutral atom laser trap loaded with radioactive ^{21}Na was improved and then used for measurements. The sodium isotope (half-life = 22 sec.) is produced on-line at the 88″ cyclotron at Lawrence Berkeley National Laboratory. We developed an effective magnesium oxide target system which is crucial to deliver a substantive beam of ^{21}Na to the experiment. Efficient manipulation of the ^{21}Na beam with lasers allowed 30,000 atoms to be contained in a magneto-optical trap. Using the cold trapped atoms, we measured to high precision the hyperfine splitting of the atomic ground state of ^{21}Na. We measured the $3S_{1/2}(F = 1, m = 0)$ - $3S_{1/2}(F = 2, m = 0)$ atomic level splitting of ^{21}Na to be 1,906,471,870±200 Hz. Additionally, we achieved initial detection of beta decay from the trap and evaluated the prospects of precision beta decay correlation studies with trapped atoms.

To my parents, Virginia and Richard Rowe, and my husband Art Zirger.

Contents

List of Figures

List of Tables

Acknowledgements

Many people contributed to the work presented in this thesis. First, I would like to thank my advisor, Professor Stuart Freedman, for the opportunity to work on this project and the support to do it. I had the chance to work with some excellent young scientists as a graduate student. Dr. Song-Quan Shang showed me the ropes when I was starting out. Dr. Brian Fujikawa was always there to help with obscure detection electronics problems. I worked on a day-to-day basis with Dr. Gerald Gwinner and Dr. Paul Vetter. Our long discussions ranging from specific experimental problems to general physics made work enjoyable. Their help with the project was critical to getting it to work, as well. During my graduate years I worked both on the Berkeley campus and at the 88″ Cyclotron at Lawrence Berkeley National Laboratory. Both places have talented and friendly support staffs, and I thank them for all their help in building the experiment. I also had the pleasure of interacting with my fellow Berkeley graduate students. Among them, I would like to acknowledge Anh-Tuan Nguyen, Chris Bowers, and Juergen Reich. Our discussions filled with "I don't know's" taught me so much. I would like to thank my roommate during most of graduate school, Jeannie Barrett, for all the fun we had together. I want to thank my parents for their love and encouragement throughout the years. Unusual in today's busy world, my parents set aside so much time to nurture and teach their children. Games of Krypto with my dad and solving tough math problems with my mom are just two of many examples that remind me of how my parents have always been there. Finally, I would like to thank my husband Art for his level-headed advice which kept all things in perspective, his friendship, and his love.

Chapter 1

Introduction

A striking feature of the weak interaction is that it violates discrete spatial symmetries. Physicists try to isolate the few simple principles of nature and from these derive physical laws. Symmetries, such as parity, play an important part in this process, often forming the basis of a theory. Parity is sometimes called the mirror symmetry because it is equivalent to a mirror transformation plus a rotation. Formally it transforms all spatial coordinates to negative themselves, $\vec{r} \rightarrow -\vec{r}$. If someone is watching a fundamental process can they tell if it is viewed with a mirror? The answer is yes for weak interaction processes because it violates parity symmetry. Until 1956 it was assumed that parity symmetry was good for all interactions and it formed part of the underlying structure of the theory. Then a series of experiments showed that not only is parity violated in the weak interaction but that it seems to be violated in a maximum manner. Today the level of sophistication of the theory which is a renormalizable quantum field theory based on a spontaneously broken non-Abelian gauge symmetry has increased but some of the basic questions remain. Why does the weak interaction seem to break parity symmetry completely? Does the weak interaction indeed break parity symmetry completely? Theories of higher unification require more forms of the weak interaction. Do these exist? The laser trapping experiment described in this thesis seeks to improve experimental techniques aimed at studying the weak interaction in order to answer these questions.

1.1 A Short History

When Fermi originally wrote down the effective Hamiltonian for nucleon beta decay [1] he assumed a current-current vector coupling in analogy with the electro-magnetic coupling,

$$H_{int} = \frac{G_F}{\sqrt{2}}(\overline{\psi}_p \gamma_\mu \psi_n)\,(\overline{\psi}_e \gamma^\mu \psi_\nu) + h.c. \; . \tag{1.1}$$

The first bracketed part, the nucleon current, changes neutron to proton inside the nucleus and the second bracketed part, the lepton current, creates an electron and an antineutrino. This process describes beta decay with an electron (the hermitian conjugate term, *h.c.*, allows decay with a positron). Neutron decay, $n \rightarrow p + e^- + \overline{\nu}_e$, is the simplest example. In the non-relativistic limit, which is well met by nucleon decays, the vector nucleon current in Equation 1.1 reduces to $\chi_p^\dagger I \chi_n$ where the χ_p and χ_n are 2-component spinor wave functions for the proton and neutron respectively. This current allows no change in angular momentum between the parent and daughter nuclei. These decays are Fermi type and have $J_i = J_f$. It was soon realized that an additional interaction was necessary to allow for observed decays where the angular momentum changed by one unit. The interaction in Equation 1.1 was generalized to

$$H_{int} = \frac{G_F}{\sqrt{2}}\left[\sum_i C_i(\overline{\psi}_p O_i^\dagger \psi_n)\,(\overline{\psi}_e O_i \psi_\nu) + h.c.\right]. \tag{1.2}$$

The operator O_i can be 1 called scalar(S), γ_5 called psuedoscalar(P), γ_μ called vector(V), $\gamma_\mu\gamma_5$ called axial vector(A) or $\gamma_\mu\gamma_\nu$ called tensor(T). The scalar nucleon current reduces to $\chi_p^\dagger I \chi_n$ in the non-relativistic limit and is a Fermi type operator. The psuedoscalar current reduces to 0 in the non-relativistic limit. Both the axial and tensor nucleon currents reduce to $\chi_p^\dagger \vec{\sigma} \chi_n$. These A and T terms allow decays, called Gamow-Teller, with $\Delta J = 0, \pm 1$ but not $J_i = 0 \rightarrow J_f = 0$ decays. Since both $J_i = 0 \rightarrow J_f = 0$ and $\Delta J = 1$ decays exist at least one Gamow-Teller term and one Fermi interaction term are needed. In fact information from the decay rates of many different nuclei showed that the strengths of the Fermi and Gamow-Teller interactions were about the same. Experiments looking for interference between A and T or S and V, called Fierz interferences, in beta spectrums found none. This indicated that either A or T was the dominant Gamow-Teller contributor and either S or V was the dominant Fermi contributor.

To determine the interaction structure the correlation between emission directions of the beta and neutrino was measured. Of course the neutrino was not observed directly but

its motion relative to the beta was deduced from the energy spectrum of the daughter ion. Depending on the interaction type the beta and neutrino will tend to be emitted parallel of anti-parallel to each other. In Fermi type decays a scalar term causes the leptons be preferentially emitted opposite each other while a vector term results in preferential parallel emission. For Gamow-Teller type decays the emission is somewhat antiparallel (parallel) for A (T) type interactions. Even though today the Standard Model of the weak interactions has settled on V and A interaction couplings, experiments of this type are still important. Various extensions to the Standard Model predict small amounts of T and S. By making very precise measurements of the beta-neutrino correlation their possible contributions can be detected. With a source of laser trapped radioactive atoms precision electron-neutrino measurements can be made. The daughter ion and beta from the decay emerge from the trap with their initial direction and energy preserved. Given this information the neutrino's emission direction can be deduced and the correlation determined. Historically, early beta-neutrino measurements were in error. Work in the Gamow-Teller decay of ^{6}He [2] indicated a T contribution. The mixed decay of ^{19}Ne [3] indicated a combination of interactions, either V and A or S and T. Given the ^{6}He results the ^{19}Ne measurement was interpreted to mean that a scalar term contributed to the interaction.

Other weak processes were also being investigated in terms of a current-current picture. Experiments on muon decay and muon capture pointed to V and A structure. Although it was noticed that the coupling constants for beta decay and muon processes were tantalizing similar the structures appeared different. More deduction on the form and unity of the weak interaction needed the flood of experimental data which followed the discovery of parity violation in the weak interaction.

In 1956 Lee and Yang [4] suggested that there existed no experimental evidence that parity is conserved in the weak interaction. A more general interaction which included parity violating terms was given,

$$H_{int} = \frac{G_F}{\sqrt{2}} \left[\sum_i (\overline{\psi}_p O_i^\dagger \psi_n) \, (\overline{\psi}_e O_i (C_i - C_i' \gamma_5) \psi_\nu) \; + \; h.c. \right]. \tag{1.3}$$

Parity violating terms, those with the C_i' coefficients, were added. Soon after, parity violation was found in the beta decay of polarized ^{60}Co [5]. C.S. Wu observed a "large asymmetry effect" in the direction the decay electrons were emitted relative to the initial nuclear spin. Figure 1.1 shows why this observation of the beta-asymmetry indicated parity violation. The nuclear polarization is represented by the spinning cylinder. The decay electrons were

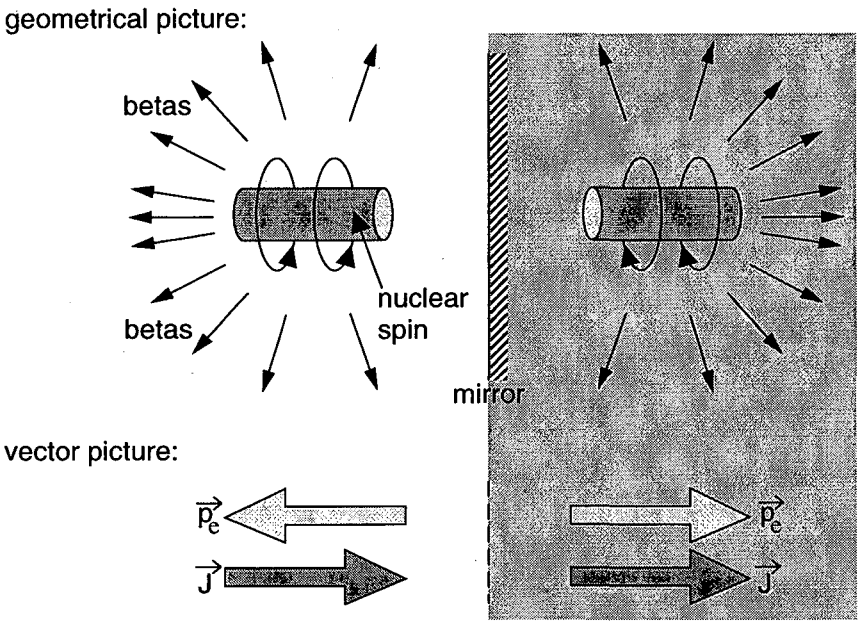

Figure 1.1: Parity violation in Wu's experiment. $\vec{J}$ is the direction of the initial nuclear spin and $\vec{p}_e$ is the preferred emission direction of the betas. The left side of the picture represents the physics in the regular world and the shaded right side shows the parity transformed world.

preferentially emitted in the direction opposite the nuclear polarization, represented by more beta arrows in that direction. The shaded right half of the picture shows the result of a parity transformation on the left side. The parity transformation is accomplished by reflecting the left side in the mirror and then making a trivial 180 degree rotation about an axis perpendicular to the mirror plane. Referring to the vector picture, the physics in the two reference frames is clearly different. Formally the fact that the psuedoscalar $< \vec{J}_i \cdot \vec{p}_e > \neq 0$ signals parity violation.

Wu's experiment showed a large amount of parity violation. Since then many more detailed experiments have shown parity violation consistent with the maximum allowed. The Standard Model today contains this maximum parity violation inserted by hand to agree with experiment. The interaction currents have the form $\gamma_\mu(1-\gamma_5)$ which are referred to as left-handed because the resulting leptons have left-handed helicity. Their spin is antiparallel their momentum. Extensions to the Standard Model, seeking to explain the left-handed nature on more fundamental grounds, incorporate higher symmetry groups. Some of these models have small amounts of right-handed currents. Precise beta-asymmetry measurements are sensitive to deviations from maximum parity violation. Small amounts of right-handed currents reduce the beta-asymmetry from the strictly left-handed prediction. In Section 1.2 it is discussed how trapped atoms can help make very precise measurements in order to detect small contributions from right-handed currents.

Soon after Wu's experiment it was found that parity was violated in the $\pi^+ \rightarrow \mu^+ + \nu_\mu \rightarrow e^+ + \overline{\nu}_\mu + \nu_e$ decay chain [6][7] and in polarized neutron decay[8] as well. An experiment by Goldhaber *et al.* [9] showed that neutrinos were 100% left-handed polarized within experimental errors. The large amount of parity violation observed indicated close to maximal violation in the lepton current, ie. $C_i = C_i'$. The left-handed nature of the neutrinos in Goldhaber's experiment combined with the left-handed electrons implied by Wu's experiment indicated an axial vector component of the nucleon current. The neutron studies pointed to a nearly V-A nucleon interaction. The muon results showed V-A structure in its analogous interaction as well. Also, a measurement of the electron-neutrino correlation in ^{35}Ar[10], although not parity violating, indicated a V component of the interaction which contradicted the earlier S indicating experiments. Now the theory was ready for refinement.

Equipped with the dramatic parity violating results, in 1958 Feynman and Gell-

Mann [11] proposed a universal, V-A (left-handed), charged weak current:

$$J_\mu = \overline{\psi}_p \gamma_\mu (1-\gamma_5)\psi_n + \overline{\psi}_\nu \gamma_\mu (1-\gamma_5)\psi_e + \overline{\psi}_\nu \gamma_\mu (1-\gamma_5)\psi_\mu + i[\varphi_\pi^* T^+ \nabla_\mu \varphi_\pi - (\nabla_\mu \varphi_\pi)^* T^+ \varphi_\pi] \tag{1.4}$$

where the interaction is

$$H_{int} = \frac{G_F}{\sqrt{2}} J_\mu J^\mu. \tag{1.5}$$

In Equation 1.4 T^+ is the isospin raising operator and the pion field, φ_π, is the an isospin triplet, $\begin{pmatrix} \varphi_{\pi^+} \\ \varphi_{\pi^0} \\ \varphi_{\pi^-} \end{pmatrix}$, of the three pions.

This formulation was a major simplification. The fundamental particles now had all the same current form and the multiple couplings from the previous description were eliminated. Now C_i=C_i', C_P=C_S=C_T=0, and C_V=C_A=1. In the special case of $0^+ \rightarrow 0^+$ beta decay where only the vector coupling contributes it was found that the coupling strengths were the same for the decay of many different nuclei. Also the beta decay vector coupling strength found was only slightly different from the coupling constant for muon decay. To explain the consistency of different nuclei the idea of a conserved vector current (CVC) was introduced in the same paper. CVC states that the vector coupling constant is a constant independent of the details of the make-up of the decaying particle. Mathematically, a conserved vector current results in a conserved weak charge in the same way conservation of electromagnetic current results in a conserved electric charge. CVC requires the addition of a pion current, the final current term above. The pion must carry a weak charge so that the weak coupling strength is not renormalized as the nucleons interact strongly in the nucleus. The reaction $\pi \rightarrow e + \nu$ was predicted by this interaction at a level at which experiments were sensitive. At the time it hadn't been observed, a bit of a problem. Pion beta decay, $\pi^+ \rightarrow \pi^0 + e^0 + \nu_e$ was also predicted with a small branching ratio. Other new weak processes such as electron-electron scattering and electron-neutrino scattering were discussed as future experiments.

Although experiments provided the guidance for writing down a unified V-A interaction it was the strong theoretical push for simplicity and symmetry that lead to the creation of such a wide ranging theory. To be so specific and simple can never be demanded by experiments but is searched for by theory as a way to understand nature. It is interesting to note in this light that the neutron experiments were indicating a nucleon current more

like V-1.3A. But the simplicity was left to stand and axial current renormalization effects were conjectured. Feynman and Gell-Mann discussed the origin of the $(1-\gamma_5)\gamma_\mu$ coupling as resulting naturally from a two component formulation of the Dirac field. By demanding only non-derivative couplings between these two component spinors and that all particles couple with the same handedness a V-A or V+A theory is determined. Experiments pick V-A. Other theorists tried to explain the fundamental nature of V-A other ways . The notion of chirality invariance, the theory being invariant under $\psi \rightarrow \gamma_5\psi$ also leads to V-A and V+A interactions.

By the mid 1960's the V-A form of the weak interaction was well accepted[12]. The earlier results with ^{6}He that indicated a T interaction were shown to be wrong and the pion decays, $\pi \rightarrow e+\nu$ and $\pi^+ \rightarrow \pi^0+e^0+\nu_e$ had been observed and the branching ratios agreed with the conserved vector current theory. Experiments that measured the polarization of electrons and positrons from beta decays agreed with the prediction of the V-A model. But a current-current interaction Hamiltonian is not a fundamental theory. It gives correct answers when a first order pertabative expansion is taken but when higher order terms are computed the answers become infinite. The current-current interaction is fine for calculating beta decays which are relatively low energy and it will be referred to in this thesis. Here the theoretical developments which changed the theory from a phenomenological current-current interaction to one of fundamental soundness are briefly discussed and the basics of the underlying theory which are utilized later in the thesis are mentioned.

In 1967 Weinberg and Salam proposed what is now called the Standard Model of the weak interaction. It combined the idea of spontaneous symmetry breaking which gave the intermediate bosons masses and the idea of gauge invariance based on the group $SU(2)_L \times U(1)$. The theory has four intermediate gauge bosons. Three are from SU(2)$_L$ and are W^+, W^0 and W^-. The other one is the U(1) gauge boson, B^0. The W^0 and B^0 mix to give the physical massive Z^0, the mediator of the then predicted neutral weak interaction, and γ, the photon. In 1971 't Hooft proved the theory is renomalizable and therefore a consistent theory. Soon after the predicted neutral weak currents were detected. Another highlight was in the early 1980's when the physical intermediate weak bosons were created and observed at CERN. The Standard Model has now been tested in detail without major discrepancies.

Beta decay is a charged weak current process mediated by charged bosons. In

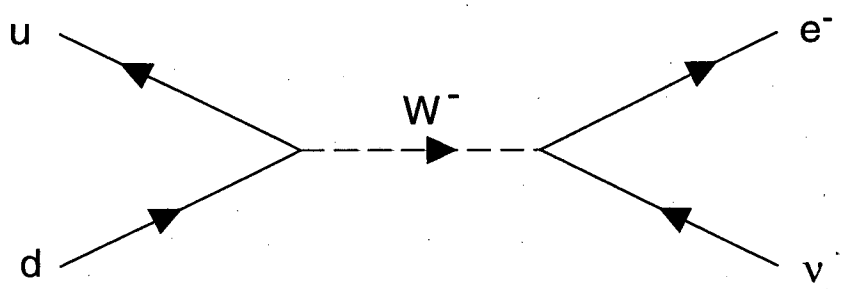

Figure 1.2: Tree level diagram for beta decay.

terms of the fundamental particles the charged weak Lagrangian is,

$$L_{chargedweak} = \frac{-2g}{\sqrt{2}} \sum_i \overline{\psi}_i \gamma^\mu (T^+ W_\mu^+ + T^- W_\mu^-) \psi_i \tag{1.6}$$

where

$$\psi_i = \begin{pmatrix} \nu_i \\ l_i^- \end{pmatrix}_L \text{ and } \begin{pmatrix} u_i \\ d_i' \end{pmatrix}_L . \tag{1.7}$$

The weak isospin raising (lowering) operator T^+ (T^-) connects the lower (upper) component of ψ_i to the upper (lower) component of $\overline{\psi}_i$. The subscript, L, indicates that only left-handed particles, $\phi_L = \frac{1}{2}(1-\gamma_5)\phi$, participate in the interaction. The ψ_i can be a lepton or a quark isodoublet. For the leptons i is summed over e, μ and τ. The quark isodoublets are charge +2/3 uplike quarks paired with charge -1/3 downlike quarks. The three quark isodoublets are $\begin{pmatrix} u \\ d' \end{pmatrix}$, $\begin{pmatrix} c \\ s' \end{pmatrix}$ and $\begin{pmatrix} t \\ b' \end{pmatrix}$. The weak quark eigenstates, d_i', are related to the strong mass eigenstates, d, s and b, by the Cabibbo-Kobayashi-Maskawa (CKM) matrix,

$$\begin{pmatrix} d' \\ s' \\ b' \end{pmatrix} = \begin{pmatrix} V_{ud} & V_{us} & V_{ub} \\ V_{cd} & V_{cs} & V_{cb} \\ V_{td} & V_{ts} & V_{tb} \end{pmatrix} \begin{pmatrix} d \\ s \\ b \end{pmatrix} \tag{1.8}$$

The tree level Feynman diagram of beta decay is shown in Figure 1.2. The $n \to p$ reaction at the quark level is $d \to u$. Since the mass of the W boson is so large, about 80 GeV, compared to the momentum transfer in beta decay, a few MeV, the contribution of

the W boson propagator becomes just $\frac{1}{m_W^2}$. The interaction Hamiltonian is then,

$$H_{int} = \frac{G_F}{\sqrt{2}} V_{ud} \overline{u} \gamma^\mu (1 - \gamma_5) d \, \overline{e} \gamma_\mu (1 - \gamma_5) \nu \; + \; h.c. \tag{1.9}$$

where

$$\frac{G_F}{\sqrt{2}} = \frac{g^2}{8 m_W^2}. \tag{1.10}$$

The CKM matrix element $V_{ud} \approx .97$ gives the weight of the weak coupling of u and d quark accounting for the slight difference in nucleon and muon vector strength first noted in the 1950's.

The Standard Model's solution to parity violation is to insert by hand the condition that only left-handed particles interact weakly. This solution is not very satisfactory as it gives no fundamental reason for maximal parity violation. The hope is to have that aspect naturally fall out of a formulation in terms of a higher symmetry group. These extensions to the Standard Model can introduce small amounts of new interactions. Experimental clues are needed. One approach is to hunt for small deviations from the value predicted by the Standard Model for correlation parameters in beta decay.

1.2 Laser Trapping Applied to Tests of the Standard Model

The goal of this ongoing experiment is to use the new technology of laser trapping of neutral atoms to improve the accuracy of beta decay measurements to test the Standard Model. In Section 1.1 two important beta decay correlations were mentioned, the beta-asymmetry and the beta-neutrino correlations. There are many others as well. The neutrino-asymmetry correlation describes the emission direction of the neutrino relative to the initial spin. The triple correlation described by the D coefficient, $\vec{J}_i \cdot (\vec{p}_e \times \vec{p}_\nu)$ is time reversal violating. If the polarization, $\vec{\sigma}$, of the decay beta is measured even more correlations are possible. The beta polarization alone is important and is sensitive to right-handed currents. Another correlation, the polarization asymmetry, measures the relative polarization of the betas emitted parallel and antiparallel to the direction of the initial nuclear spin. The triple correlation $\vec{\sigma} \cdot (\vec{J}_i \times \vec{p}_e)$ is another time reversal violating parameter. Precise measurements of the beta energy spectrum also contribute to testing the Standard Model. Present techniques for making these measurements are becoming limited and a new approach is needed to push these tests to higher accuracy and precision.

Radioactive atoms confined in a laser trap may provide a solution to the difficult task of improving current beta decay measurements. The magneto-optical trap (MOT) discussed in this thesis confines a single species of atoms to a small sphere less that one millimeter in diameter within a vacuum system, providing very good geometry for an experiment. Lasers are resonant with the trapped isotope only resulting in an isotopically pure source. The ball of atoms in the trap has a low density, $\approx 10^{10}$ atoms/cm^3, and is surrounded by a good vacuum in the low 10^{-10} torr range which essentially eliminates source scattering. In this situation both the beta particle and the recoiling daughter ion from the beta decay are available for study with their momenta unperturbed. By knowing the momentums of the positron and daughter ion the complete kinematics of the decay including the neutrino's momentum can be reconstructed. Optical pumping techniques can be utilized on this low density source to providing highly polarized nuclei. The option of loading an auxiliary magnetic trap which holds only one polarization with the cooled atoms from a MOT exists as well. Also optical diagnostics of the polarization can be used to determine the polarization precisely. Work with these goals in mind, probing the hyperfine structure of ^{21}Na, will be discussed in Chapter 5.

One limitation of this laser trapping technique is that it is confined to elements with strong cycling transitions at convenient laser wavelengths. Only alkali atoms are easily trapped, although with additional effort stable atoms including metastable noble gases and alkaline earths have also been trapped. Because only a few precise correlation measurements exist some good measurements on a few new isotopes will tremendously increase knowledge. Right now laser trapping on the radioactive atoms, ^{21}Na, ^{37}K [13], ^{38m}K [13] and ^{82}Rb [14], is being done with beta decay measurements as the goal. The benefits of laser traps for decay correlation measurements can be appreciated in light of the restrictions of previous experiments.

One technique used for beta decay studies is to inject the gasous activity of interest into a cell. Typical cell dimensions are from a few centimeters to tens of centimenters. With such a large source compared to the detector size careful Monte Carlo simulations are needed to model the system. In the latest version of a highly precise measurement of the beta-asymmetry parameter in ^{19}Ne [15] a small mylar cell was used and the detectors were placed far from the cell so that the geometry would be better defined. Another worry with cells are the uncertainties with the polarization. In the ^{19}Ne case nearly perfectly polarized nuclei emerge from a Stern-Gerlach magnet and enter the cell. Uncertainties in the rate

of sticking to the cell wall and depolarizing wall collisions limit the precision with which the polarization can be known. Background contaminant activity can also exist in the cell. Depending on the production process this can contribute a few percent to the count rate and corrections for it must be made.

Another category of experiments involve implanting activity at a few tens of keV onto thin backing foils to hold it. Here the geometry can be quite good with the implanted area less than 1 mm^2. But scattering of the beta off of the backing can amount to many percent corrections which must be estimated to interpret the results. Polarization is also difficult. The activity can be created polarized via a reation with a polarized beam and then maintained in a weak holding field. These polarizations are small, a few percent, and decay in a few seconds. Absolute polarization can not be measured accurately and must be inferred from beta-asymmetries in other beta decay branches. Typically these branches have small branching ratios so the data rate in the experiment suffers. A way to get high polarizations is to use low temperature nuclear orientation. An iron foil is used and placed in a high magnetic field, about 0.1 Tesla and made very cold, about 10mK. Some fraction of the implanted nuclei end up in good sites in the magnetized iron lattice where the hyperfine field can be tens of Tesla. Boltzman statistics give very high polarizations for the successful nuclei but the average polarization is hard to calculate to better than a few percent. Attempts have been made to make comparisons between the decays of different isotopes in the same lattice to get around calculation uncertainties. But concerns remain about whether the different isotopes are located in similiar lattice sites. Finally there is no guarantee that the implanting beam is contaminant free. Errors from contaminants with half-lives similar to the studied activity are hard to eliminate.

Beam experiments, mainly with neutrons, have contributed immensely to studies of beta decay correlations. Cold neutrons from a reactor follow wave guides to the experiment where the beam passes through a detector array. The neutrons can decay anywhere along their path in the detector and this must be modeled with the detector acceptances to interpret the results. Polarized neutrons are made by reflection off of a magnetic mirror polarizer. The polarizations are determined with a second analyzer magnetic mirror to accuracies of about 0.5%. But problems with the delicate process of guiding the polarization, such as stray magnetic fields, make these determinations tricky. Background rates of a few percent are typical in these experiments and must be subtracted. The level of precision of the various current neutron experiments is about 1%. But the four present precision

measurements of the neutron beta-asymmetry parameter [16][17][18][19] are in disagreement (χ^2=9 for n=3). More understanding of the systems' systematics is clearly needed.

Chapter 2

Beta Decay of ^{21}Na

2.1 Nuclear Decay Scheme

The work of this thesis centers around a radioactive isotope of sodium, ^{21}Na. It decays by positron emission, $^{21}\text{Na} \rightarrow ^{21}\text{Ne} + e^+ + \nu_e$, with a half-life of 22 seconds. As can be seen by referring to Figure 2.1, the largest branch of the decay goes to the ground state of ^{21}Ne while a small 5% branch goes to the first excited state. The electron capture branch is very small, about 0.09%. Figure 2.1 shows the spins and parities of the levels. For instance the ground state of ^{21}Ne, labeled $3/2^+$, has spin 3/2 and positive parity. The endpoint energy of the beta is 2.5 MeV for the main branch. The exact values with errors of the decay properties of ^{21}Na are summarized in Table 2.1.

The $3/2^+$ state of ^{21}Na and the $3/2^+$ state of ^{21}Ne form an isospin doublet. The

Property	Symbol	Value	Reference
total half-life	$t_{1/2}^{tot}$	22.47±0.03 sec	[20]
main $3/2^+ \rightarrow 3/2^+$ transition branch	BR_{main}	94.9±0.2%	[21]
side $3/2^+ \rightarrow 5/2^+$ transition branch	BR_{side}	5.0±0.2%	[21]
electron capture branching ratio	BR_{EC}	0.087%	[20]
Q-value	Q_{EC}	3547.460±0.701 keV	[22]
beta endpoint total energy	E_0	3036.31±0.70 keV	[22]
beta endpoint kinetic energy	E_{kin}	2525.31±0.70 keV	[22]
gamma energy	E_γ	350.725±0.008 keV	[23]

Table 2.1: Decay properties of ^{21}Na.

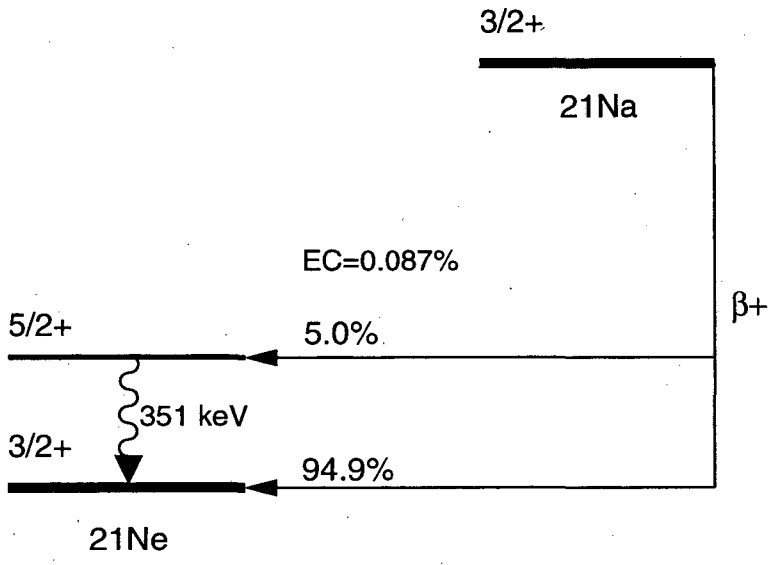

Figure 2.1: Nuclear decay scheme for ^{21}Na.

ground state ^{21}Na nucleus with its 11 protons and 10 neutrons is the upper member of the doublet, $T = \frac{1}{2}, m_T = +\frac{1}{2}$. The lower member, $T = \frac{1}{2}, m_T = -\frac{1}{2}$, is the ground state of ^{21}Ne with 11 neutrons and 10 protons. The Fermi matrix element $< 1 >=< \psi_f|T^-|\psi_i >$, where T^- is the isospin lowering operator, enters into positron decay calculations. To the degree that the isospin assignments are good the Fermi matrix element for the main branch is

$$\begin{aligned} < 1 > \; &= < \psi_f|T^+|\psi_i > \; = < T = \frac{1}{2}, m_T = -\frac{1}{2}|T^-|T = \frac{1}{2}, m_T = +\frac{1}{2} > \\ &= \sqrt{T(T+1) - m_{t_i} m_{t_f}} \; = \; 1. \end{aligned} \tag{2.1}$$

Of course for the side branch the value of $< 1 >$ is zero since the operator T^- is a scalar in coordinate space and doesn't connect states of different spin. The simple isospin structure makes the contributions of the two allowed terms in the ^{21}Na system large. Complicated forbidden terms and the effects of isospin mixing contribute only with very small corrections so fundamental weak interaction parameters can be extracted from experiments despite the complicated nuclei involved.

2.2 The Allowed Approximation

The properties of beta decay can be determined in the Standard Model. This section outlines the calculation, roughly following the detailed treatment of [24]. The allowed approximation which keeps only non-nuclear-recoil order terms and the impulse approximation, which treats the basic interaction as a proton changing to a neutron within the nucleus and ignores internuclear forces, are used. This treatment gives a good physical picture of the origin of the parameters and is highly accurate as well, to a fraction of a percent in ^{21}Na. The benefits of studying a decay between isodoublets is apparent via the simple calculation of the vector matrix element. The practicality of using complicated nuclei to study the fundamentals of the weak interaction is shown when angular decay properties depend on only one parameter. Small corrections to the allowed approximation will be discussed in Section 2.5 in terms of the elementary particle picture which provides a simpler framework to view modifications.

The interaction used to calculate the decay amplitude is from allowed neutron decay,

$$H_{int} = \sum_{nucleons} \frac{G_F}{\sqrt{2}} V_{ud} \overline{\psi}_n \gamma^\mu \left(C_V - C_A \gamma_5\right) \psi_p \overline{\psi}_{\nu_e} \gamma_\mu (1 - \gamma_5) \psi_e \; + \; h.c. \tag{2.2}$$

From the CVC hypothesis the $p \rightarrow n$ reaction has the same vector strength as the underlying quark, $u \rightarrow d$, interaction so the vector coupling constant C_V equals 1. The axial vector coupling constant C_A, which is renormalized from its constituent quarks value, is equal to about 1.26 and is determined from neutron decay. When the decay interaction is applied to actual nuclei and integrated the decay amplitude is found to be

$$A_{fi} = \frac{G_F}{\sqrt{2}} V_{ud} \left[C_V < 1 > j_0 - C_A < \vec{\sigma} > \cdot \vec{j}\right]. \tag{2.3}$$

The lepton current is

$$j^\mu = \overline{\psi}_e \gamma^\mu (1 - \gamma_5) \psi_{\nu_e}. \tag{2.4}$$

The nuclear matrix elements for β^+ decay are

$$< 1 > \; = \; \sum_{j=nucleons} \int \chi_f^\dagger(\vec{r}) \tau_j^- \chi_i(\vec{r}) d^3\vec{r} \; = < \psi_f | T^- | \psi_i > \tag{2.5}$$

$$< \vec{\sigma} > \; = \; \sum_{j=nucleons} \int \chi_f^\dagger(\vec{r}) \vec{\sigma}_j \tau_j^+ \chi_i(\vec{r}) d^3\vec{r}. \tag{2.6}$$

The isospin lowering operator $T^- = \sum \tau_j^- = \sum(\overline{\psi}_n \psi_p)_j$ effectively changes a proton to a neutron. Recalling Equation 2.1, the value of the Fermi matrix element, $< 1 >$, is 1 (0) for the main (side) decay branch.

The differential transition probability is found by squaring the amplitude and including the appropriate phase space factor in the regular way,

$$dW = (2\pi)^{-5}\delta(E_e + E_\nu - E_0)\frac{m_e}{E_e}\frac{m_\nu}{E_\nu}F(Z, E_e)|A_{fi}|^2 d^3\vec{p}_e d^3\vec{p}_\nu. \tag{2.7}$$

The Fermi function, $F(Z, E_e)$, accounts for the Coulomb interaction between the nucleus and the leaving beta. The Dirac equation is solved for a positron spinor in the electric field of the nuclear charge. The simple phase space factor of a plane wave solution for the beta is then modified by the Fermi function.

From the differential transition probability all decay properties can be calculated by integration over the unobserved variables. In this way the total decay rate, energy spectra and different correlations between angular momenta and/or momentums can be calculated. The important point is that all of these properties depend on only three variables (found in $|A_{fi}|^2$) in the allowed order. One is the universal strength of the interaction, $G_F V_{ud}$, and is determined in a host of beta decays. The other two, the vector form factor $a{=}C_V < 1 >$ and the axial vector form factor $c{=}C_A < \sigma >$, are specific to a decay branch. The parameter a is accurately calculable and equal to 1 (0) for the main (side) branch in the allowed approximation. The parameter c is difficult to calculate accurately and must be found experimentally. Each branch of the ^{21}Na$\rightarrow^{21}$Ne system in the allowed order is parameterized by the known interaction strength $G_F V_{ud}$, the known vector form factor a, and one unknown factor c.

When summed over the final spins Equation 2.7 gives [25],

$$\begin{aligned} dW \;=\; & \frac{G_F^2 V_{ud}^2}{2(2\pi)^5} F(Z, E_e) p_e E_e (E_e - E_0)^2 dE_e d\Omega_e d\Omega_\nu \xi \left[1 + a_{\beta/\nu}\frac{\vec{p}_e \cdot \vec{p}_\nu}{E_e E_\nu} + b\frac{m}{E_e} \right. \\ & + c_{align}\left(\frac{\vec{p}_e \cdot \vec{p}_\nu}{3E_e E_\nu} - \frac{(\vec{p}_e \cdot \hat{j})(\vec{p}_\nu \cdot \hat{j})}{E_e E_\nu}\right)\left(\frac{J(J+1) - 3 < (\vec{J} \cdot \hat{j})^2 >}{J(2J-1)}\right) \\ & \left. + \frac{< \vec{J} >}{J} \cdot \left(A\frac{\vec{p}_e}{E_e} + B\frac{\vec{p}_\nu}{E_\nu} + D\frac{\vec{p}_e \times \vec{p}_\nu}{E_e E\nu} \right) \right]. \end{aligned} \tag{2.8}$$

Here $\vec{J}$ is the initial angular momentum of the nucleus. The unit vector $\hat{j}$ is in the direction of $< \vec{J} >$. The value of $\xi = a^2 + c^2$ affects the overall decay strength. The expressions

for the coefficients, $a_{\beta/\nu}$, b, c_{align}, A, B, and D are listed in [25]. In the Standard Model at allowed order they depend only on the ratio of the form factors $\frac{c}{a}$. These coefficients describe the correlations between spins and momenta in the decay. For example A, the beta-asymmetry parameter defines the correlation between the initial nuclear spin and the lepton momentum when the neutrino is unobserved. The beta-neutrino coefficient $a_{\beta/\nu}$ describes the correlation between the directions the beta and neutrino are emitted.

By integrating Equation 2.7 further over all variables the absolute decay rate is found. This relation is typically written in terms of the half-life $t_{1/2}$ and is

$$f_c t_{1/2} = \frac{2\pi^3 \ln 2}{G_F^2 V_{ud}^2 (a^2 + c^2)}. \tag{2.9}$$

The Fermi integral, f, integrates the phase space factors,

$$f = \int_{m_e}^{E_0} F(Z, E_e) p_e E_e (E_e - E_0)^2 \, dE_e. \tag{2.10}$$

The notation f_c represents the few percent corrections to f and is discussed in the next section.

The consistency of the Standard Model can be checked with just two measurements in the ^{21}Na$\rightarrow^{21}$Ne system combined with the ft value from $0^+ \rightarrow 0^+$ decays. Do both measurements give the same value of c? The half-life of the decay is known. Combined with the value of $G_F V_{ud}$ obtained from other experiments it can be used to calculate c. This is done in Section 2.4. Then a decay correlation measurement tests the Standard Model. For instance, a measurement of the beta-asymmetry coefficient will test for physics outside the Standard Model such as right-handed currents. Another approach which is independent of the overall interaction strength $G_F V_{ud}$ is to compare two decay correlation measurements. This approach is desirable because the several percent corrections to $G_F V_{ud}$ are avoided. Only corrections that are a few tenths of a percent are necessary. Correlation parameters depend only on $\frac{c}{a}$. So a measurement of both the beta-asymmetry coefficient and the beta neutrino correlation, each with different sensitivities to new physics, provides a test.

2.3 Corrections to ft Values

There is a lot of interest now in accurate calculations of ft values for beta decay because of the very precise experimental data available for $0^+ \rightarrow 0^+$ decays. For $0^+ \rightarrow 0^+$ decays the axial vector form factor c is zero. The operator $\sum_{j=nucleons} \vec{\sigma}_j \tau_j$ transforms like

a spherical tensor of rank 1 and doesn't connect two spin 0 states. Since the value of a for the isotriplet $0^+ \rightarrow 0^+$ decays is $\sqrt{2}$ the value of $G_F V_{ud}$ can be calculated. The value of G_F is precisely determined in muon decay so the value of V_{ud} can be found. The CKM matrix element V_{ud} is an important input to check the unitarity of the CKM matrix. The CKM matrix relates the weak quark eigenstates to the mass eigenstates in the Standard Model. The work with $0^+ \rightarrow 0^+$ decays shows the state of the art theory calculations for the ft values of super-allowed decays. Similar precision can be expected for ^{21}Na decay when experimental input values are better known.

The experimental input for calculating ft values are the beta endpoint energy E_0, the total half-life $t_{1/2}^{tot}$ and the transition's branching ratio BR. The total endpoint energy, E_0, is used for calculating f. The total half-life combines with the branching ratio to give the partial half-life $t_{1/2}$ of the individual transition. Theory comes into play with the calculation of the corrected Fermi integral, f_c. Even the standard Fermi integral, f, requires intricate calculations[26]. As noted before the Dirac equation is solved for the beta interacting with the Coulomb field of the nucleus. A nucleus with a finite gaussian distribution of charge is used. Screening of the nuclear charge by the atomic electrons as well as the small recoil of the nucleus are included. An additional energy dependent term multiplying the Fermi function, the shape factor, results from recoil order terms discussed in Section 2.5. The finite size of the distribution of weak charge in the nucleus gives a small energy dependence [27]. There is some disagreement between theorists on the value of this correction. For the heavier nucleus ^{54}Co the discrepancy is 0.2% but for the lighter nucleus ^{26}Al^m the discrepancy is only 0.05%. Estimating from the isotopes given in [27] this correction factor for ^{21}Na should be less than 0.1% with better than 0.05% agreement. The shape of the ^{21}Na spectrum must also be corrected for a calculable (see Section 2.5) weak magnetism term which is zero for the $0^+ \rightarrow 0^+$ decays. A small atomic excitation correction is also included in the calculation [26].

The value for the standard Fermi integral, f, is corrected by radiative, δ^R, and isospin breaking, δ^C, effects to arrive at the corrected Fermi integral, f_c. The standard breakdown is,

$$f_c = f(1 + \delta^R)(1 - \delta^C). \tag{2.11}$$

Details can be found in [28][29]. The radiative corrections are divided into nuclear structure dependent and independent parts. The nuclear-independent correction, $\Delta_{\beta\mu}$, allows the

comparison between the strength of muon decay and beta decay and the extraction of V_{ud}. It is not necessary for comparing different nucleon decays so the values of ft in the next section do not include it. For clarity this will be notated, $f_c t(1+\Delta_{\beta\mu})$. The radiative corrections amount to a few percent and are well agreed upon by the theorists. The nuclear-dependent corrections are about 1.5% and the nuclear-independent corrections are about 2.5%. In addition, the electromagnetic interaction breaks isospin symmetry. Correction must be made for the resulting configuration mixing and radial nucleon wavefunction mismatch. These isospin breaking corrections are fairly small but not so well agreed upon. For ^{21}Na this correction should be about 0.3% but theoretical uncertainties for similiar weight isotopes are currently as high as 0.1%[29].

The current value from $0^+ \rightarrow 0^+$ decays for $f_c t(1+\Delta_{\beta\mu})$ is 3072.3±2.0 sec giving a value of $|V_{ud}|$ equal to 0.9740±0.0005[29]. A test of the unitarity of the CKM matrix can be made with the elements of the first row which should be related by

$$V_{ud}^2 + V_{us}^2 + V_{ub}^2 = 1\,. \tag{2.12}$$

The value of V_{us} comes from K_{e3} decays ($K^+ \rightarrow \pi^0 + e^+ + \nu_e$ and $K_L^0 \rightarrow \pi^\pm + e^\mp + \nu_e$) and hyperon decays. The value of V_{ub} comes from the decay of B mesons. Using the values, $|V_{us}|$=0.2196±0.0023 and $|V_{ub}|$=0.0032±0.0008, suggested by [29] the unitarity condition, Equation 2.12, is violated ($V_{ud}^2 + V_{us}^2 + V_{ub}^2 = 0.9968 \pm 0.0014$) by 2σ. If the value of $f_c t(1+\Delta_{\beta\mu})$ from $0^+ \rightarrow 0^+$ decays was 0.3% smaller than the current value the CKM matrix unitarity would be re-established. It is still being debated whether this discrepancy indicates new physics or whether the calculations of corrections are in error. For ^{21}Na experiments the ft value is used to calculate the ratio of the form factors, c/a. Then the value of correlation coefficients can be predicted and compared with experiment to check consistency and hunt for new physics. When the precision of the correlation parameters gets very good, around this 0.3% discrepancy level, the process is logically reversed. Then the ^{21}Na correlation experiments provide a value of c/a which is combined with its ft value to determine V_{ud} as another unitarity test.

2.4 Calculating the Axial Vector Form Factor

The value of the axial vector form factor c can be calculated from the ft value of ^{21}Na. Reference [30] lists the $f_c t(1+\Delta_{\beta\mu})$ value for ^{21}Na. For consistency their value of

	$ft_{1/2}$ (^{21}Na *analog decay*)			
	f		$t_{1/2}(analog)$	
	E_0	f_{theory}	*branching ratio*	$t_{1/2}(total)$
accuracy of parameter	0.02%	0.1%	0.2%	0.1%
error in $f_c t$	0.1%	0.1%	0.2%	0.1%

Table 2.2: Current sources of uncertainty in the $f_c t$ value of ^{21}Na from experimental inputs and theory.

$f_c t(1+\Delta_{\beta\mu})$ for $0^+ \rightarrow 0^+$ decays is also used to insure that all corrections were applied in the same way. The 0.05% error seems a bit small but it is dwarfed by the error from ^{21}Na. For $0^+ \rightarrow 0^+$ beta decays the value of $f_c t$ is simply $\frac{2\pi^3 \ln 2}{G_F^2 V_{ud}^2}$. This is seen by taking $a = \sqrt{2}$ and $c = 0$ in Equation 2.9. The value of a for an isodoublet system like ^{21}Na - ^{21}Ne to be inserted in to Equation 2.9 is 1. The configuration mixing and nuclear mismatch which make $a \neq 1$ has been accounted for already in f_c. To find c for the ^{21}Na decay it is convenient just to take a ratio of $f_c t_{1/2}$ values,

$$\frac{1+c^2}{2} = \frac{f_c t_{1/2}(0^+ \rightarrow 0^+)(1+\Delta_{\beta\mu})}{f_c t_{1/2}(^{21}\mathrm{Na}\, 3/2^+ \rightarrow ^{21}\mathrm{Ne}\, 3/2^+)(1+\Delta_{\beta\mu})} \quad (2.13)$$

$$= \frac{3070.6 \pm 1.6 sec.}{4106.4 \pm 11.6 sec.} \quad (2.14)$$

which leads to

$$c = -0.704(3). \quad (2.15)$$

Table 2.2 shows the current sources of uncertainty for $f_c t$. Right now the limitations are from old experimental inputs to ^{21}Na. These could be improved if necessary. Currently the error in c causes an error in the beta-asymmetry parameter of 0.2% which could be improved to 0.1% with better experimental inputs.

2.5 Corrections to the Allowed Approximation

Corrections to the allowed approximation are a few percent when calculating absolute decay rates as seen in the previous sections. For relative decay rates the allowed approximation is even better, a fraction of a percent. Relative decay rates, such as the rate of beta emission parallel vs antiparallel to the nuclear spin, come into play when computing

beta decay correlation parameters. Since the goal of this experiment is to measure decay correlations with precisions of less than a percent these corrections will have to be made.

It is useful to discuss the small recoil corrections to allowed decay in the so called elementary particle approximation. The elementary particle approach treats the parent and daughter nuclei as fundamental particles, designated by only their external four-momentum and spin. A general interaction is written based on all possible combinations of spin (J', m' and J, m) and four-momentum (p_i and p_f) which give Lorentz invariants up to first order in the nuclear recoil. This includes various induced terms with their associated form factors not found in the fundamental interaction. Since terms are formed based on rotational symmetry it is easy to utilize the CVC hypothesis in conjunction with the isodoublet decay structure to determine all the vector type form factors. Terms with the same variable dependence are combined, regardless of origin. For instance the weak magnetism term has a normal component from the recoil order vector interaction as well as an anomalous induced part. The grouping makes it easy to cut the calculation at a given precision.

Holstein writes [31] the most general nuclear beta decay transition which has ten terms. For an isodoublet transition the CVC hypothesis requires the induced pseudoscalar term, e, and a high order tensor term, f, to be zero. Because only the second-class current components of the induced tensor term, d, and the j_2 term contribute to an isodoublet transition d and j_2 are both zero. Other form factors h, the induced pseudoscalar, and j_3 are allowed but don't contribute significantly. The four remaining terms that have a significant contribution for ^{21}Na are written here,

$$\begin{aligned} l^\mu < \psi_f(p_f, J', m')|V_\mu|\psi_i(p_i, J, m) > &= \delta_{JJ'}\delta_{mm'}a(q^2)\frac{P\cdot l}{2M} + ib(q^2)\frac{1}{2M}C^{m'k;m}_{J'1;J}(\vec{q}\times\vec{l})_k \\ &\quad + g(q^2)\frac{1}{(2M)^3}C^{m'k;m}_{J'2;J}P\cdot l\sqrt{\frac{4\pi}{5}}Y^k_2(\hat{q})q^2 \end{aligned} \tag{2.16}$$

and

$$l^\mu < \psi_f(p_f, J', m')|A_\mu|\psi_i(p_i, J, m) > = C^{m'k;m}_{J'1;J}\varepsilon_{ijk}\varepsilon_{ij\lambda\eta}\frac{1}{4M}c(q^2)l^\lambda P^\eta \tag{2.17}$$

where

$$\begin{aligned} P &= p_i + p_f \\ q &= p_i - p_f = p_e + p_\nu \text{ (four} - \text{momentum transfer)} \\ M &= \frac{M_i + M_f}{2}. \end{aligned}$$

Electromagnetic Quantity	^{21}Na	^{21}Ne	Weak Form Factor	Value
nuclear charge	+11e	+10e	$a(0)$	1
magnetic moment	+2.3861(1)μ_B[32]	-0.661797(5)μ_B[33]	$b(0)$	82.7
electric quadrupole	+0.05(4) barn[33]	+0.103(8) barn[33]	$g(0)$	$8\pm8\times10^4$

Table 2.3: Electromagnetic parameters and the weak form factors determined with them from CVC.

The vector form factor $a(q^2)$ and the axial vector form factor $c(q^2)$ are the large terms and reduce to their previous definitions in the allowed approximation where recoil-order terms are neglected ($q^2 = 0$). The weak magnetism form factor $b(q^2)$ and the electric quadrupole form factor $g(q^2)$ contribute only in recoil-order. By applying the formal mathematical CVC relation which relates the weak interaction couplings between isotropic analog states to their electromagnetic analogs ,

$$[I_-, J_\mu^{em}] = +V_\mu^{W-} \tag{2.18}$$

a, b and g are determined from the electromagnetic properties of the nuclei [31]. Values for the ^{21}Na$(3/2^+) \rightarrow {}^{21}Ne(3/2^+)$ decay are summarized in Table 2.3.

Holstein [34] gives extensive formulas to calculate decay properties taking into account these higher order terms. Here estimates of the sizes of the corrections to correlation parameters are given. The sizes are discussed in terms of how the errors scale with the decay properties and are summarized in Table 2.4. These give the approximate size of the corrections to a general correlation coefficient. Specific numbers for the beta-asymmetry coefficient, A, are given in Section 2.6.

One set of recoil-order corrections to allowed beta decay has size of order q^2R^2. These are due to the next term in the expansion of the lepton current, e^{iqr}, interacting with the finite extent of the nucleus. Explicit q^2 dependence for a and c results. It is parameterized by Holstein [34] by,

$$\begin{aligned} a(q^2) &= a_1 + a_2(q^2/M^2) \\ c(q^2) &= c_1 + c_2(q^2/M^2). \end{aligned} \tag{2.19}$$

Both a_2 and c_2 are order M^2R^2 so the corrections are of order q^2R^2. The electric quadrupole from factor g also contributes at the q^2R^2 order. Although the electric quadrupole term

Source	Scaling	Size of Scaling for ^{21}Na
weak magnetism	Aq/M	0.3%
q^2 dependence of a, c	q^2R^2	0.4%
weak electric quadrupole	q^2R^2	0.4%
electromagnetic	αZRE_0	0.5%

Table 2.4: Order of magnitude estimates of the size of corrections to allowed beta decay for correlation experiments.

appears to contribute at order q^2/M^2 from Equation 2.16, the form factor g is order M^2R^2 not unity, so the overall order is q^2R^2. For nuclei,

$$R \approx 7 \times 10^{-3} A^{1/3} \text{ 1/MeV}. \tag{2.20}$$

So for ^{21}Na, $R \approx 2 \times 10^{-2}$ 1/MeV. The maximum value of $|q|$ is about 3 MeV/c, the beta endpoint energy. So for ^{21}Na q^2R^2 is about 4×10^{-3}.

The second set of recoil order corrections have order q/M which come from higher order terms in the expansion of the allowed terms as well as parts that are induced by the strong interaction acting among the nucleons of the composite nuclei. For ^{21}Na the value, $q/M \approx 2 \times 10^{-4}$, is quite small. There are many terms at the q/M level, the pseudoscalar form factor term being one, but these contribute too little to consider here. The weak magnetism from factor, though, enters like $Aq/M \approx 3 \times 10^{-3}$ for ^{21}Na and must be corrected for at the sub-percent accuracy level.

Most of the electromagnetic corrections cancel in the calculation of the angular distributions of decay products. The configuration mixing and nuclear-mismatch which make a different from 1 are accounted for in calculating c/a, which is the only parameter needed for angular correlation calculations. The small remaining radiative type corrections can be calculated via [35] by long and tedious formulas. The corrections to angular distributions are of order αZRE_0 which is $\approx 0.5\%$ for ^{21}Na.

2.6 Beta-Asymmetry Coefficient for ^{21}Na

One measurement that can be made in a trap is of the beta-asymmetry coefficient for ^{21}Na. The angular distribution of betas emitted from polarized nuclei is found by

input	correction to A_0	uncertainty to A_0
weak magnetism	+0.19%	<0.01%
electric quadrupole	<0.01%	<0.01%
electromagnetic	≈0.5%	0.1%
a_2, c_2	+0.05%	0.02%

Table 2.5: Corrections to the beta-asymmetry parameter at zero beta kinetic energy, A_0

integrating Equation 2.8 over the unobserved neutrino,

$$\begin{aligned} dW &\propto 1 + A\frac{<\vec{J}>}{J} \cdot \frac{\vec{p}_e}{E_e} = 1 + AP\beta\cos\theta \qquad (2.21)\\ P &= \text{nuclear polarization} \\ \beta &= \frac{v_e}{c} \\ \theta &= \text{angle between the polarization axis and the emitted beta.} \end{aligned}$$

The beta-asymmetry parameter, A, parameterizes the degree of asymmetry in the decay and is predicted by the Standard Model. The value of A in allowed order in the Standard Model is [24],

$$A(j \to j+1) = \frac{-j}{j+1} \qquad (2.22)$$

$$A(j \to j) = \frac{\frac{c^2}{j+1} - 2ac\sqrt{\frac{j}{j+1}}}{a^2+c^2} \qquad (2.23)$$

For the two ^{21}Na decay branches, using $c = -0.704(3)$ from Equation 2.15 and a=1, the values of A are,

$$A\left(\frac{3}{2}^+ \to \frac{5}{2}^+\right) = -0.60 \qquad (2.24)$$

$$A\left(\frac{3}{2}^+ \to \frac{3}{2}^+\right) = 0.862(2). \qquad (2.25)$$

Corrections to the allowed approximation value of A add a small energy dependence. A_0 refers to the value of A when the beta has zero kinetic energy. The size of the corrections for A_0 are listed in Table 2.5. The weak magnetism and electric quadrupole contributions are readily calculable using the equations in [34]. The correction due to the q^2 dependence of a and c is also calculated via[34] but an estimate of the sizes of a_2 and c_2

must be made. The electromagnetic correction is estimated to be ≈0.5% using an approximate equation in [35]. For ^{19}Ne the electromagnetic correction was 0.4% [36], although some discrepancy between values was noted. A 0.1% error was listed to reflect the precision a theorist could currently expect. Applying all of the corrections except the electromagnetic correction the corrected value of A_0 equals 0.863(2).

The beta energy dependence from weak magnetism for A is minimal in the case of ^{21}Na. In contrast, in the case of ^{19}Ne which has a small value of A_0 the weak magnetism contribution to the slope is large and experimentally determined[15]. Weak magnetism for ^{21}Na gives a dependence of A on the total beta energy, E_e, equal to

$$A(E_e) = 0.863 - 5 \times 10^{-4}(E_e - m_e) - 3 \times 10^{-4}\left(\frac{1}{E_e} - \frac{1}{m_e}\right). \tag{2.26}$$

Finally, higher order angular dependences are also present due to corrections to the allowed order[35]. A term with dependency $E_e\beta^2(P^2\cos^2\theta - \frac{1}{3})$ has a coefficient with a value of a few$\times 10^{-3}$. Another term has a $E_e^2\beta^3 P\cos\theta(P^2\cos^2\theta - \frac{3}{5})$ dependency and a coefficient with a value of a few$\times 10^{-4}$. These terms are indistinguishable from the constant and $\cos\theta$ terms with just an up/down ($\cos\theta = \pm 1$) measurement. For sub-percent precision A measurements an accounting must be made for these additional terms.

2.7 Right-Handed Weak Currents

The Standard Model puts parity violation of the weak interaction into the Hamiltonian by hand. The result is the $(1 - \gamma_5)$ factor in both the quark and lepton currents which gives the weak interaction its left-handed nature. Models rooted in a higher symmetry may include a small right handed current which has a $(1 + \gamma_5)$ factor. These possible small right-handed currents will introduce small changes in the values of decay correlation coefficients. The beta-asymmetry coefficient is sensitive to such currents. Figure 2.2 illustrates this with a simple decay, A(J = 1) → B(J = 0) + β^+ + ν_e. In the figure spin is represented by the wide, open arrows and emission direction by solid arrows. The A nucleus has spin 1 and is 100% polarized in the up direction. The B daughter nucleus has spin 0 so the decay product leptons must carry off the original spin. The left-handed current (LHC), $\overline{\psi}_{\nu_e}\gamma_\mu(1-\gamma_5)\psi_e$, results in left-handed e^-'s and ν_e's as well as right-handed e^+'s and $\overline{\nu}_e$'s. Any right-handed current (RHC) contribution gives the leptons the opposite handedness from the LHC. To preserve spin in a LHC system the right-handed positron

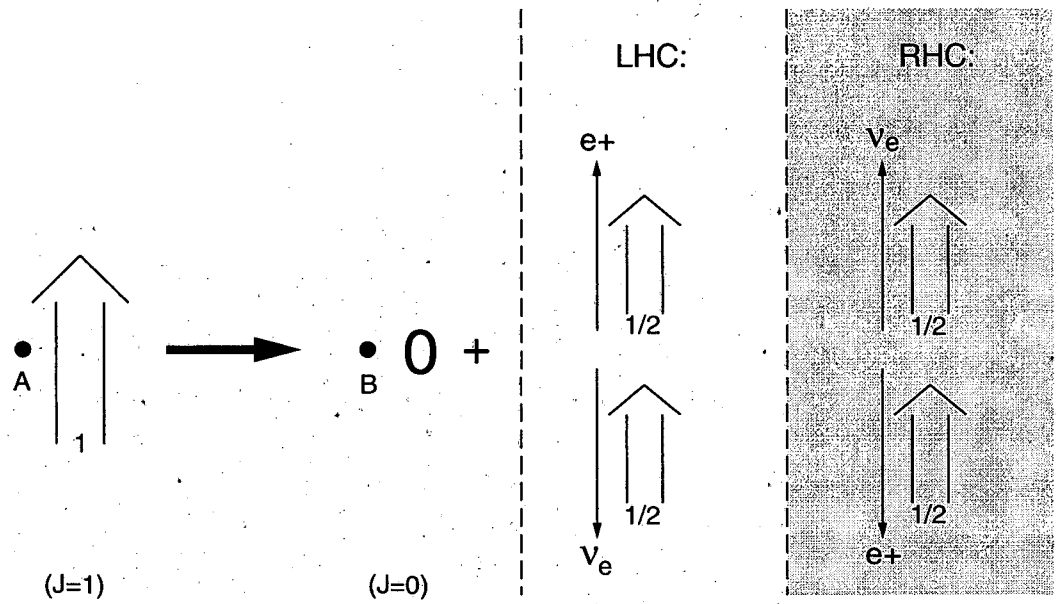

Figure 2.2: Diagram illustrating the sensitivity of beta decay correlation measurements to right-handed currents.

is emitted upward and the left-handed neutrino is emitted downward. The shaded gray section of Figure 2.2 shows the lepton emission directions for a RHC system. To preserve spin in this case the leptons are emitted in the opposite directions from the LHC system. The beta-asymmetry measures the direction of the emitted e^+ relative to the initial spin. A RHC contribution to the interaction causes a e^+ emitted in the opposite direction from the LHC system and reduces the asymmetry. On the other hand the beta-neutrino correlation in this example (corresponding to ζ=0 in the following manifest right-left symmetric model) is unaffected by a right-handed current contribution. The decay leptons in this example are emitted back to back in both the LHC and RHC systems.

A popular model with which to compare the limits set with different experiments is the manifest left-right symmetric model (MLRS)[37]. A second set of W bosons which are right-handed are added. In general the physical bosons, W_1 and W_2, are linear combinations of the left and right-handed bosons, W_L and W_R. The mixing between the bosons is parameterized by the angle ζ. The square of the physical masses is $\delta = (\frac{M_1}{M_2})^2$. The expressions for W_1 and W_2 are

$$W_1 = W_L \cos\zeta - W_R \sin\zeta \tag{2.27}$$

$$W_2 = W_L \sin\zeta + W_R \cos\zeta \, .$$

The beta-asymmetry measurement is sensitive to the manifest left-right symmetric parameters by the equation[30],

$$A(0) = A_0(1 + \varepsilon\zeta^2 + 2\varepsilon\zeta\delta - 2\delta^2) \, . \tag{2.28}$$

For the $3/2^+ \rightarrow 3/2^+$ decay branch of ^{21}Na the sensitivity coefficient ε, which is derived in [30] from a formula based on just the vector and axial vector form factors, equals -0.308. Figure 2.3 shows the limits on δ and ζ from Equation 2.28 given that A_{exp}/A_0 is measured to a 3%, 1%, and 0.1% precision. The area above each curve is excluded in each case. Also shown in Figure 2.3 as a dashed curve is the limit set by a 1% measurement of the ratio of the beta-asymmetry correlation and the beta-neutrino correlation using the sensitivity formulas in [36].

Many experiments contribute to limiting the δ/ζ parameter space. Some recent reviews[36][28][38] of the data have gathered the various results. Figure 2.4 shows the 90% confidence level limits from some experiments. The ^{19}Ne beta-asymmetry and lifetime data give the dashed line limit in Figure 2.4[36]. The neutron beta-asymmetry combined with the neutron lifetime data as of 1992 give the limit labeled $A(n)$[36]. This limit does not include the outlying Gatchina neutron beta-asymmetry data. The limit is shown here only to indicate the exclusion shape that the $\approx$1% neutron beta-asymmetry data give. Since 1992 there have been two new neutron beta-asymmetry results[18][19] and a revision of the Gatchina result[17] but as mentioned in Section 1.2 these results are in disagreement with each other. A tighter δ, ζ limit from the neutron beta-asymmetry waits for this situation to be resolved. It is interesting to note that the ^{19}Ne and neutron beta-asymmetries do not limit δ when $\zeta \approx 0$. This fact contrasts with the ^{21}Na beta-asymmetry limits which restrict δ at $\zeta \approx 0$ but have little sensitivity to the value of ζ. For the neutron, the neutrino-asymmetry coefficient, B in Equation 2.8, sets the limit labeled B_n in Figure 2.4[38]. Measurements of the absolute polarizations of the betas resulting from beta decay give the limit labeled β Pol[38]. Relative polarization measurements of the betas from two different decays, one pure Fermi and one pure Gamow-Teller constrain δ and ζ. These measurements can be made precisely (0.4%) with Bhabha polarimetry[39] or time resolved positronium decay polarimetry[40]. The constraints from the later are shown in Figure 2.4 labeled P_F/P_{GT}. Precise measurements of the endpoint beta spectrum from polarized muon decay give the

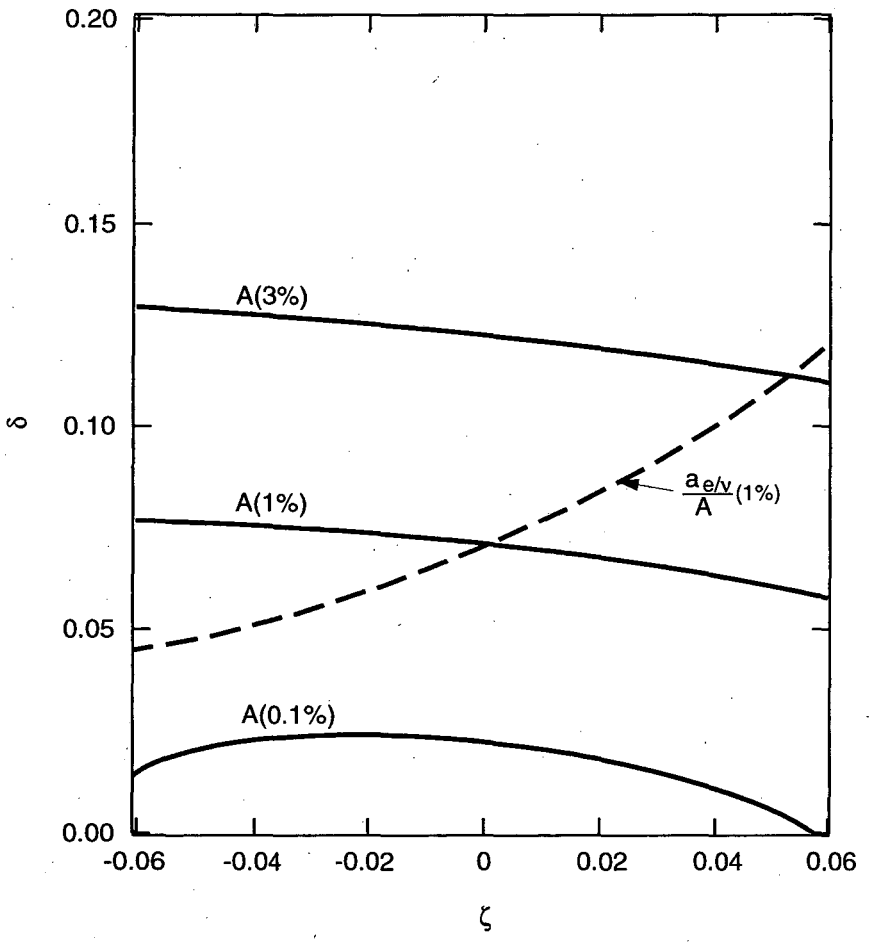

Figure 2.3: Limits on manifest left-right symmetric parameters δ and ζ which would result from ^{21}Na decay measurements on the $3/2^+ \rightarrow 3/2^+$ decay branch.

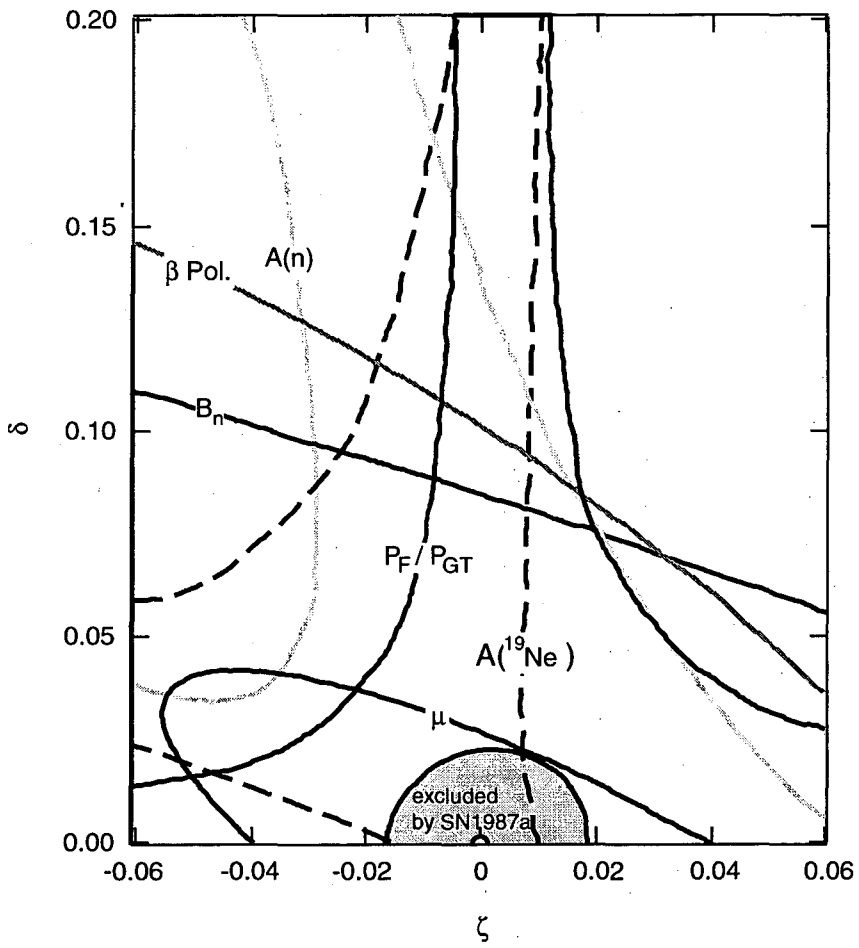

Figure 2.4: Limits at 90% confidence on manifest left-right symmetric parameters δ and ζ from current experiments.

limit labeled μ in Figure 2.4[41]. Although the limits set by this purely leptonic process are tight for the MLRS model, in extensions to this simple model the muon limits need not be so tight. For instance, in models with massive neutrinos muon decay is insensitive to W_R if ν_μ^R is heavy. Polarization asymmetry measurements, the relative polarization of the beta emitted parallel and antiparallel to the initial nuclear spin, are very sensitive to RHC's when the beta-asymmetry coefficient for the decay is nearly 1 and the nuclei are highly polarized. New work with ^{107}In and ^{12}N[42] measures this asymmetry. The limit for the W_2 mass at $\zeta = 0$ is given as $m_{W_2} > 300$ GeV or $\delta < 0.07$ at the 95% confidence level. They state that their ζ=0 assumption is consistent with the stringent limits on ζ, $-0.0006 < \zeta < 0.0028$, set by demanding CKM matrix unitarity. Direct searches for new W's at $p\overline{p}$ colliders give $m_{W_{new}} > 720$ GeV ($\delta < 0.01$)[43]. Reference [42] discusses the cases outside the MLRS model where these limits are weakened and low energy experiments are important. If the CKM matrices for the right and left sectors are not equal or the W_R mass is about W_L (the right-handed coupling is small in this case in accordance with the fact that W_R has not been detected yet) then the direct search limits do not apply. Limits on m_{W_R} from the $K_0 - \overline{K}_0$ mass difference[42][44][45] have changed over the years, generally getting looser. The current limit is $M_R > 300$ GeV or $\delta < 0.07$. Finally, more theoretical calculations give limits on δ and ζ from the observation of the neutrino luminosity from the supernova SN1987a where the introduction of a right-handed W modifies the neutrino production mechanism[46]. The shaded area in Figure 2.4 is claimed to be excluded by the supernova observations[38].

2.8 Other Correlation Coefficients

The electron-neutrino correlation is a measure of the angular distribution between the beta and neutrino emitted in beta decay. Detection of the recoiling daughter nucleus makes it pratical to determine the electron-neutrino coefficient, $a_{\beta/\nu}$. The energy of the daughter ion depends on the beta-neutrino relative angle. This point is discussed in more detail in Chapter 6. For unpolarized nuclei Equation 2.8 becomes:

$$dW \propto 1 + a_{\beta/\nu}\frac{\vec{p}_e \cdot \vec{p}_\nu}{E_e E_\nu} = 1 + a_{\beta/\nu}\beta\cos\theta_{\beta/\nu}. \tag{2.29}$$

Here β is $\frac{v_e}{c}$ and $\theta_{\beta/\nu}$ is the angle between the directions the beta and neutrino are emitted. In the Standard Model at the allowed order the expression for $a_{\beta/\nu}$ is

$$a_{\beta/\nu} = \frac{a^2 - \frac{1}{3}c^2}{a^2 + c^2} \ . \tag{2.30}$$

Using the values of a and c from Section 2.4 the result for the $3/2^+ \rightarrow 3/2^+$ decay branch is $a_{\beta/\nu}$=0.558(3). The error listed is only from the uncertainty in c. For the $3/2^+ \rightarrow 5/2^+$ decay branch $a_{\beta/\nu}$=$-\frac{1}{3}$. Both of these values must be adjusted for the recoil order corrections described in Section 2.5 which enter at the few tenths of a percent level.

A precise measurement of the beta-neutrino correlation in ^{21}Na is interesting because it is sensitive to possible scalar and tensor contributions to the weak interaction. Exotic extensions to the Standard Model such as leptoquarks, charged scalar bosons, and supersymmetric particles can introduce scalar and/or tensor interactions[47]. The sensitivity to scalar and tensor contributions is parameterized here in terms of the size of the C_S, C'_S, C_T, and C'_T coefficients defined in Equation 1.3. Given the Standard Model's C'_V=C_V and C'_A=C_A how much room is there for nonzero scalar and tensor coefficients given a measurement of $a_{\beta/\nu}$ with a given precision? Using the general formula for $a_{\beta/\nu}$[25] including nonzero scalar and tensor coefficients gives for ^{21}Na that

$$a_{\beta/\nu} = 0.558 - 0.52\left[\frac{|C_S|^2}{C_V^2} + \frac{|C'_S|^2}{C_V^2}\right] - 0.04\left[\frac{|C_T|^2}{C_A^2} + \frac{|C'_T|^2}{C_A^2}\right] \tag{2.31}$$

for the $3/2^+ \rightarrow 3/2^+$ branch and

$$a_{\beta/\nu} = -\frac{1}{3} + 0.67\left[\frac{|C_T|^2}{C_A^2} + \frac{|C'_T|^2}{C_A^2}\right] \tag{2.32}$$

for the $3/2^+ \rightarrow 5/2^+$ branch. A 1% measurement of $a_{\beta/\nu}$ for the $3/2^+ \rightarrow 3/2^+$ branch gives the limit,

$$\left[\frac{|C_S|^2}{C_V^2} + \frac{|C'_S|^2}{C_V^2}\right] - 0.08\left[\frac{|C_T|^2}{C_A^2} + \frac{|C'_T|^2}{C_A^2}\right] < 0.01 \ . \tag{2.33}$$

Limits on scalar and tensor terms from current experiments come from two different types of experiment. The first type searches for effects which result from vector/scalar or axial vector/tensor interference. This so called Fierz interference term, b in Equation 2.8, is valued in the Standard Model as b=0. Strict limits can be placed on b with spectral shape measurements and the constancy of the ft values for $0^+ \rightarrow 0^+$ transitions[48][49]. The measurements of b only limit the sums $C_S + C'_S$ and $C_T + C'_T$ and fail to provide a bound

for the cases that $C_S = -C'_S$ or $C_T = -C'_T$. The other types of experiments, like the beta-neutrino correlation, are sensitive to the sums $[|C_S|^2 + |C'_S|^2]$ and $[|C_T|^2 + |C'_T|^2]$. In combination the two experimental types limit the scalar and tensor terms. The current limits for $\frac{C_S}{C_V}$, $\frac{C'_S}{C_V}$, $\frac{C_T}{C_A}$, and $\frac{C'_T}{C_A}$ independently are only in the 10% range[50]. Referring to the limits set in Equation 2.33 a $< 1\%$ measurement of $a_{\beta/\nu}$ for ^{21}Na would improve the current limits on scalar contributions to the weak interaction.

Two more important correlation coefficients that are accessible with recoil daughter ion detection combined with nuclear polarization are B and D. The coefficient B is the neutrino-asymmetry parameter and measures the correlation between the initial nuclear spin and the direction the neutrino is emitted. The value of B in allowed order in the Standard Model is [24],

$$B(j \to j+1) = \frac{j}{j+1} \tag{2.34}$$

$$B(j \to j) = \frac{-\frac{c^2}{j+1} - 2ac\sqrt{\frac{j}{j+1}}}{a^2 + c^2} \tag{2.35}$$

For ^{21}Na's $3/2^+ \to 3/2^+$ branch, $B = 0.5967(3)$. For ^{21}Na's $3/2^+ \to 5/2^+$ branch, $B = 1/3$. Again, the error listed is only the error from the value of c. The coefficient B is also sensitive to right-handed currents and has a similiar sensitivity to A at $\zeta \approx 0$. The other coefficient, D, measures the triple correlation $\vec{J}_i \cdot (\vec{p}_e \times \vec{p}_\nu)$. It is time reversal violating and non-zero in the allowed approximation (in the absence of final-state interactions) only for complex values of a/c.

Chapter 3

Production of ^{21}Na with a Magnesium Oxide Target

The issue of ^{21}Na production is central to this experiment. In order to trap the twenty-two second half-life isotope, it must be produced as the experiment runs. We make it by bombarding a target containing ^{24}Mg with 25 MeV protons to get ^{21}Na via the ^{24}Mg$(p,\alpha)^{21}$Na reaction. The amount of trapped ^{21}Na depends on the efficiencies of many processes. The first of these is how much sodium can be produced and extracted from the target to form an atomic beam. A desirable target system allows the created activity to diffuse quickly and completely out of the target material. The target must last for multi-day runs without evaporating or melting. The several microamps of proton beam current available from the cyclotron should be usable without destroying the target. Minimal pollution of the atomic beam by the target material is desirable. Then we can efficiently extract a highly collimated atomic beam via long exit tubes out of the target. The high vacuum at the trap region can also be maintained and trap size reducing collision between atomic beam contaminants and trapped atoms will be minimized. This chapter describes the development of a magnesium oxide target system which contains these features.

3.1 The Magnesium Oxide Target and Crucible Holder

The original version of this experiment used a metallic magnesium target for production of ^{21}Na. We chose a MgO target material to replace the magnesium for many reasons. The slow diffusion of the sodium in the magnesium limited the amount extracted

from the target to about 1% of the amount made[51]. The rest decayed in the target. To maximize the diffusion rates the magnesium target was heated to just below its melting point. At this temperature the magnesium target evaporated in about 10 hours. The evaporated magnesium polluted the atomic beam. Magnesium in the beam collided with the trapped ^{21}Na atoms, kicking them out of the trap. The highly refractory MgO with its high melting point, 2800°C, and low vapor pressure, 1×10^{-5} torr at 1227°C[52], promised to solve these problems. Heating the MgO to very high temperatures would allow the created activity to diffuse quickly so all the ^{21}Na made could be extracted. The target material would remain solid, avoiding the problems with an evaporating target and allowing passive collimation. The high temperature theory worked only moderately well. Sintering of the target as it was heated limited the temperature. Individual grains of MgO fused into larger grains, slowing the diffusion rates. The process of finding the right temperature to maximize production in light of this problem is detailed in Section 3.6. The experiment benefited from the low vapor pressure of the target material. Implementation of passive collimation for which low crucible pressure is required increased the amount of ^{21}Na delivered to the trapping region. The fact that the MgO target lasts for 24 hour runs, under the bombardment of 2 μA of protons, without a decrease in production is also important.

A series of experimental target development runs, discussed in Section 3.6, determined the final target and crucible configuration. In this section the final design is detailed. The target is made from magnesium oxide powder with a -325 mesh size which corresponds to a maximum grain size of 40 μm. A 40 mg portion of powder is put into a cylindrical form 1 cm in diameter. The powder is lightly pressed in the form with a hand press so that the resulting disc holds together but is not glossy on its surface. The resulting disc thickness is about 330 μm. Nine such discs make up a target. The discs are spaced equally apart in a tantalum holder and placed in a 2.5 cm long cylindrical alumina crucible.

The target crucible is made of 95% alumina ceramic. Figure 3.1 shows the crucible. It is held in place inside the oven by multiple set screws which grip the end of the 14 cm long crucible stem. The top part of the crucible is cylindrical with the dimensions shown in Figure 3.1. The target is loaded into the top of the crucible which is screwed into the stem. A thermocouple is placed in a small through hole at the base to monitor the temperature of the crucible. The ^{21}Na produced in the target exits through four small channel holes. The hole pattern in shown in Figure 3.1. The channels have an 8 to 1 length to diameter ratio. They are tapered to allow tantalum tubes to be inserted into them to add even more

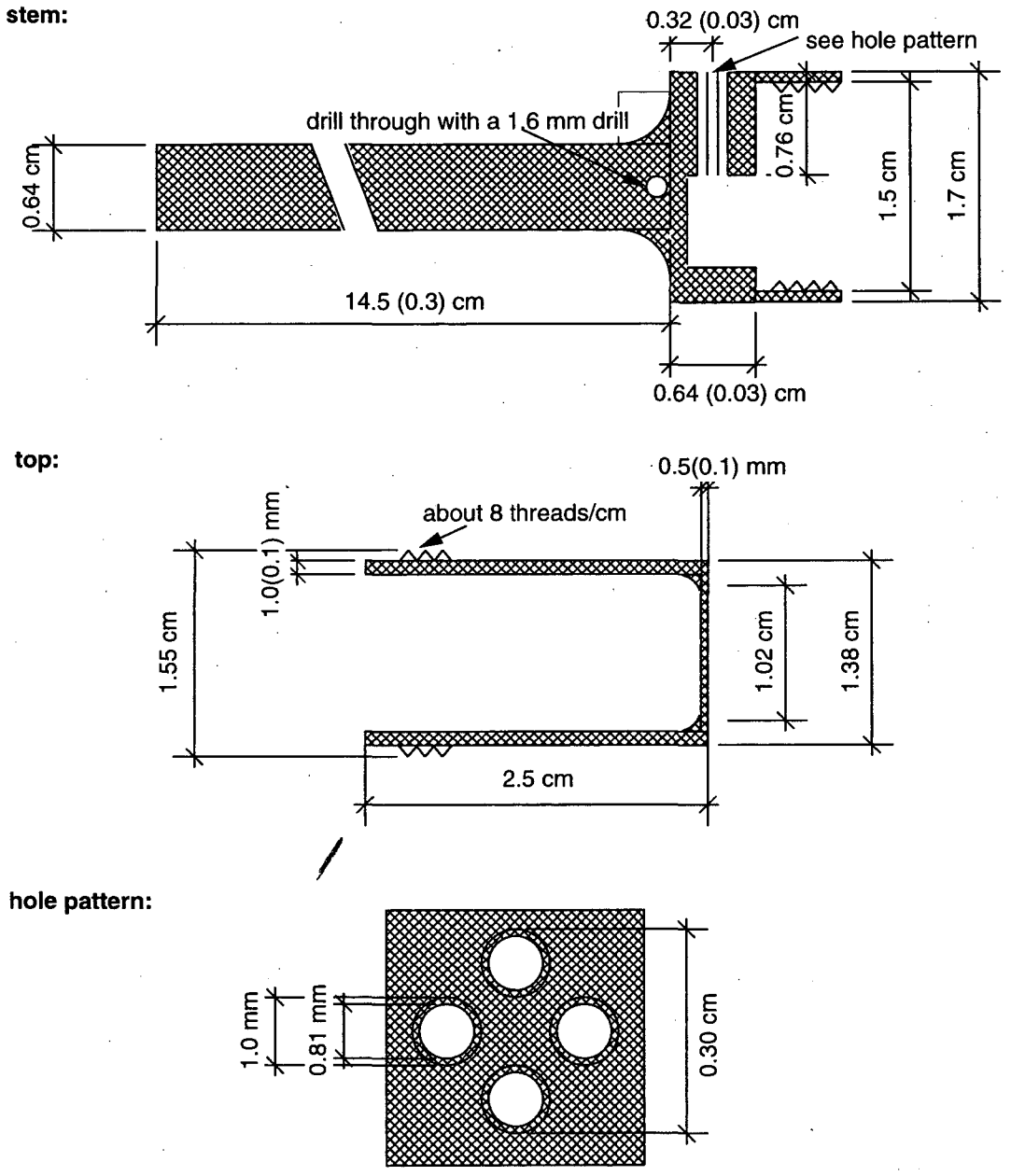

Figure 3.1: Schematic of the oven crucible. It is made out of 95% alumina ceramic.

collimation. Tantalum tubing with a 0.65 mm inner diameter and a 1.05 mm outer diameter was cut into four 1.5 cm long tubes. The ends of these tubes were tapered with a sanding wheel so that they fit snugly when inserted into the crucible. No additional attachment is necessary to hold the tubes in place. With the tantalum tubes in place the length to diameter ratio is increased to 23 to 1.

A beam of 25 MeV protons from the cyclotron enters through the thin, 0.5 mm (0.2 g/cm^2), crucible top. The energy loss of the proton beam in this window is 4 MeV. The estimated proton energy range of the significant production cross section of the ^{24}Mg$(p,\alpha)^{21}$Na reaction is from 21 MeV to 12 MeV (see Section 3.5). Protons traveling through 360mg/cm^2 of MgO will be slowed from 21 MeV to 12 MeV. The target is 450mg/cm^2 thick and therefore utilizes the useful production. After traversing the target material the protons stop in the crucible.

We prebake the target in order to boil off contaminants. Typically, oven temperatures up to 400°C are used when testing the trapping apparatus with ^{23}Na so the oven temperature needs to be raised in preparation for a beam time. First the vacuum valve separating the trap region and the target region is closed and the cryo and ion pumps on the target region side are valved out. With only the turbo pump opened to the target region the oven temperature is raised gradually for several hours. As the oven temperature increases a sudden increase in pressure occurs as contaminants vaporize. Experience taught that if the pressure reading on the target region's ion gauge is maintained below 1×10^{-5} torr then gas release in the target material does not damage the target. Once the oven temperature reaches the operating temperature required for the proton beam, typically 880°C (106 A, 4.8 V), it is left overnight. The pressure the next day reduces to a few$\times 10^{-7}$ torr. After valving in the ion and cryo pumps the target side pressure reduces to about 2×10^{-8} torr. The target is then ready for proton bombardment.

3.2 Passive Collimation of the Atomic Beam

This section describes how for limited production of activity within a crucible, long exit tubes not only collimate the outgoing flux but increase the usable forward flux. The following formulas are only exactly correct for ideal conditions. The mean free path of a ^{21}Na atom in the crucible, λ_{atom}, must be large compared to the length of the tubes, l. The holdup time, τ_h, before the ^{21}Na atom finds the exit aperture must be small compared

to the beta decay half-life, $\tau_{1/2}$. Specific values are given below for the current MgO target showing that it meets these criteria well.

Reference [53] is a useful summary of atomic beam ovens. An important result from molecular effusion is that for a specific atom species, the forward flux, $I(0)$, and the total flow rate, R, of atoms emanating from an aperture scales to the absolute temperature, T, and the pressure, p, by

$$I(0) \propto pT^{-1/2} \tag{3.1}$$

and

$$R \propto pT^{-1/2}. \tag{3.2}$$

The exact coefficients depend on the geometry. All comparisons that follow will be made at the same temperature, T. The fact that the flux and flow rate are proportional to the pressure will be the important concept from Equations 3.1 and 3.2.

A comparison of the fluxes from two crucibles that are the same size but have different exit apertures illustrates the benefits of a crucible with a long channel aperture. Two crucibles, a and b, are compared. Crucible a has an aperture of area A and infinitesimally thin walls. Crucible b also has an aperture of area A but its aperture is extended into a cylindrical channel of length l. Another consequence of molecular effusion is that the forward flux from an extended channel aperture is the same as from an ideal aperture (infinitesimally thin walls) with the same aperture area at the same pressure. Combining this result with the pressure dependency of Equation 3.1 gives

$$\frac{I_b(0)}{I_a(0)} = \frac{p_b}{p_a}. \tag{3.3}$$

The total flow rate through a channel is related to the total flow rate through an ideal aperture of the same area and pressure by Clausing's G factor[54],

$$R_b = GR_a \quad (p_b = p_a). \tag{3.4}$$

Using Equation 3.2, Equation 3.4 can be extended for different pressures to be,

$$\frac{R_b}{R_a} = G\frac{p_b}{p_a}. \tag{3.5}$$

In a regular atomic oven supplied with stable material the vapor pressure is a function of the oven temperature so $p_a = p_b$ for the same temperature. Then the forward flux is the same for the two crucibles and the channels do not increase the forward flux but decrease

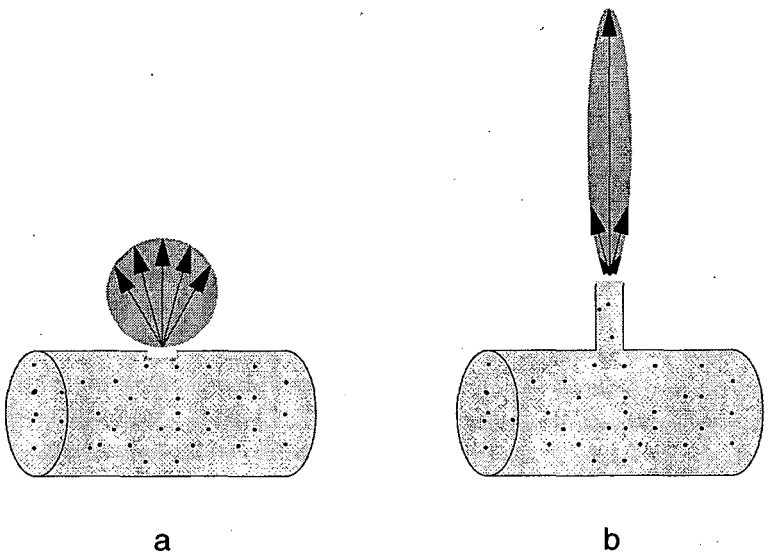

Figure 3.2: Pictorial explanation of the increase in forward atomic flux due to a channel aperture in the case of a fixed production of atoms.

the flux wasted off to the sides. For a radioactive oven, though, there is a limited production of activity so the pressures are not the same. In equilibrium, the production rate, R_{prod}, of the activity diffusing from the target equals the rate it leaves the oven. Here we assume that the ^{21}Na does not beta decay as it bounces in the crucible before finding the exit aperture. Under these circumstances,

$$R_a = R_b = R_{prod}. \tag{3.6}$$

Using this result in Equation 3.5 gives

$$\frac{p_a}{p_b} = G. \tag{3.7}$$

With this ratio of pressures Equation 3.3 gives

$$\frac{I_a(0)}{I_b(0)} = G. \tag{3.8}$$

The flux in the forward direction therefore increases by the factor $1/G$ when long channel tubes are used. Figure 3.2 shows the concept pictorially. The tubes effectively recycle the limited activity produced. If the ^{21}Na can not exit in the forward direction it returns to the oven for another try. The shaded regions in Figure 3.2 indicate the angular distribution of the flux. The areas of the shaded regions are equal to describe the equality of the total flows exiting the two crucibles. The arrows represent the flux in specific directions. The

Variable	Description	Value Used
A	crucible aperture area	2×10^{-2} cm^2
k	Boltzmann's constant	1.38×10^{-23} J/K
m	mass of ^{21}Na	3.6×10^{-2}
p	pressure inside crucible	$< 7 \times 10^{-5}$ torr
σ	collision cross section of ^{21}Na	5×10^{-14} cm^2
T	oven temperature	1300K
V	volume of crucible	3.2 cm^3
$\overline{v}$	mean velocity of ^{21}Na	1.1×10^3 m/s

Table 3.1: Variables and values used in Equations 3.10, 3.11 and 3.12.

forward flux form crucible b is greater than from crucible a because its angular distribution is more forwardly directed. This holds as long as the holdup time for radioactive atoms is small compared to the decay time.

For long cylindrical exit tubes in the crucible with length l and diameter d, the Clausing's factor is[53]

$$G = \frac{4d}{3l}. \tag{3.9}$$

The final design had a length to diameter ratio of 23 to 1 and $G = 1/17$. The original crucible had a 3 to 1 aperture and G=1/2. Therefore about a factor of eight increase in forward flux as a result of using the long tubes is expected.

The actual values for the mean free path and holdup time are calculated below. The numerical values of the input variables are collected in Table 3.1. The mean holdup time, τ_h, of an atom in an ideal crucible is

$$\tau_h = \frac{4V}{\overline{v}A} \tag{3.10}$$

where the mean velocity, $\overline{v}$, is

$$\overline{v} = \left(\frac{8kT}{\pi m}\right). \tag{3.11}$$

At a temperature of 1300K the mean holdup time of ^{21}Na in the crucible used is 6 ms for an uncollimated aperature. With the addition of long tubes the holdup time increases by $1/G$. With the long 23:1 tubes the holdup time is only 100 ms. So the requirement that $\tau_h \ll \tau_{decay}$ is well satisfied.

For long crucible exit tubes to be effective at collimating the atomic beam the mean free path, λ, of the ^{21}Na in the crucible between collisions must be large compared

to the tubes' dimensions. The vapor pressure in the target must be low for λ to be large. The MgO target has a vapor pressure of only 1×10^{-5} torr at 1227°C[52]. But the small grain of sodium oxide, 0.6 mg, that was added to the crucible to supply a ^{23}Na atomic beam increases the pressure. Most of the sodium oxide boils away as the target is heated before a run. But some ^{23}Na from the sodium oxide is still evident even after 24 hours at 900°C. This turns out to be convenient because ^{23}Na can still be trapped during the run for alignment and calibration. But the sodium vapor pressure affects the tubes' operation. It is difficult to specify an exact vapor pressure for sodium oxide because it contains three chemical species, Na_2O, Na_2O_2, and NaO_2 with dissociation temperatures of 1193K, 919K, and 825K respectively[55]. An upper limit on the vapor pressure is estimated. If the sodium oxide pressure in the crucible is 7×10^{-5} torr then 0.6 mg of material would be used in 24 hours. So the sodium oxide pressure must be less (probably much less) than 7×10^{-5} torr in order to maintain a atomic beam for more than 24 hours. The mean free path, λ, is

$$\lambda = \frac{kT}{\sqrt{2}\sigma p}. \tag{3.12}$$

The value of σ can be determined from the data that λ equals 1×10^{-3} cm for sodium at 700K and 1 torr[53]. Inputing the experiment's values of 1200K and $< 7 \times 10^{-5}$ torr into Equation 3.12 gives $\lambda \geq 20$ cm. So even with this conservative estimate the condition $\lambda \gg l$ is well satisfied.

3.3 A High Temperature Oven

Figure 3.3 shows the basics of the oven structure. The target crucible is held within the oven by a holder as described in Section 3.1. A cylindrical filament surrounds the crucible and is heated with a DC high current. Two vacuum feedthroughs are connected to the inner support rods. The electrical current flows across the thin filament and back out the outer support rods. Figure 3.4 shows the details of the filament. It is made from 1.9 cm (outer diameter) tantalum tubing, 0.76 mm thick. The middle 3.8 cm is cut in spirals to increase resistance, localizing the heating to the target. Two EMS, 7.5 V/250 A, power supplies in series provide the current. The oven was designed for high temperatures. In early tests the crucible reached the maximum temperature, 1700°C[52], for surface-to-surface stability of the alumina crucible and the tantalum filament. Inspection of the oven later revealed the filament was bonded to the crucible. Because of target sintering, see

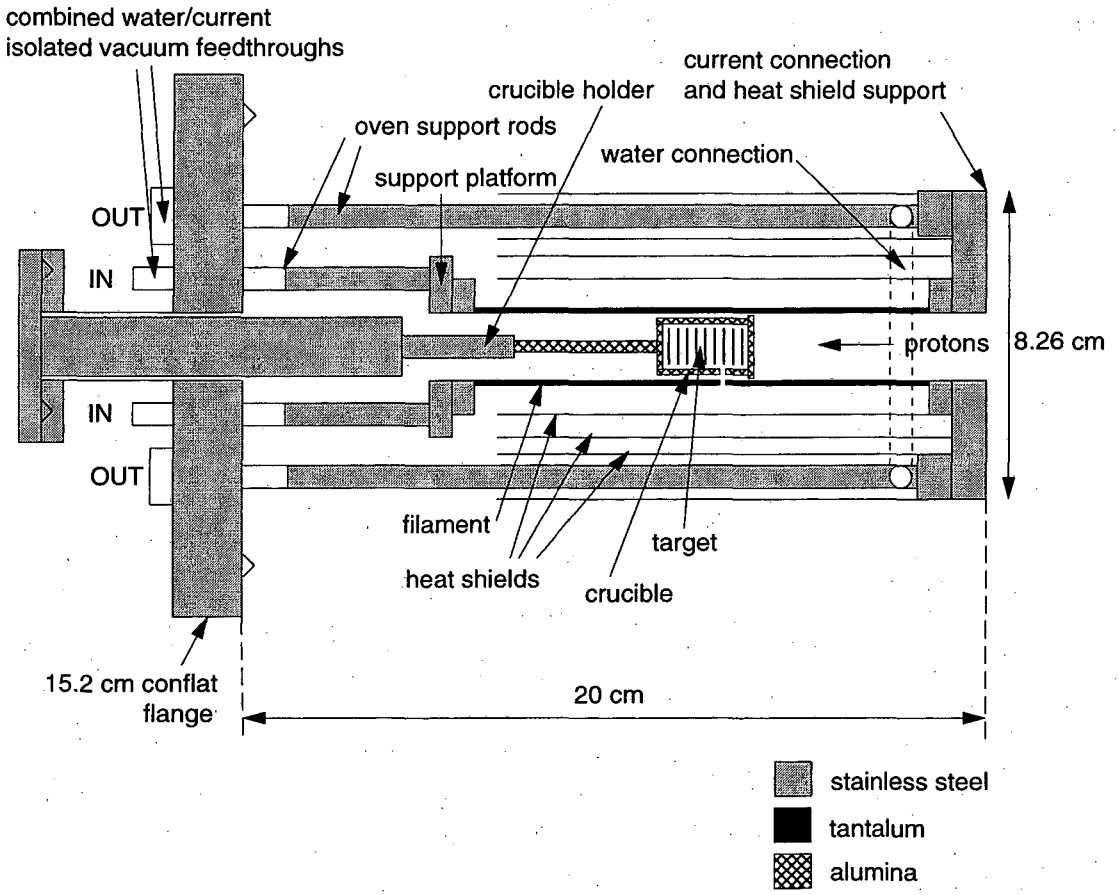

Figure 3.3: Diagram of the high temperature oven.

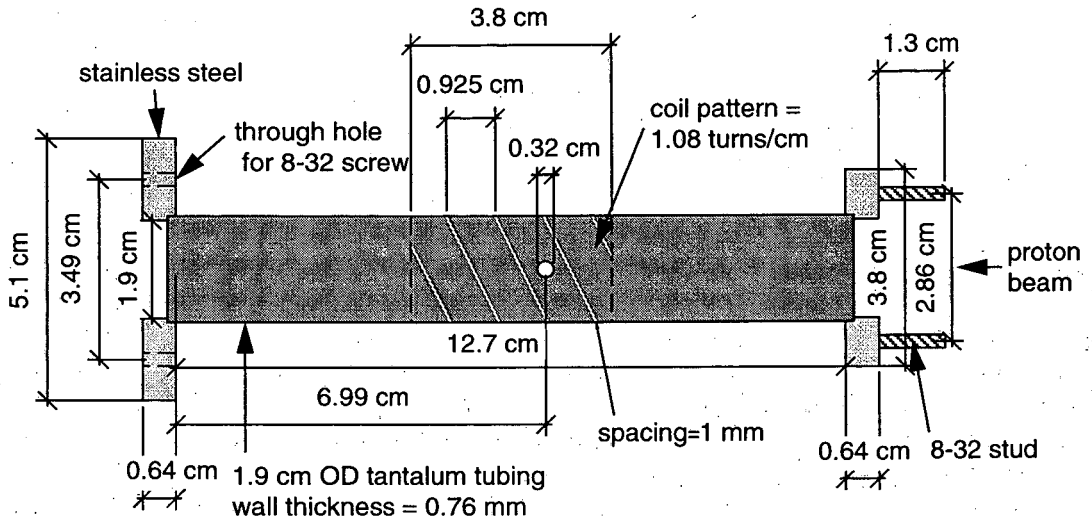

Figure 3.4: Schematic of the tantalum oven filament used for heating the target crucible.

Section 3.6, the oven is presently operated below 1000°C. A typical current and voltage setting is 105 A and 4.8 V which gives a reading of 880°C on the thermocouple at the rear of the crucible. Four layers of cylindrical heat shields surround the filament. The inner shield is tantalum and the three outer shields are stainless steel. The oven support rods are water cooled with 60 ml/s of water.

The oven structure is assembled around the target crucible after a new target is loaded and the crucible is secured to the crucible holder. The filament is placed around the crucible and attached by screws to the support platform. The heat shield support piece is then added and attached to both the filament and the outer support rod. The oven structure is inserted into the vacuum system and the vacuum seal is made at a rotatable 15.2 cm conflat flange. The proton beam hits the crucible on axis. The ^{21}Na atomic beam exits through a hole in the heat shields perpendicular to the proton beam (in the downward direction in Figure 3.3). The atomic beam is aligned with the 2 m tube connecting the target chamber to the trapping chamber. While looking down the connecting tube from the trapping chamber side the flange supporting the oven was rotated until the crucible's channeled apertures were aligned. Then the rotatable flange is fixed and the oven alignment is preserved after the target is loaded.

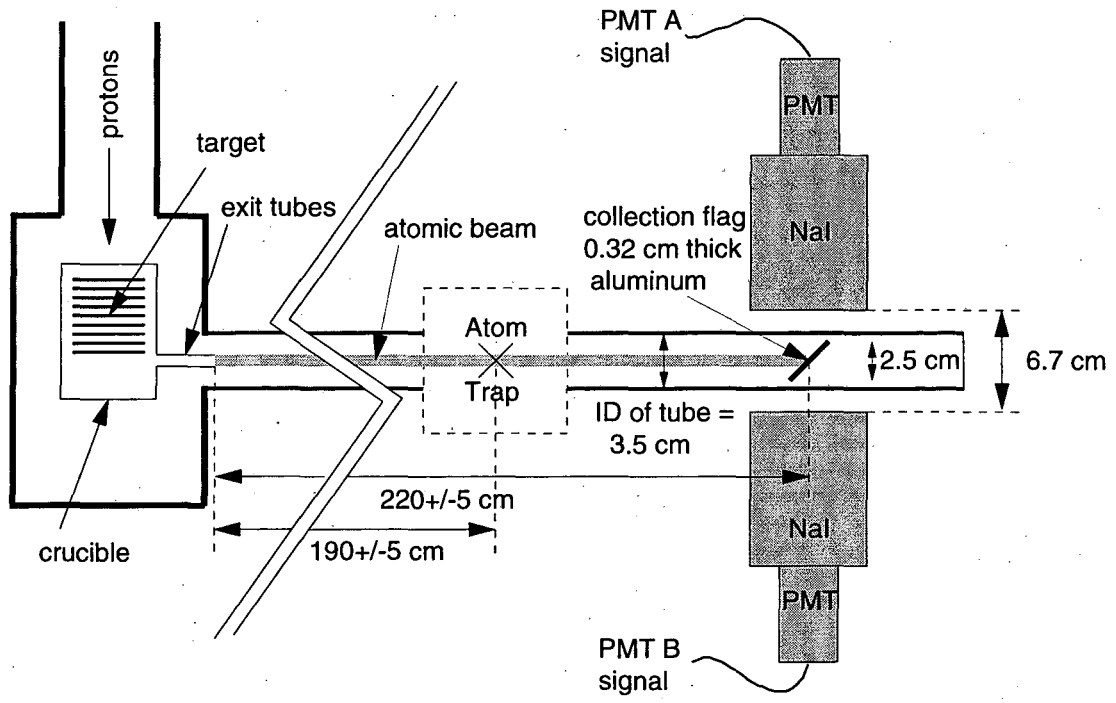

Figure 3.5: Positions and distances between the oven, collecting flag and NaI detectors.

3.4 Detection of Radioactive Atoms

The ^{21}Na atoms leave the target crucible and head down the 2 m tube connecting the target region to the trapping region. At the end of the tube, past the trapping setup, is a flag which can be plunged into the beam line to collect ^{21}Na from the atomic beam. See Figure 3.5. It is made from 0.32 cm thick aluminum which was sand blasted to roughen its surface. It is thick enough to stop a 2.5 MeV positron but has little effect on 511 keV gamma rays. The flag is oriented at 45° relative to the atomic beam so its profile to the atomic beam is 2.5 cm wide. The flag's collection area, A, is 8.0 cm^2 and it is located a distance, $d = 220 \pm 5$ cm, away from the exit tubes of the target crucible. When the ^{21}Na on the flag decays about half of the positrons enter the flag where they stop and annihilate with electrons, producing a pair of back-to-back 511 keV gamma rays. These gammas are detected in coincidence with two 7.6 cm $\times$ 7.6 cm NaI detectors whose faces are 6.7 cm apart.

Figure 3.6 shows the NaI detectors' electronics. Two photomultiplier tubes, labeled PMTA and PMTB, convert the NaI scintillation light to electrical signals. Each PMT output is split. One part is sent to an analog to digital converter (ADC1 or ADC2) which digitizes the pulse area. The photomultiplier tubes, +2000 on A and +1600 V on B, are set so that the full energy peaks of the 511 keV gammas are in about channel 500 of the ADC's. The other part of the split signal goes to a coincidence logic circuit. Each signal is first amplified and discriminated. The hardware coincidence window is 0.5 μs. Coincidences occuring during the count gate time and while the controller is not busy are delayed 110 μs and then sent to the interrupt register which informs the crate controller that an event is waiting. A time to digital converter, TDC1, records the difference in arrival times of the two PMT pulses. The time of arrival of a coincidence is recorded with scaler 2. Scaler 2 is reset at the beginning of each counting period. Scaler 1 counts the total number of events, processed or not. A Macintosh Quadra 950 computer controls the data acquisition through a MAC-CC 392 crate controller. A data run consists of two time periods which are repeated as many times as desired. First the proton beam is on during the beam gate time and then detector coincidences are recorded during the count gate time. For each coincidence event the readings on ADC1, ADC2, TDC1 and scaler 2 are recorded. At the end of a data run scaler 1 is recorded. The events are stored on the computer for post-run data analysis.

The NaI detectors were calibrated with a ^{22}Na source of known activity, 1.59 d/s. The ^{22}Na source was on a thin metal backing of negligible thickness which was 2.5 cm in diameter. It was taped to the center of the flag. ^{22}Na is a positron emitter with an endpoint energy of 0.54 MeV. The decay positrons are stopped in the flag just as they are in the case of ^{21}Na. The annihilation radiation is then used to calibrate the detectors. One error in the equivalence of ^{21}Na and ^{22}Na is the different rates of backscatter from the aluminum flag for the different energy spectrums of positrons. The lower energy positrons from ^{22}Na will scatter more compared to the ^{21}Na positrons resulting in an undervalued efficiency of the system for ^{21}Na. Backscatter rates in aluminum range from 4% at 2.5 MeV to 13% at 0.1MeV[56]. A 5% error is included in the efficiency result for this effect. The resulting efficiency, e, of the detectors is 10.0±0.5%. The deadtime of the system was measured to be 180±20μs. For fast decay rates a correction must be made to find the actual rate, R_{act}, from the system's rate, R_{sys}. The correction is

$$R_{act} = \frac{R_{sys}}{1 - t_d R_{sys}}. \tag{3.13}$$

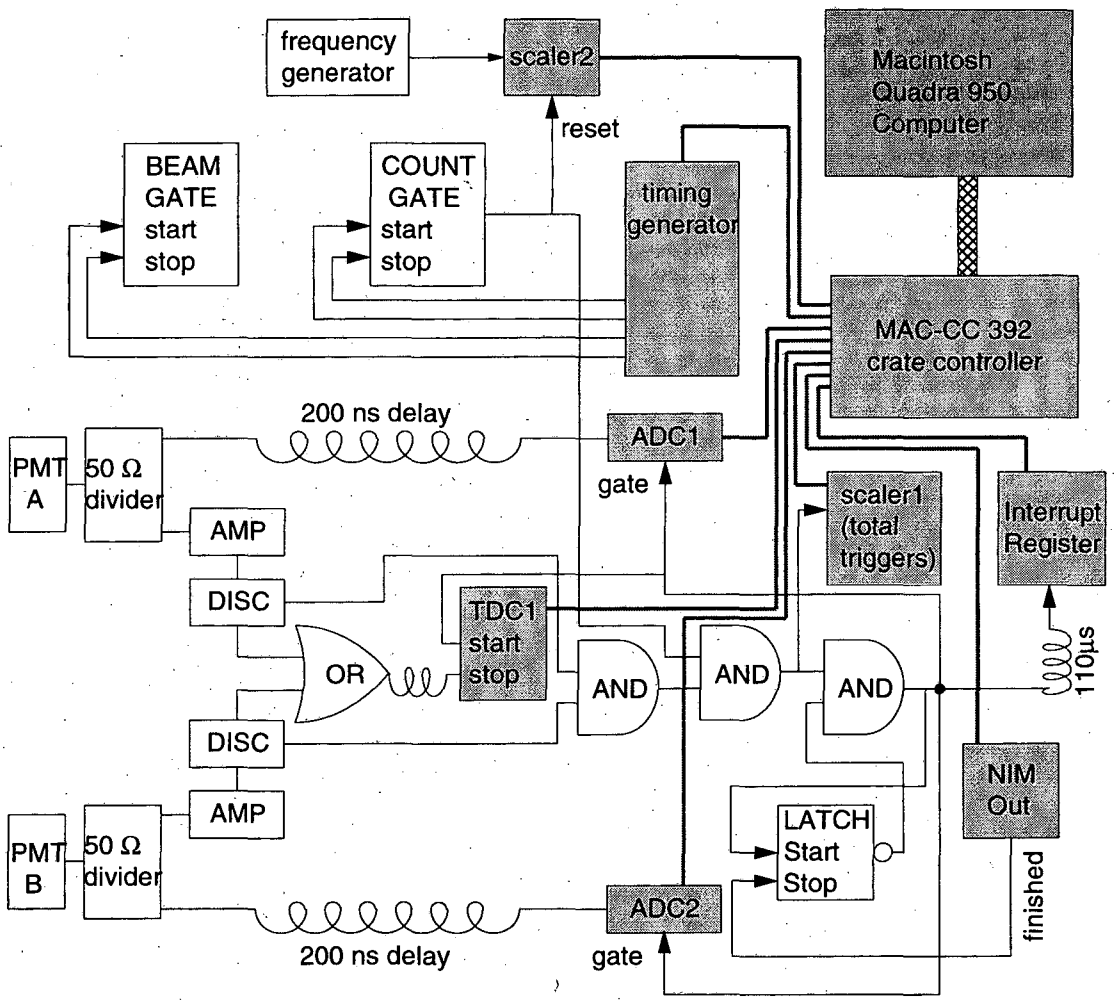

Figure 3.6: Electronics for detecting ^{21}Na condensed on the collection flag.

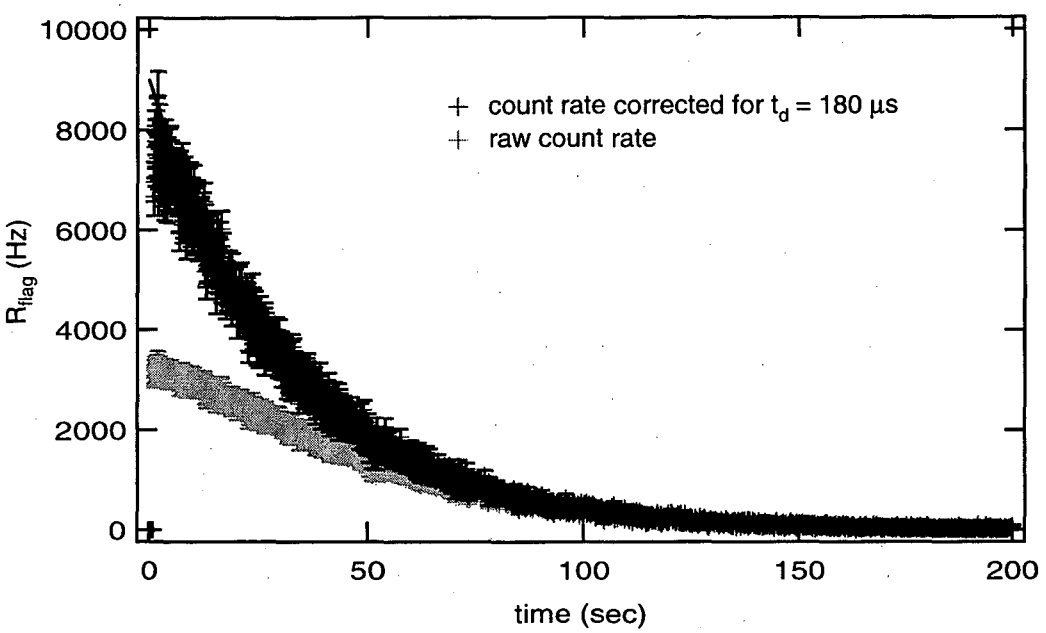

Figure 3.7: Graph of the ^{21}Na counts on the collecting flag for run 4 of the "Tubes" Run.

For a system rate of 1000Hz the correction is 20% and the actual rate is 1200 Hz.

To reduce systematic error a cycling procedure is used. The proton beam is on for 60 sec and the ^{21}Na is collected on the collecting flag. Equilibrium is reached after about 60 sec or about three half-lives. The rate at which ^{21}Na is added to the flag equals the rate it decays. When the proton beam is off the decay rate is counted as a function of time. The signal rate decays with the 22 second half-life of ^{21}Na. Extrapolating back to $t = 0$ gives the equilibrium rate. Figure 3.7 shows data from run 4 of the "Tubes" Run[1]. The lower curve is the raw count rate detected on the flag as a function of time. The upper curve is the raw data corrected for 180 μs of deadtime using Equation 3.13. Only the data below 1000 Hz, where the deadtime correction is below 20%, was fit to determine the initial rate on the flag. The fit over the entire time range is shown, however. For this run $R_{flag} = 9000 \pm 300$ Hz.

From the equilibrium detection rate on the flag the total production rate, R_{tot}, of

[1]Every cyclotron beam time was assigned a run name, in this case "Tubes". Individual tests within a beam time were numbered.

Symbol	Description	Value
A	area of catching flag	8.0 cm^2
d	distance from oven aperture to flag	220±5 cm
d'	distance from oven aperture to trap center	190 ± 5 cm
e	detection efficiency	$10.0 \pm 0.5\%$
G	Clausing G-factor for 23:1 tubes	1/17
R_{flag}	equilibrium decay rate on flag	9000 ± 300 Hz
s	probability that the ^{21}Na sticks to the flag	1
$\rightarrow$		
$R_{tot} = (1.0 \pm 0.1) \times 10^8$ atoms/s*		
$F_{trap} = (1.5 \pm 0.1) \times 10^4$ atoms/cm^2s*		

*rates given the assumptions stated in the text

Table 3.2: Inputs to Equations 3.14 and 3.15 and the resulting values.

^{21}Na leaving the target crucible can be calculated. The total production rate is

$$R_{tot} = \frac{\pi d^2 G R_{flag}(0)}{Ase}. \tag{3.14}$$

The geometric and efficiency values of the experiment used in Equation 3.14 are listed in Table 3.2. The value of s, the fraction of ^{21}Na in the atomic beam that sticks to the flag, used is 1. It is likely to be less than 1. Reference [51] claims 80% for sand blasted aluminum. By using $s = 1$ in Equation 3.14 a lower limit on the total production rate is found. The value of G used in Equation 3.14 assumes the maximum collimation possible with 23:1 crucible exit tubes. Again a lower limit on the total production rate is found with this assumption. For the "Tubes" Run data shown in Figure 3.7 the total production rate, R_{tot}, is $(1.0 \pm 0.1) \times 10^8$ atoms/sec. The ^{21}Na flux, F_{trap}, at the trap which is a distance d' from the crucible exit holes is

$$F_{trap} = \frac{R_{flag}(0)}{Ase} \cdot \frac{d^2}{d'^2}. \tag{3.15}$$

For the "Tubes" Run, $F_{trap} = (1.5 \pm 0.1) \times 10^4$ atoms/cm^2s. Note that this rate was measured without transverse cooling of the atomic beam.

3.5 Predicted Production Rate of ^{21}Na

The ^{21}Na is produced with the ^{24}Mg(p,α)^{21}Na reaction using the ^{24}Mg nuclei (80% natural abundance) in the MgO. The cross section of the reaction has been previously

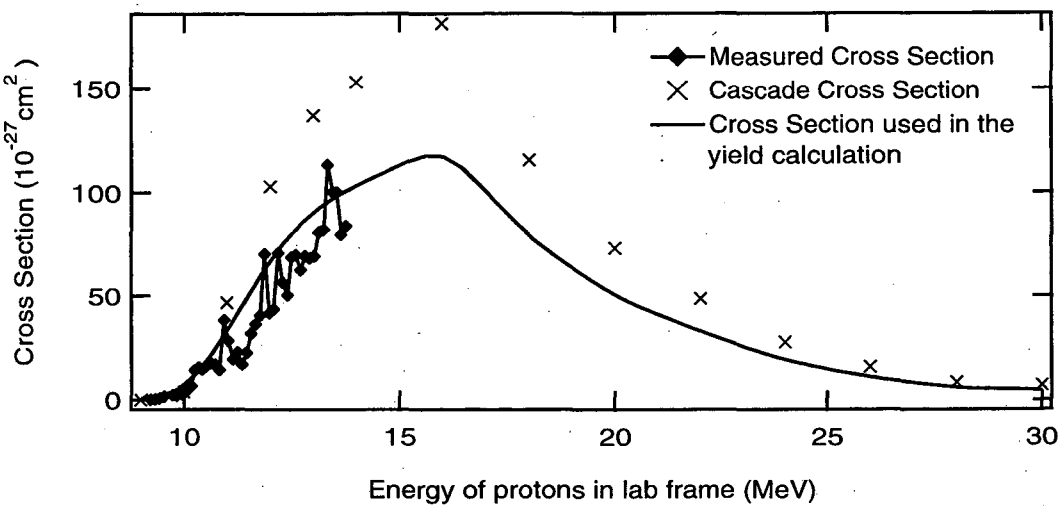

Figure 3.8: Cross sections for the ^{24}Mg(p,α)^{21}Na reaction.

measured, but only up to proton energies of 13.75 MeV[57]. Figure 3.8 shows the results. It is expected that a significant cross section extends beyond 14 MeV. Figure 3.8 also shows the cross section computed with the CASCADE code[58]. CASCADE computes the cross section for the compound reaction. The reaction is modeled as the formation of a compound nucleus which has various probabilities for decaying to possible final states. Direct contributions to the cross section are ignored. To estimate ^{21}Na production above 14 MeV the solid line cross section in Figure 3.8 is used for the cross section. This curve is the CASCADE cross section renormalized to fit the experimental data at low energies. The ^{21}Na yield resulting from this cross section is a rough estimate.

The production rate, P, of ^{21}Na is

$$P = nR \int_{E_1}^{E_2} \sigma(E) \frac{1}{dE/dx\,(E)} dE. \tag{3.16}$$

The parameters used in Equation 3.16 are listed in Table 3.3. The stopping power, dE/dx, for protons in MgO[59] is shown in Figure 3.9. The computed production rate as a function of energy, shown in Figure 3.10, corresponds to 1μA of protons stopped in a thick target. For this experiment the protons slow from 21 MeV to about 12 MeV in the target as shown by the dotted lines in Figure 3.10. For 1 μA of protons the expected production is therefore 2×10^9 ^{21}Na/s.

Symbol	Description	Value
a	atomic weight Mg+O	40.3 g
α	natural abundance of ^{24}Mg	80%
E	energy of proton in the lab frame	12-21 MeV
dE/dx	stopping power	see Figure 3.9
N_A	Avogadro's number	6.02×10^{23}
$n = N_A\alpha/a$	^{24}Mg sites per gram MgO	1.2×10^{22} 1/g
R	number of protons per second	$1\mu\text{A} = 6.3 \times 10^{12}$ 1/s
σ	cross section for ^{24}Mg(p,α)^{21}Na	see Figure 3.8

Table 3.3: Inputs to the calculation of ^{21}Na production.

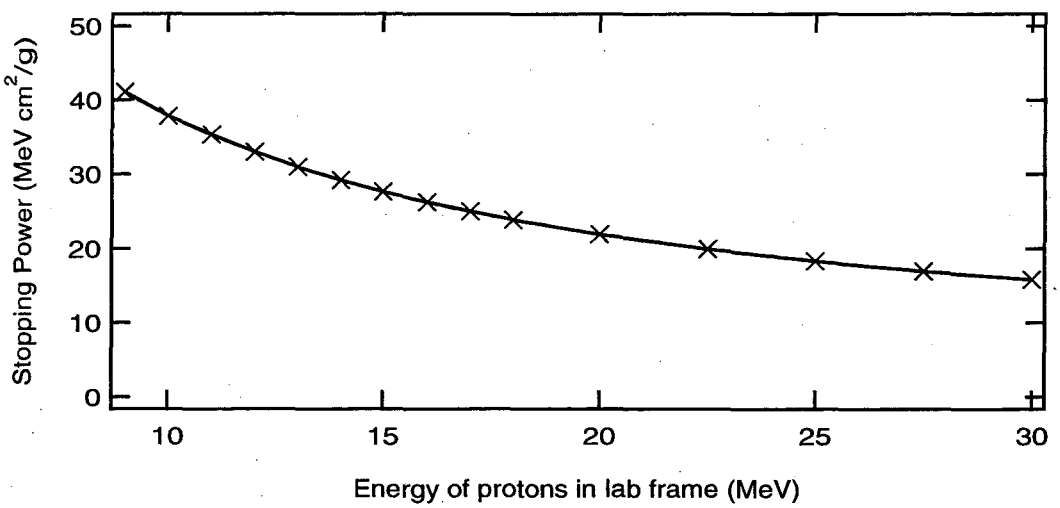

Figure 3.9: Stopping power of protons in MgO.

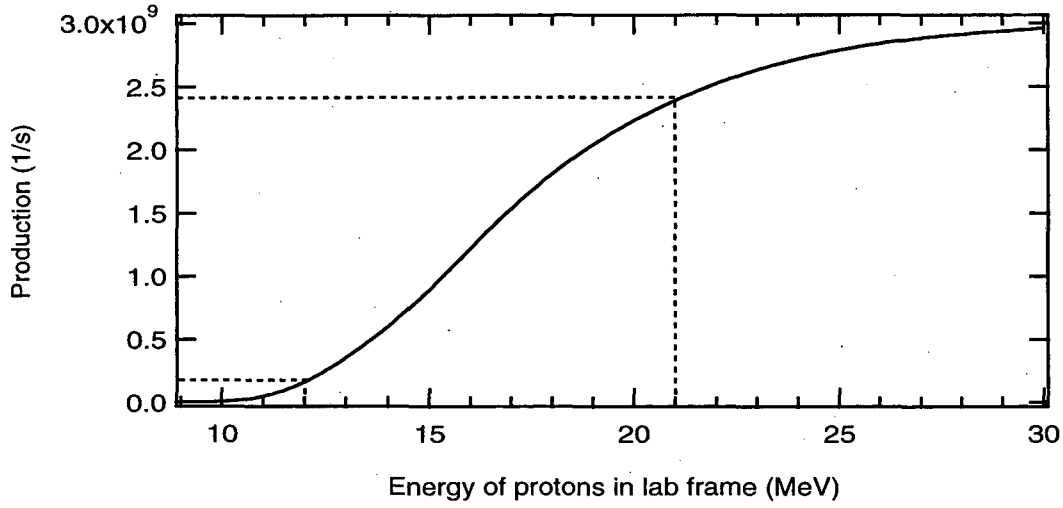

Figure 3.10: Production of ^{21}Na by the ^{24}Mg(p,α)^{21}Na reaction with 1 μA of protons hitting a thick MgO target.

3.6 Experimental Production Runs

The target apparatus is located at the end of the 3C beamline in cave 3 at the 88″ cyclotron at Lawrence Berkeley National Laboratory. Figure 3.11 shows the layout of the 3C beamline. In a typical run 1-2 μA of protons exit the cyclotron and are measured on the beam stop directly outside the cyclotron labelled BS2. A good beam tune gives 90-95% transmission from BS2 to a Faraday cup, FC3C2, which is located 20 cm in front of the target oven. Although FC3C2 is not fully electron suppressed it reads only a few percent high for penetrating 25 MeV protons so about 900 nA of protons hit the target. Typically a final beam tune is done by maximizing the proton current reading from a target. But for this experiment the heated target boils off so many electrons that the proton current is swamped by background. A different alignment procedure is required. Using the readings from a beam tune with the target cold the cyclotron operator tunes the beam close to the target center as measured on a phosphor screen, PH3C2, located 20 cm in front of the target. The phosphor is plunged into the proton beam to observe the beam profile. The typical image viewed by the camera monitor is shown in Figure 3.12. The spot is about 0.5 cm in diameter with 0.25 nA of current on BS2. Figure 3.12 shows the approximate beam spot location on PH3C2 for good allignment of the proton beam on target. Once the beam

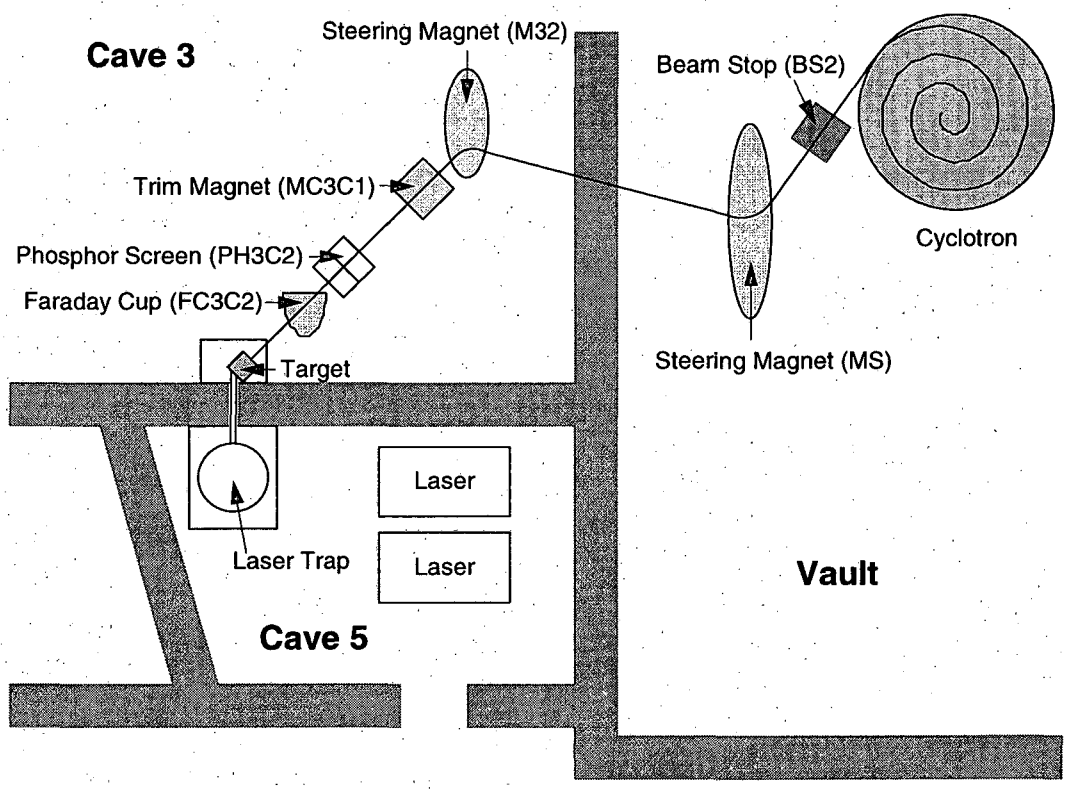

Figure 3.11: Layout of the 3C beamline with the locations of the beamline elements mentioned in the text.

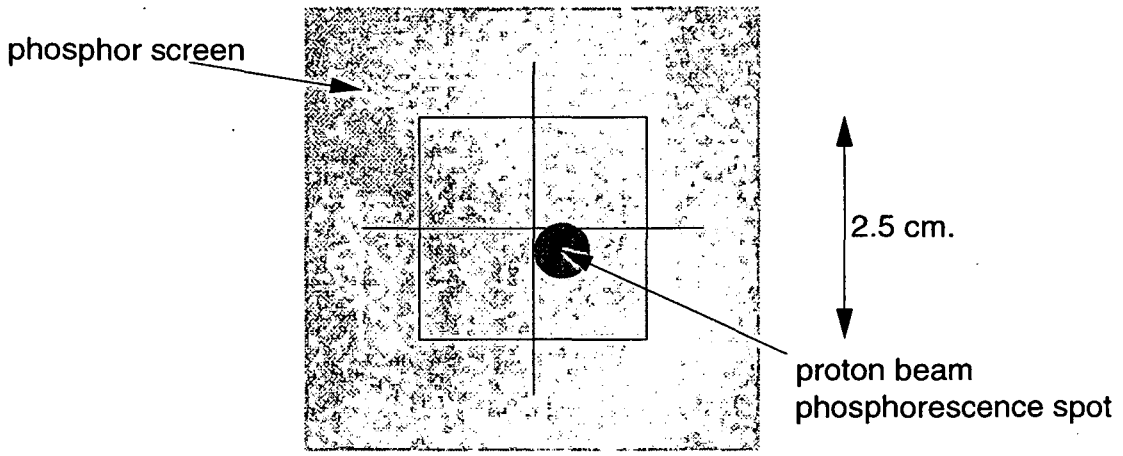

Figure 3.12: Correct position of the proton beam spot on the phosphor screen, PH3C2. The perspective is that of the protons heading toward the target.

position is adjusted on PH3C2 the production of ^{21}Na with 1 μA of proton current (as read on BS2) is measured. The beam is then displaced up/down and right/left by changing the currents in the trim magnet MC3C1 which is 1.5 m upstream from the target by tenths of amps. Production is monitored at each setting and the final setting is where the ^{21}Na production is maximized. Table 3.4 lists the cyclotron runs mentioned in this thesis.

We made a series of tests with different targets to arrive at the best target configuration. This section describes the process in which different target and crucible geometries were tested at varied temperatures to find the parameters for the highest continuous ^{21}Na production. Sintering of the target, diffusion of activity in the target and implementation of passive collimating tubes were important points. The best attempts are made to be quantitative but this is not always possible. Qualitative pictures were important, especially for understanding the diffusion of activity out of the target.

Once ^{21}Na is produced in the target it must diffuse out of the individual powder grains and through the bulk material to reach the exit apertures. Sintering, the combining of small powder grains to form larger grains as the target is heated, slows this process. The best temperature where the powder remained unsintered consistent with the fastest possible diffusion rate was found in production tests. In one run the sintering temperature was dramatically overshot. A target of about 10 g/cm^2 of MgO powder was lightly pressed

Run Name	Date	Comment
Reich	4/3/96	target development
Incoherent	6/3/96	target development
Coherent	6/14/96	target development
Stacked	7/20/96	target development
Aerospace	8/1/96	target development
Tubes	10/14/96	target development
Lonely	5/30/97	hyperfine measurement
Vortex	4/30/98	beta decay
Wedding	6/1/98	beta decay
Foamed	10/4/98	target development

Table 3.4: List of the cyclotron runs mentioned in this thesis.

into a cylinder and heated to about 1600°C during a beam run. As a result it shrunk to a small cylinder with half the dimensions of the original cylinder. In general an increase in ^{21}Na atomic beam production with temperature was observed. At a temperature of about 1200°C a sudden rise in production occurred but was unsustainable. Upon returning to lower temperatures the ^{21}Na detection rate was substantially below the rate measured at the same temperature before heating the target. Figure 3.13 shows such a time line for one run. Repeated production measurements were taken over time as the oven was slowly heated. The amount of ^{21}Na diffusing out of the oven and entering the atomic beam increased with temperature initially as shown in Figure 3.13. But once the oven temperature was raised to about 1200°C the production gradually decreased over time. Later experiments established that if the temperature during a run is kept below 1000°C the production rate is sustainable and visual inspection of the target after the run shows no evidence of sintering.

In an attempt to understand diffusion rates we developed a measurement technique using the trapped atoms. In steady-state operation the optical trap continually loads from the atomic beam and loses atoms from collisions of trapped atoms with background gas atoms. Figure 3.14 shows data taken at about 1200°C during the "Reich" Run. The top graph shows the decline of trapped ^{21}Na after the atomic beam is blocked. The trapped atoms decay with a half-life of 8 seconds. The bottom graph in Figure 3.14 shows the decline of the trap after the proton beam is shut off. The delay in the trap decay is a result of ^{21}Na loading into the trap from atoms that continue to diffuse out of the target. As can be seen from Figure 3.14, the difference in the two trap decay times is small. After the proton

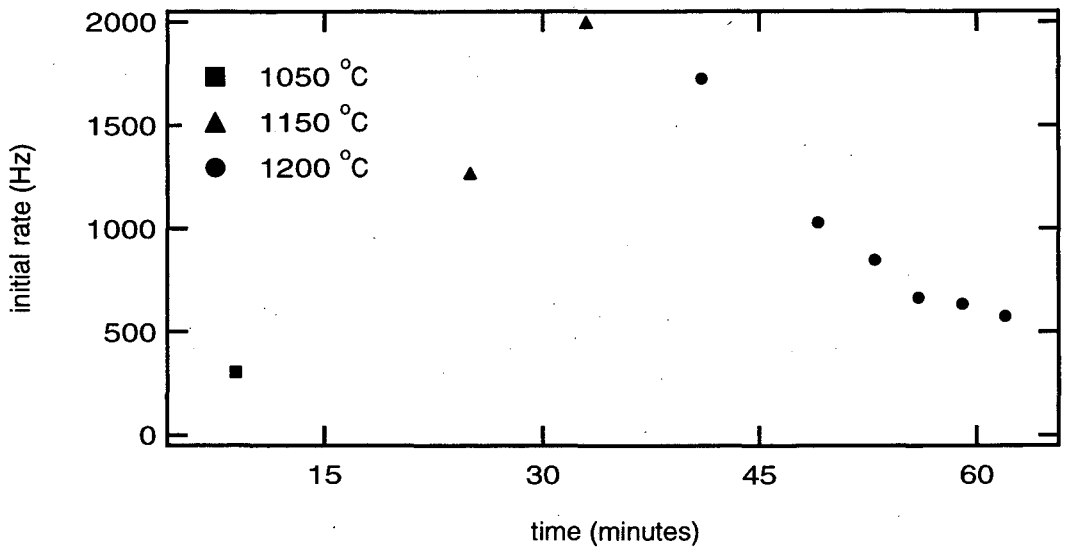

Figure 3.13: Data on the sintering of the target. The sintering of the target over time caused a reduction in ^{21}Na release from the target.

beam shuts off little ^{21}Na continues to diffuse from the target. The data in the bottom graph of Figure 3.14 are fit with a curve which is the solution to the decay in the number of trapped atoms as the trap continues to be loaded with an exponentially decreasing source proportional to $e^{-t/\bar{t}_d}$. The fit gives a mean diffusion time, $\bar{t}_d$, of 1.1±0.5 sec. The total diffusion rate from the target is high compared to the decay rate of ^{21}Na.

The expectation is that most of the ^{21}Na will diffuse out of the target before it beta decays. This conclusion was contradicted by the estimated amount of ^{21}Na made which actually left the oven, about 1%. Understanding this discrepancy helped us make a better target. The important realization is that a small number of atoms near the surface of the target diffuse out much faster than the atoms in the bulk. A simple one dimensional model illustrates this mechanism. The activity per unit length, u, in a cylinder of length l will redistribute according to the diffusion equation,

$$\frac{\partial u}{\partial t} = D\frac{\partial^2 u}{\partial x^2}, \tag{3.17}$$

with D being the diffusion constant. If the activity is initially created evenly throughout the cylinder then the total fractional amount remaining in the cylinder, $U_{tot} = \int_0^l u\,dx$, after

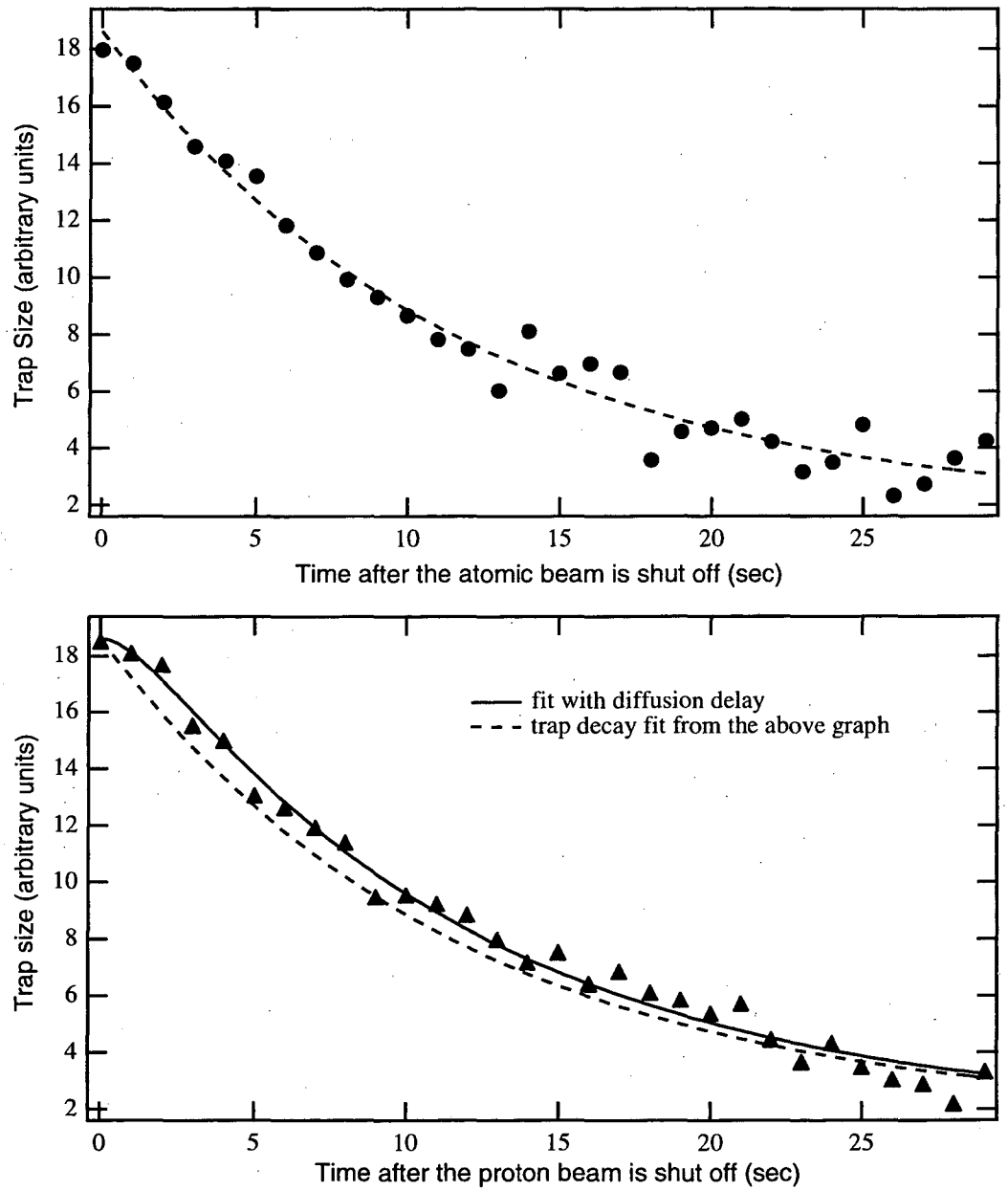

Figure 3.14: Graphs of the number of trapped atoms after the atomic beam is shut off (top graph) and after the proton beam is turned off (bottom graph).

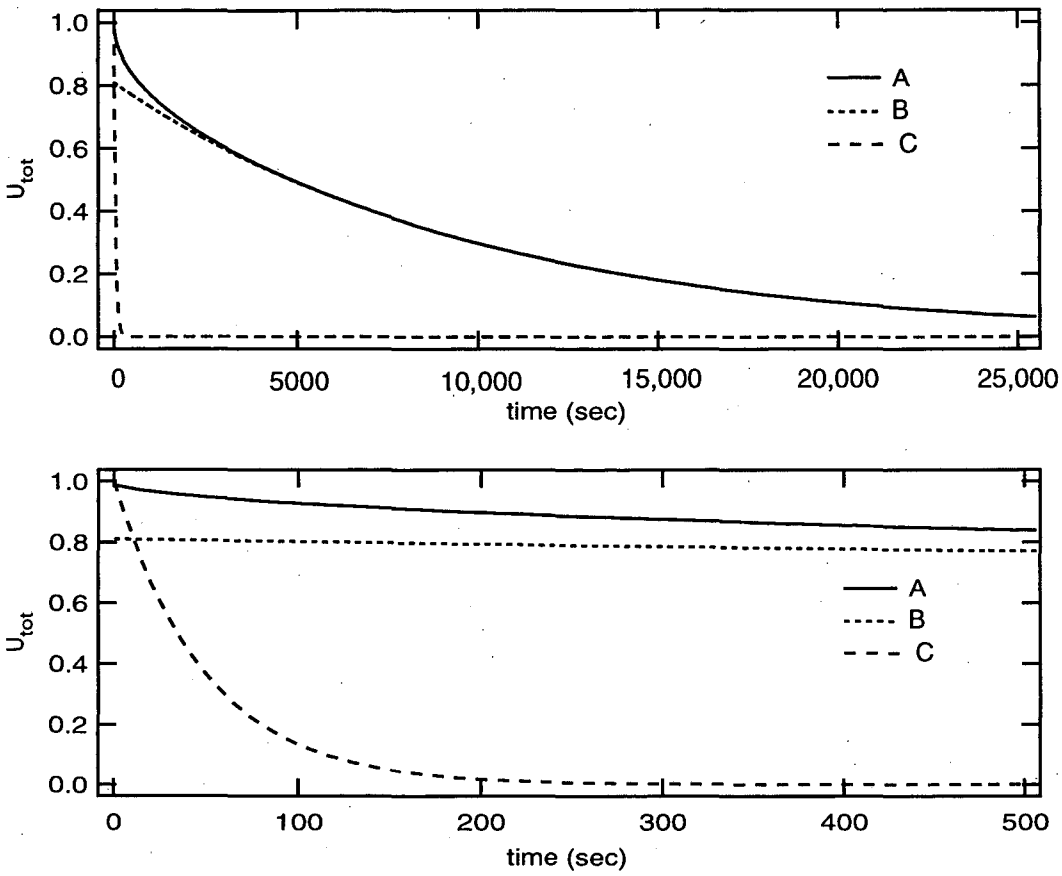

Figure 3.15: Model of the fraction of activity, U_{tot}, remaining in the target as a function of time for various senarios.

a time, t is (see for instance [60])

$$U_{tot}(t) = \frac{8}{\pi^2} \sum_{n=odd} \frac{1}{n^2} e^{-n^2 t/\tau_d}. \tag{3.18}$$

The diffusion time, τ_d, is related to the diffusion constant, D, by

$$\tau_d = \frac{l^2}{D\pi^2}. \tag{3.19}$$

Most of the atoms diffuse in a time τ_d but small amounts come out much faster due to the higher terms in Equation 3.18. Figure 3.15 shows the value of U_{tot} from Equation 3.18 with τ_d=1 $\times$ 10^4 sec. The two graphs show the same curves with different time scales. This

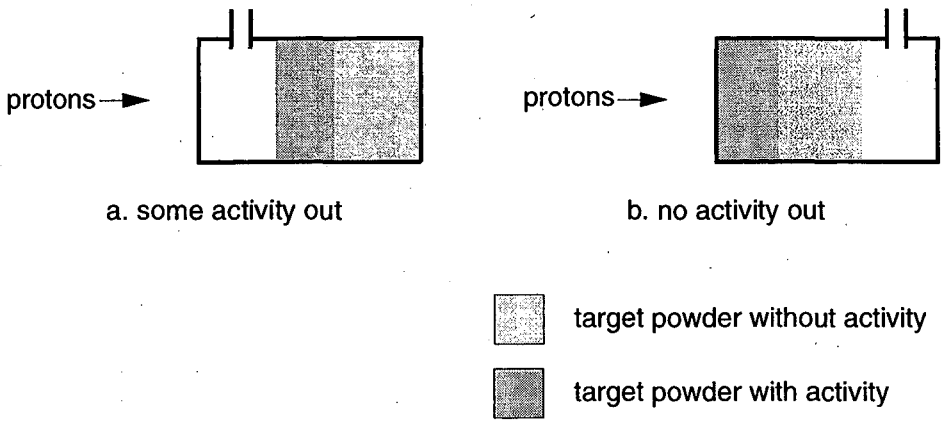

Figure 3.16: The placement of the target and crucible exit tubes relative to the proton beam in two test runs.

value of τ_d allows about 1% of the activity to be released in 20 sec. Curve A shows the first 17 terms of Equation 3.18. Curve B shows the contribution of only the first term of Equation 3.18. The fast release of activity at the beginning is mainly due to the higher terms. When an exponential decay curve is fit to the first 50 seconds of curve A a much shorter effective diffusion time of 50 sec is found. As shorter time spans closer to $t = 0$ are examined even shorter decay times are found. For demonstration Curve C shows the fractional amount of activity remaining in the target if U_{tot} with τ_d=50 sec is graphed. This demonstrates how using the initial decay rate to determine the diffusion time grossly underestimates the amount of time it takes for most of the ^{21}Na to diffuse. The actual times can be thousands of times longer.

We established that diffusion through the bulk target is slow during a run when the crucible orientation was reversed. The crucible apertures were placed downstream of the target in this run. Figure 3.16 shows the orientations of the target and crucible apertures. In previous target tests the MgO powder was gently pressed into the back of the crucible. Plenty of MgO was used so the protons stopped midway through the target and the actual production of ^{21}Na only occurred in the front section, as illustrated by the darker gray in Figure 3.16a. In the new configuration (Figure 3.16b) the powder was inserted in the front of the crucible. The activity had to diffuse through all of the rest of the powder to leave the

Run Name	Cycle Number	Temp. (°C)	Tubes *l:d*	Target Description	Flag Rate $R_{flag}(0)$ (Hz)	Total Rate* R_{tot} (Hz)
Reich	10	960	3:1	bulk	170 Hz	1.4×10^7
Coherent	4	1050	3:1	5 MeV	250 Hz	2.1×10^7
Stacked	5	980	8:1	stacked	1300 Hz	4.1×10^7
Aerospace	11	950	8:1	stacked	2900 Hz	9.2×10^7
Tubes	4	950	23:1	stacked	9000 Hz	1.0×10^8

* Using Equation 3.14.

Table 3.5: ^{21}Na atomic beam production for given runs normalized to 1μA of protons on BS2.

crucible and no ^{21}Na was detected outside the crucible on the collecting flag. ^{24}Na is also produced in the MgO target during runs by the ^{25}Mg(p,2p)^{24}Na reaction. It has a half-life of 15 hours so the target can be dissected and checked for ^{24}Na the day after a test run. A germanium detector was used to look for the characteristic gamma rays of ^{24}Na at 2.75 MeV and 1.37 MeV in the different sections of the target. The target portions near the crucible's aperture contained much less ^{24}Na than the portions on the upstream side. During the two hours that the target oven remained hot after production ^{24}Na diffused through the target. It moved only a small distance during that time. The conclusion from these observations is the bulk diffusion rate is "slow".

The qualitative information that the diffusion through the bulk powder is extremely slow but that activity close to the surface comes out much faster than the rest was the basis of a new target design. A stack geometry described in Section 3.1 gives as much surface area as possible. There is enough MgO to exploit the large production cross section energy range but there is no extra material through which the ^{21}Na must diffuse. An even more open target geometry could improve the extraction of ^{21}Na further. It appears that the target must be based on powder, however. An open, spongy form of sintered MgO was tested in the "Foamed" Run. The material was a reticulated MgO ceramic with an average pore size of about 0.5 mm and a density of 0.4 g/cm^3. A 0.4 g/cm^2 thick target of this material yielded no detectable (< 10 Hz flag rate) ^{21}Na in the atomic beam.

The production numbers for some of the target test runs are listed in Table 3.5. It is hard to compare numbers from different runs with different targets, temperatures and proton beam tunes. Table 3.5 is an attempt to record the results in order to a give a quantitative description of the improvements in production. Comparisons are made at

temperatures of about 1000°C where the target remained unsintered. In addition, all production values are from data runs before any tests at higher temperatures were made. In some runs higher yields occurred at higher temperatures but as discussed earlier these yields were unsustainable.

For the trapping experiment the important column in Table 3.5 is the "flag rate". It indicates how much ^{21}Na is delivered to the trapping region. An increase in this number directly translates to an increase in the number of trapped atoms. Two main factors contributed to the increase in the flag rate. The change in the target from a bulk powder to a lightly pressed stack of target discs allowed more ^{21}Na to diffuse out of the target. Long exit tubes increased the used forward ^{21}Na flux. Unfortunately because of the limited number of beam times more than one change was often made from one beam time to the next. It would be nice to have systematic data after each individual change.

The final column in Table 3.5 lists the total production rate of ^{21}Na leaving the crucible using Equation 3.14. The increase in this number represents the improvement remaining after the maximum improvement due to the collimating tubes is taken out. This improvement is due to the better target design in which the total rate of ^{21}Na coming out of the oven increases. The assumption that the tubes work according to theory is supported by the increase in the flag rate between the "Aerospace" and "Tubes" Runs which had essentially the same targets.

The target for the "Reich" Run was a bulk target with plenty of MgO pressed into the target crucible with the geometry of Figure 3.16*a*. In the "Coherent" Run the amount of MgO powder in the crucible was greatly reduced so its stopping thickness for protons was only 5 MeV. The powder was kept as fluffy as possible. Although less than half of the production cross section was used more ^{21}Na exited the crucible than in the "Reich" Run. The ^{21}Na diffuses faster through the fluffy powder. The next step in development was a stacked target. Although ideally the discs would be fluffy powder they must be pressed to hold together. The stacked geometry increased the total rate by a factor of two. In the "Aerospace" Run the target was pressed more lightly than the "Stacked" Run resulting in an even higher total rate. The improvement in the flag rate between the "Aerospace" and "Tubes" Runs can be attributed to the longer tubes because the target remained basicly the same. Equation 3.9 predicts a factor of 23/8 improvement between the runs. The improvement observed was a factor of 3 so the tubes did their job. Longer tubes may still be possible to collimate the atomic beam further as the experiment's parameters are

well within the theoretical criteria listed in Section 3.2. However, centering the collimated atomic beam down the tube connecting the target to the trap will become more difficult. With the present 23:1 tubes, allignment to about 1° is needed. The total increase in the flag rate due to target improvements was a factor of 50. A factor of 7 came from better target design. The other factor of 7 very likely came from the collimating tubes; an increase of 23/3 is expected from theory.

The extraction efficiency, the fractional amount of the ^{21}Na created that leaves the crucible, can be estimated. In the "Tubes" Run, 1 μA of protons was measured on BS2 so about 900 nA of protons hit the target. Assuming the cross section from Figure 3.8 the production of ^{21}Na in the target was 2.0×10^9 Hz. Using an 80% flag sticking probability in Equation 3.14 gives 1.3×10^8 Hz of ^{21}Na leaving the oven crucible. Taking the ratio of the total out to the total made gives an estimate of the extraction efficiency of 7%. This chapter described all of the assumptions going into this estimate of extraction efficiency. The flag sticking probability, the tubes operation effectiveness, the Faraday cup reading efficiency and especially the production cross section are not precisely known. With all this in mind this estimate is probably good to about 50%.

Chapter 4

The Laser Trap

4.1 The Lasers and the Optical System

Lasers at the atomic resonance wavelength for sodium, 589 nm, are required for making a laser trap containing sodium atoms. Laser light at 589 nm is created with an argon ion laser pumped dye laser. Two dye lasers are used. Laser 1 is a Coherent 899 ring dye laser pumped with 6 W of the single 514 line from a Coherent Innova 400 Ar^+ laser. Laser 2 is a Coherent 899 ring dye laser pumped with 6 W of all lines of a Coherent Innova 300 Ar^+ laser. We use Rhodamine 6G dye. The power outputs for laser 1 and laser 2 running single mode with a linewidth of about 1 MHz (FWHM) are about 800 mW and 600 mW respectively. An external lock signal derived from the saturated absorption spectroscopy of stable ^{23}Na is fed into the external lock input of each laser to stabilize the lasers at the desired atomic transition frequency.

Figure 4.1 shows the saturated absorption spectroscopy set-up. The output beam of the laser is divided with a beam splitter, BS1, and 10% of the power is directed into the saturated spectroscopy part of the optical set-up. The resonant frequency of ^{21}Na relative to ^{23}Na is lower by 1648 MHz because of the isotope shift, requiring additional compensation. The spectroscopy beam is therefore passed twice through an acoustic optic modulator, AOM1, set at +824 MHz before entering the spectroscopy cell. The unshifted, 0^{th} order beam from AOM1 is for locking to ^{23}Na frequencies. The frequency shifted or unshifted beam is aimed into the spectroscopy cell depending on whether the lasers need to be locked to the ^{21}Na or ^{23}Na resonant frequency.

A 0.6 cm thick glass plate, BS2, causes two probe beams to pass through a cell

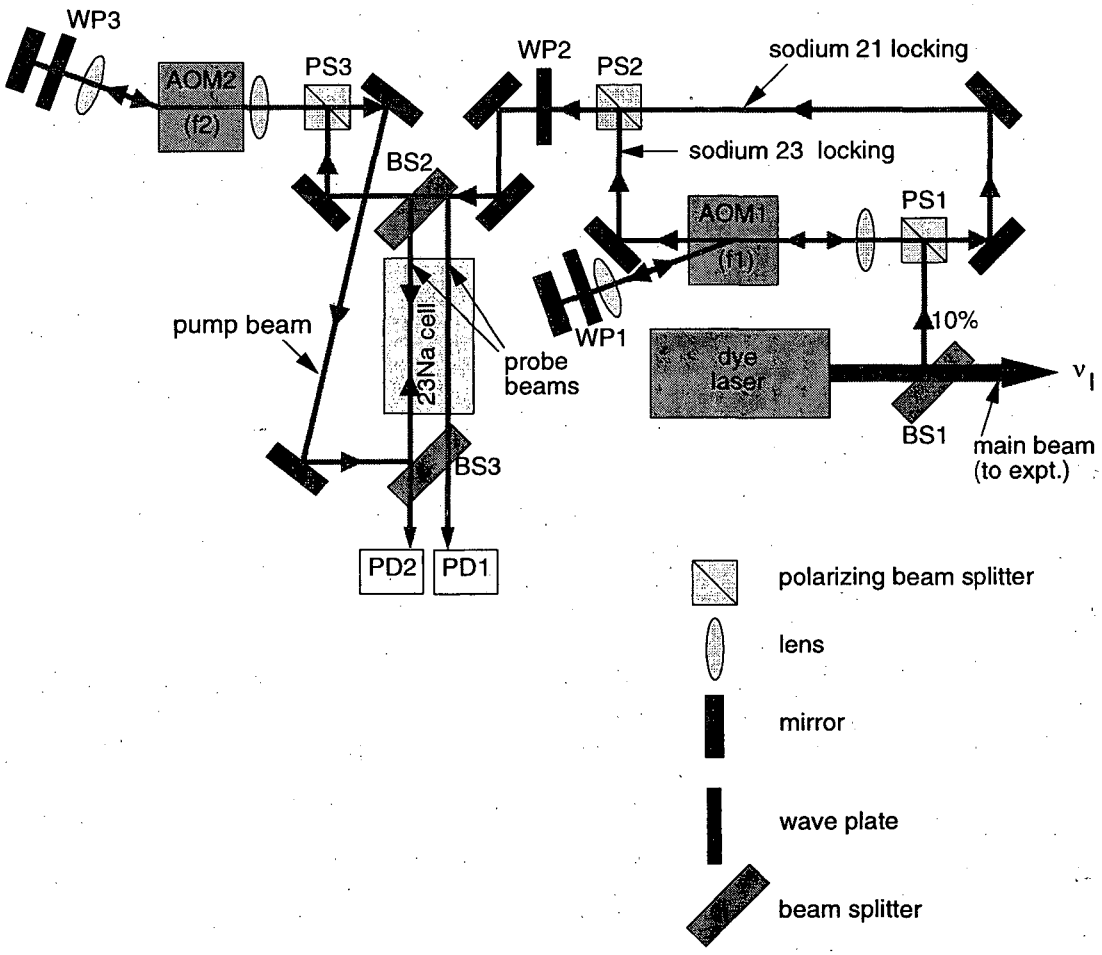

Figure 4.1: The saturated spectroscopy set-up used to derive the laser lock signal.

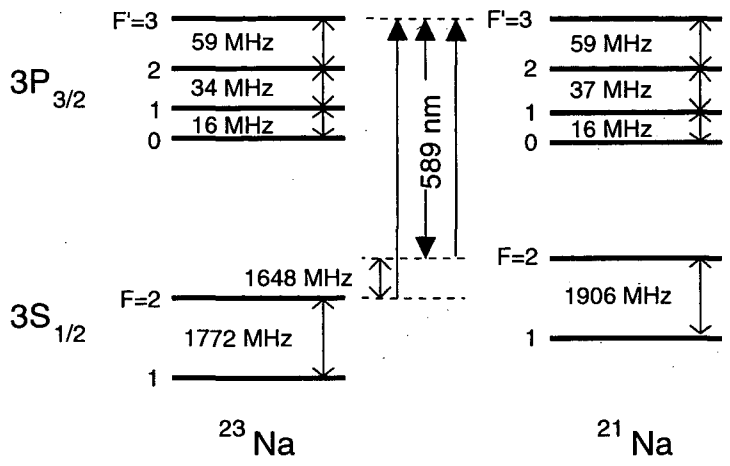

Figure 4.2: The relevant atomic levels of ^{21}Na and ^{23}Na for trapping. The $3S_{1/2}$ ground-state has two hyperfine sublevels, $F = 1$ and $F = 2$. The $3P_{3/2}$ excited level has four hyperfine sublevels, $F = 0, 1, 2, 3$. Note that the energy spacings are not drawn to scale.

containing stable ^{23}Na heated to about 100°C. The two beams stop on photodiodes, PD1 and PD2. One beam spatially overlaps a counterpropagating pump beam. The pump beam makes a double pass through AOM2 after the probe beams are split off. The AOM2 is modulated at about 1 KHz resulting in a frequency modulated probe beam. Subtracting PD1's signal from PD2's signal removes the Doppler feature of the saturated absorption spectrum. The subtracted signal is fed into a Stanford Research System SR5 lock-in amplifier to extract the magnitude of the signal oscillating at the modulation frequency. The resulting dispersive shaped error signal is fed into the laser's external lock, locking the laser's reference cavity to the atomic frequency.

Figure 4.2 shows the relevant D_2 atomic lines for ^{21}Na and ^{23}Na used in both the spectroscopy and the trapping. The spectroscopy probes transitions between the ground-state $3S_{1/2}$, F=2 level and the excited state $3P_{3/2}$, F'=1,2,3 levels. The frequency exciting these transitions will be notated $f_{F\to F'}$ where F and F' designate the hyperfine level of the $3S_{1/2}$ and $3P_{3/2}$ levels respectively. The best lock signal comes from the cross over feature halfway between $f_{2\to 2'}$ and $f_{2\to 3'}$. This feature is used to the lock the laser. Because of its double pass through AOM2 the frequency of the pump beam is $2f_2$ greater than the probe beams' frequency . The resulting output laser frequency, ν_l, when locking to the cross over

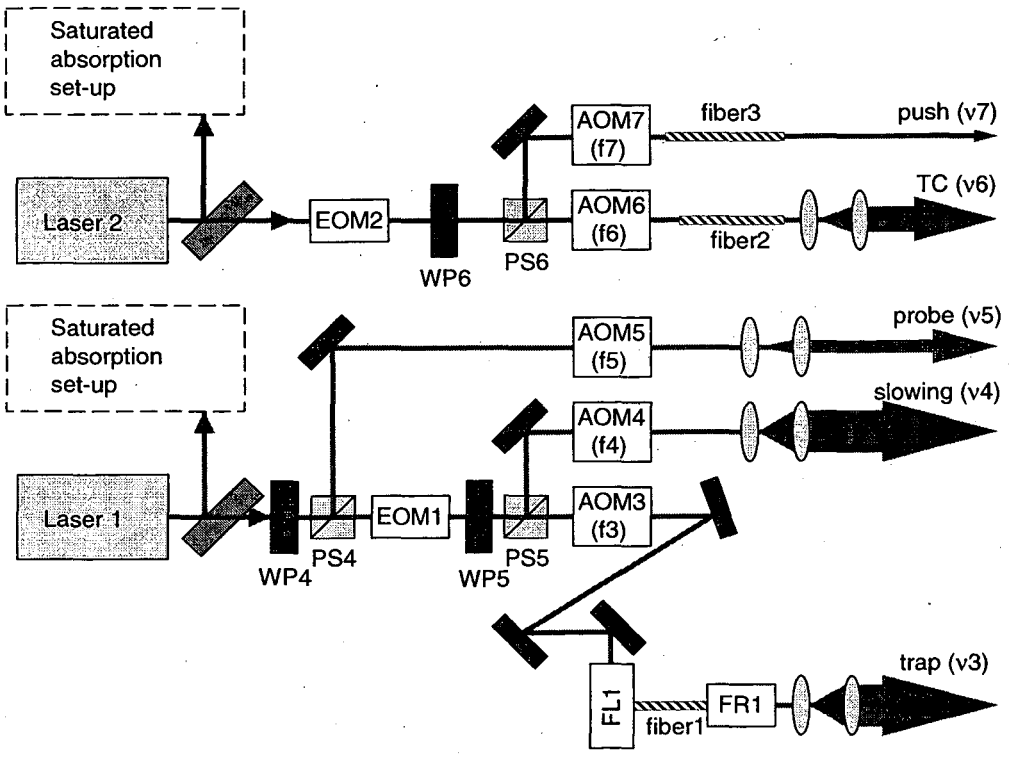

Figure 4.3: Overview of the optical system showing all of the beams used in the experiment.

feature, is

$$\nu_l = f_{2\to 3'} - 29.5 \text{ MHz} - \text{f}_2. \tag{4.1}$$

Figure 4.3 shows all of the beams used in the experiment. Most of the beams pass through an electro-optic modulator (EOM). The EOM adds sideband frequencies to these beams. Each sideband frequency contains about 15% of the total laser power. The EOM frequency is set such that when the main frequency makes a $F = 2 \to F' = 3^-$ transition the upper sideband frequency makes a $F = 1 \to F' = 2$ transition. With this additional frequency optical pumping into the $F = 1$ state is avoided. The EOM frequency is typically 1717 MHz for ^{23}Na and 1848 MHz for ^{21}Na. Next each of the beams passes once through an AOM. This serves two purposes. First, each beam can be tuned independently to a specific frequency. Second, each beam can be switched on and off remotely. When the drive

Laser Beam	Symbol	Frequency (MHz above $f_{2\to 3'}$)	Power or Intensity	Diameter FWHM (mm)
probe	ν_5	0	0.5 mW	6
push	ν_7	0 - +25	2-20 mW	6
slowing	ν_4	-30	15 mW/cm^2	10
transverse cooling	ν_6	-13	180 mW	5
trap-horizontal	ν_3	-13	20 mW/cm^2	9
trap-vertical	ν_3	-13	20 mW/cm^2	9

Table 4.1: Beam frequencies, sizes and powers in typical operation of the experiment.

frequency is removed from an AOM the beam is no longer deflected into the experiment and is effectively turned off. The frequencies of the various beams are

$$\nu_i = f_{2\to 3'} - 29.5 \text{ MHz} - f_2 + f_i, \tag{4.2}$$

where f_i is the frequency of the output AOM for the i^{th} beam. The AOM frequencies are adjusted for the required application. Table 4.1 lists the frequencies of each beam. The use of half wave plate and polarizing beam splitter in the set-up, for example WP4 and PS4, allow the laser power to be divided between the various output beams by rotating the wave plates. Table 4.1 shows the powers used in the experiment as well as the final beam sizes after being expanded by lens pairs.

A paragraph is included here relating to air bubbles in the dye jet in hope that others will avoid this trouble. The symptom, brief losses of frequency lock with the associated loss of trapped atoms was difficult to track down. The cause, air bubbles in the dye jet, was easy to correct once identified. The bubbles caused lasing to stop for short intervals, about 2μs. This interval was long enough for the laser to lose lock with its reference cavity. Then it took the laser's electronics 10 ms to regain the lock to the reference cavity. During this time the reference cavity's output indicated a swing in frequency of about 100 MHz, enough to eject the atoms from the trap. Air bubbles in the jet was the initial suspect but there was no evident cause or independent evidence that they existed. Finally it was determined that the replacement filters used in the dye circulator were defective. The solution was then simply to obtain a better dye filter. With a 0.5 μm filter in place there are no losses of frequency lock due to bubbles.

4.2 System Overview

Figure 4.4 gives an overview of the trapping apparatus. The figure is not drawn to scale; it is meant to illustrate how the different components of the experiment described in the following text fit together. Cave 3 is the location of the target and transverse cooling. The rest of the experiment is in cave 5 which is separated from cave 3 by a 1 m thick concrete radiation shielding wall.

4.3 The Vacuum System

The vacuum chamber holding the target oven is a modified 10.2 cm stainless steel cross welded to 15.2 cm conflat flanges. One flange connects to the 10.2 cm diameter beam pipe of the cyclotron which delivers the protons. One meter upstream, towards the cyclotron, the beam pipe is pumped with a CTI cryogenic pump. The oven is inserted into the cross and attached at the 15.2 cm flange. A Balzers 170 l/s turbo pump is located directly below the oven. The cross connects to a 15.2 cm vacuum cube where the transverse cooling is done. Four, 10.2 cm diameter windows on the cube allow the transverse cooling light to pass back and forth across the atomic beam. A Varian VacIon, 500 l/s ion pump for additional pumping is located under the cube. The cube is attached to the trapping vacuum chamber by a 2 m, 3.81 cm diameter tube which goes through the radiation shielding wall separating the target region in cave 3 from the trap region in cave 5. The impedance of this long tube makes differential pumping between the trap side and target side possible. The vacuum pressure in the transverse cooling cube during runs is a few times 10^{-8} torr while the trap side pressure is close to 10^{-10} torr. The trapping chamber is a modified 10.2 cm tube. Eight ports with 7.0 cm flanges on their ends are evenly spaced in the horizontal plane. The tube connecting the target side to the oven side is attached to one of these flanges. The others end with 3.81 cm clear view windows with a broadband antireflection coating. The slowing beam enters the chamber opposite the connecting tube. The two ports perpendicular to the slowing beam are used for trap measurements. The remaining four ports are used for the horizontal trapping beams. The bottom of the chamber has a 10.2 cm clear window and the top has a 3.81 cm clear window. Both have broadband antireflection coatings. The vertical trapping beams enter the chamber through these windows. A Varian VacIon, 500 l/s ion pump equipped with an internal titanium sublimation pump tees off

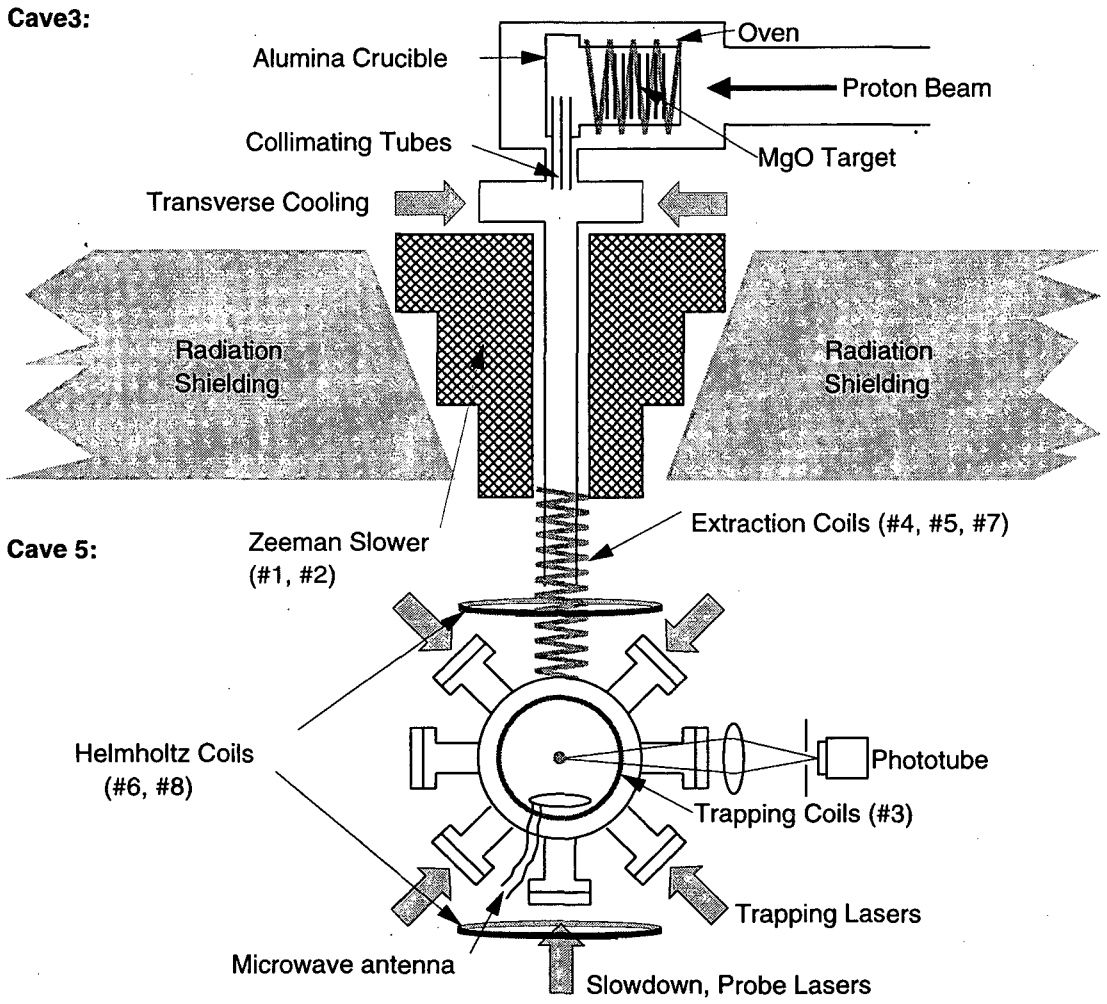

Figure 4.4: Overview of the trapping apparatus.

Field Number	Description	Resistance (Ω)	Inductance (mH)	Power Supply used	Current (Amps)
# 1	tapered Zeeman slower	68	660	Sorensen DCR 600-16T	3.83
# 2	constant Zeeman slower	58	360	EMI SCR	1.65
# 3	trapping quadrupole	1.8	2.2	Kepco BOP36-14M	6.0
# 4	1^{st} extraction (furthest from trap)	1.0	0.31	Kepco ATE55-10M	3.52
# 5	2^{nd} extraction	0.5	0.24	EMI 10-8	5.98
# 6	switched Helmholtz	1.8	8.8	Kepco BOP 50-2M	4.0
# 7	3^{rd} extraction (closest to trap)	0.3	.022	EMI 10-8	0.0
bike (# 8)	unswitched Helmholtz	25	23	Kepco SM 75-8 AM	0.47

Table 4.2: Listing of properties of the current coils and current settings for the "Lonely" Run.

the top of the chamber to pump the trapping region. One more 3.81 cm diameter viewport on the chamber at a 45° upward angle is used for viewing the trapped atoms.

4.4 Current supplies

Table 4.2 lists the current supplies used to supply the various coils used to create magnetic fields in the experiment. The current output for each coil during normal operation is listed. Figure 4.4 shows the location of each coil.

4.5 Phototube Calibration

A Hamamatsu HC120-08 phototube monitors the resonant light from the trap. It views the atoms through the horizontal port at 45° to the horizontal trapping beams. A 2.54 cm lens directly outside of the vacuum chamber, 15.2 cm from the trapped atoms, focuses light onto the detector. The phototube is run in two modes, current mode for strong signals and photon counting for weak signals. In current mode the phototube output is simply run

into a 10 kΩ resister and the voltage, V_{pt}, measured with a voltmeter. In photon counting mode the phototube signal is amplified and then discriminated and the resulting TTL pulses are counted. The rate of phototube counts is denoted R_{pt}. When the phototube is run at 615 V, 1.0 mV/10kΩ corresponds to 1.2×10^6 Hz.

The number of trapped atoms is estimated from the light scattered by the atoms from the trapping lasers. In the case of a two level atom the rate of spontaneous photon emission, R_{spont}, by near resonant light is

$$R_{spont} = \frac{\Gamma}{2} \frac{s}{1 + s + 4\frac{(2\pi\delta)^2}{\Gamma^2}}. \tag{4.3}$$

Γ is the atomic linewidth of the transition used, $2\pi \cdot 9.89$ MHz[55] for the sodium $3P_{3/2}$ line. The detuning of the exciting laser from the resonant frequency is δ. The saturation parameter is $s = I/I_{sat}$. I is the intensity of the exciting laser and I_{sat}=6mW/cm^2 for sodium. The intensities of the six trapping beams illuminating the atoms add up to 120mW/cm^2. Seventy percent of this intensity is in the main transition giving $s = 14$. Using the detuning of the trapping beams, -13 MHz, for δ in Equation 4.3 gives $R_{spont} = 2.0 \times 10^7$ photons/s-atom. The conversion from phototube reading to number of trapped atoms, N, is

$$N = \frac{R_{pt}}{e_q \Omega R_{spont}}. \tag{4.4}$$

Using a detector solid angle, Ω, of 1.7×10^{-3} and the quantum efficiency of the photocathode, e_q, of $12 \pm 1\%$ in Equation 4.4 gives $N = 300$ atoms/mV.

4.6 Transverse Cooling

The first place an optical force is used to manipulate Na atoms is the transverse cooling of the atomic beam. It reduces the transverse velocities, v_T, of the atoms in the atomic beam thereby increasing the forward flux of atoms which can be loaded into the trap. In general, a pair of counterpropagating laser beams, tuned below the resonant frequency, produces a damping force on the illuminated atoms. This "optical molasses"[61] slows the absolute velocity of the atoms in the region of the laser beams. The laser beam an atom is moving against is Doppler shifted closer to resonance while the laser beam copropagating with the atom is Doppler shifted further from resonance. A moving atom will preferentially absorb photons from the laser against which it is moving, resulting in a damping force,

$F \approx -\alpha v_T$. This equation slows atoms exponentially to $v = v_0 e^{-\frac{\alpha}{m}t}$. Reference[62] details the force which can be counterintuitive for high laser intensities where different laser polarizations and detunings give unexpected outcomes. Their two-level model gives a value for $\frac{\alpha}{m}$ for sodium with $I = 3I_{sat}$ and a detuning of -13 MHz equal to 3×10^4 1/s.

Red-detuned laser beams pass back and forth across the atomic beam to cool the atoms' transverse velocities with the damping force described above. The atoms leave the oven and travel through the pipe connecting the target and trap regions. The atoms with transverse velocities less than the critical velocity, v_T^{crit} (about 0.8 m/s), flow through the capture radius of the trap. The atoms with transverse velocities greater than v_T^{crit} are wasted. The transverse velocities, v_T^{cool}, that can be cooled to below the critical transverse velocity by transverse cooling satisfy

$$v_T^{cool} e^{-\frac{\alpha}{m}t} \leq v_T^{crit} \text{ or } v_T^{cool} \leq v_T^{crit} e^{\frac{\alpha}{m}t}. \tag{4.5}$$

The improvement factor, f_{TC}, due to transverse cooling is the ratio of atoms with transverse velocity cooled to less than v_T^{crit} to those with transverse velocity less than v_T^{crit} before cooling. In two dimensions it is the square of the ratio of the maximum value of v_T^{cool} to v_T^{crit}. Using Equation 4.5 gives

$$f_{TC} = \left(e^{\frac{\alpha t}{m}}\right)^2. \tag{4.6}$$

Using the time, $t = 4 \times 10^{-5}$ s, it takes to pass through 2 cm at 500 m/s in Equation 4.6 gives $f_{TC} = 11$.

The transverse cooling stage is located about 10 cm downstream from the beginning of the atomic beam at the crucible holes. Laser light from cave 5 goes to cave 3 through a polarization maintaining single mode optical fiber. About 100 mW of laser light, detuned 13 MHz below the $F = 2 \rightarrow F' = 3$ transition, emerges from the fiber and is collimated into a beam 5 mm in diameter. This beam is split in two. Each beam, one in the vertical and one in the horizontal planes, passes back and forth four times across the atomic beam such that each pass is spatially separated from the other passes. Then the laser beam is retroreflected so it retraces its path in the opposite direction. This optical configuration increases the number of trapped ^{23}Na atoms by a factor of 7-15 depending on the sensitive alignment. For ^{21}Na trapping, where the oven temperature is higher, up to a factor of ten increase in trapped atoms has been observed with transverse cooling.

4.7 Zeeman Slower

The sodium atoms emerge from the crucible with thermal velocities of about 1000 m/s. The atoms must be slowed down to the 10 m/s capture velocity of the trap to be loaded. The sodium atomic beam travels through the 2 m tube connecting the target and trapping regions. A counterpropagating laser beam slows the atoms with resonant laser light. An atom absorbs a photon and receives a velocity reduction of 3 cm/s. In the subsequent decay of the excited atom the spontaneous photon is emitted in all directions. After absorption of many photons the atom will on average be slowed 3 cm/s per photon. The deceleration possible with this mechanism is large. The spontaneous emission rate of a saturated atom is $\Gamma/2$. The resulting maximum deceleration for sodium is 9×10^5 m/s^2. With this deceleration an atom traveling at 1000 m/s is stopped in 0.5 m. But, if the atoms are initially in resonance with the laser light they will quickly fall out of resonance as they are slowed down due to their changing Doppler shift. For sodium the Doppler shift is 1.7 MHz per m/s. Given that the transition's linewidth is 10 MHz, once the atoms slow down by 6 m/s they are beginning to fall out of resonance. One method of maintaining the resonance condition as the atoms slow down is the Zeeman slowing technique[63][64]. With this method the effect of the Doppler shift on the slowed atoms is compensated for by an equal and opposite Zeeman shift. An atom can be slowed at nearly the maximum deceleration rate by designing a tapered magnetic field arranged so the atoms remain in resonance as they slow.

The Zeeman slower for the experiment is a 1.5 m long, freon cooled, tapered magnetic solenoid. The solenoid is embedded in the shielding wall dividing the target and trapping regions. It surrounds the 2 m long pipe connecting the two regions. The solenoid is wound in two coils. One coil, #1 in Table 4.2, is tapered and the other, #2 in Table 4.2, is constant. Each coil is designed to run with 4 A of current. With 4 A, coil #1 has a maximum field of 620 gauss and coil #2 has a constant field of 440 gauss. At the end of the Zeeman slower solenoid additional coils are wound to span the remaining 17 cm to the trap. These coils are referred to as the extraction coils and are listed as #4, #5, and #7 in Table 4.2. The currents is these coils are adjusted to smoothly connect the magnetic field of the Zeeman solenoid to the trapping magnetic field.

The slowing beam is aimed through the trap, down the tube connecting the target to the trap, and onto the crucible holes. The slowing beam is 1 cm in diameter with about

15 mW/cm^2 of laser intensity. It is detuned three linewidths below the $2 \rightarrow 3'$ transition to minimize trap disruption. The slowing beam is gradually focused so it is a 2 mm spot on the crucible holes. The beam is circularly polarized, σ^+, so the atoms are initially optically pumped to the $F = 2$, $m_F = 2$ level. The slowing proceeds on the $F = 2$, $m_F = 2$ $(m_J = 1/2, m_I = 3/2) \rightarrow F' = 3, m'_F = 3$ $(m'_J = 3/2, m_I = 3/2)$ transition with the other levels out of resonance at high field. A very small trap exists with no the slowdown beam. The slowdown beam is aligned by monitoring the trap brightness while steering the slowdown. Typically, the first alignment is done without the focusing lenses. Once the trap brightness is maximized the lenses are added and the trap brightness is again maximized, usually giving a factor of two increase in trap brightness.

4.8 The Magneto-Optical Trap

This experiment uses a robust neutral atom laser trap, the magneto-optic trap (MOT), which has become widely used in the atom trapping community. The MOT uses six laser beams from the $\pm\hat{\mathbf{x}}$, $\pm\hat{\mathbf{y}}$, and $\pm\hat{\mathbf{z}}$ directions with specific polarizations in combination with a quadrupole magnetic field configuration to produce a force toward the trap center. See Figure 4.5. In addition, due to the tuning of the trapping lasers below resonance, the atoms feel a damping force which cools them. As a result, cold atoms collect in the center of the trap. The temperature of the atoms in a MOT is about the Doppler limit temperature[65] which is 240μK for sodium. Many excellent descriptions of the MOT appear in the literature. For more details see, for example, [66].

The quadrupole magnetic field for the MOT is provided by two 100 turn 10-cm-diameter coils spaced 8 cm apart. The current flow is opposite in the two coils. With 6 A of current the field gradients at the trap center are 20 gauss/cm in the axial direction and 10 gauss/cm radial. The trap beam from the laser is divided into two beams. One is recycled among the four horizontal beams of the trap and the other makes the upward beam and a retroreflected downward beam. The mean intensity of each trapping beam is 20 mW/cm^2. The trapping beams are detuned about 13 MHz below the $F = 2 \rightarrow F' = 3$ transition. Each trapping beam is circularly polarized with the state shown in Figure 4.5. In Figure 4.5 the polarizations are defined in the direction of motion of the photon. The trapping apparatus is aligned and tested with ^{23}Na. The ^{23}Na comes from the dissociation of sodium oxide which was placed in the oven crucible. When the apparatus is correctly aligned a typical trap

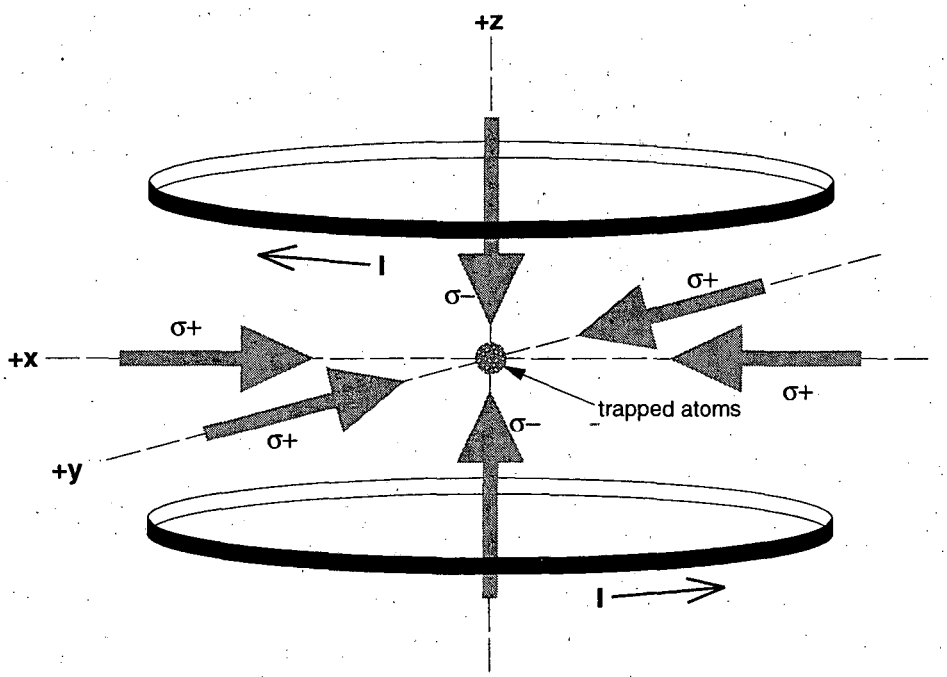

Figure 4.5: The electrical current geometry and laser beam polarizations for a magneto-optical trap.

Figure 4.6: Fluorescence light from trapped ^{21}Na atoms.

brightness is 700 mV/10kΩ at 500°C. This trap brightness was measured before the oven was heated to beam time temperatures at which time most of the sodium oxide evaporates.

Figure 4.6 shows a picture of the light scattered from the trapped atoms detected with a CCD camera. The small dot in the center is the collection of trapped ^{21}Na atoms. The light ring around the sides is the 3.81 cm vacuum port behind the atoms. The trap shown in Figure 4.6 was 75 mV or about 23,000 atoms. We took the picture during the "Lonely" Run which is the run that we made the the hyperfine splitting measurement. The most atoms trapped so far has been 90 mV/10kΩ or about 27,000 atoms.

The trapping efficiency can be estimated. The maximum possible number of atoms trapped, N_0 if all atoms that pass through the trap are trapped is

$$N_0 = \frac{\pi r_c^2 F_{trap}}{(\lambda_{trap} + \lambda_\beta)} f_{TC} \,. \tag{4.7}$$

The capture radius of the trap is r_c and F_{trap} is the ^{21}Na flux at the trap. The trap decay rate is λ_{trap} and f_{TC} is the trap brightness increase factor due to transverse cooling. The 27,000 atoms were trapped when 2 μA of protons were on target. Using a flag sticking probability

of 80% gives a ^{21}Na flux at the trap of $F_{trap} = 2.4 \times 10^4$ atoms/cm^{2}s (see Section 3.5). Using $2r_c$ =9 mm, λ_{trap}=0.14 Hz, and f_{TC} =10 in Equation 4.7 gives $N_0 = 1.1 \times 10^6$. The number of atoms trapped is about 2.7×10^4 so the trapping efficiency is only about 2%.

The slowing process is where many atoms are lost. The Zeeman slower can only slow atoms with velocities less than a maximum velocity. The Zeeman shift of the maximum magnetic field has a corresponding maximum Doppler shift. Atoms with higher velocities are never Zeeman tuned into resonance and are therefore not slowed. For sodium and the transition used, the maximum velocity, v_{max}, and the maximum magnetic field, B_{max}, of the tapered solenoid are related by

$$v_{max} = 0.83 \frac{\text{m/s}}{\text{gauss}} \times B_{max} \,. \tag{4.8}$$

The fraction, $F(v_{max})$, of thermal atoms at a temperature, T, with velocities less than v_{max} is

$$F(v_{max}) = \int_0^{v_{max}} 4\pi \left(\frac{m}{2\pi kT}\right)^{3/2} v^2 e^{-\frac{mv^2}{2kT}} \, dv \,. \tag{4.9}$$

Figure 4.7 plots $F(v_{max})$ for different temperatures. The Zeeman currents presently used, see Table 4.2, give a maximum field of 680 gauss or v_{max}= 560 m/s. Only 12% of atoms at 900°C are below 560 m/s and can be slowed. So the inefficiency of the Zeeman slower accounts for a large part of the low trapping efficiency.

The present number of trapped atoms is enough to measure properties of the atoms and this is now the focus of the experiment. It is still possible, though, to improve the number of trapped atoms further when necessary with more work. Some possible improvement ideas are briefly mentioned here. The slowing efficiency can be improved by reworking the Zeeman slower. The Zeeman solenoid has the potential to go up to 1100 gauss (v_{max}=900 m/s) which would allow 38% of the atoms to be slowed. To achieve this the extraction coils must be completely reworked in order to smoothly transfer the atoms from the higher field at the end of the solenoid. For an improvement of a factor of three this work may be worth it. As mentioned in Section 3.5 still longer collimating tubes should work to further increase the usable ^{21}Na flux. With two dye lasers there is enough laser power to increase the size of the trap beams as well. This will increase the capture radius of the trap to include most of the atomic beam. As the atoms are longitudinally slowed in the Zeeman slower a small amount of transverse heating results. The final diameter of the atomic beam at the trap as a result of this heating can be estimated. The number, N, of photons it

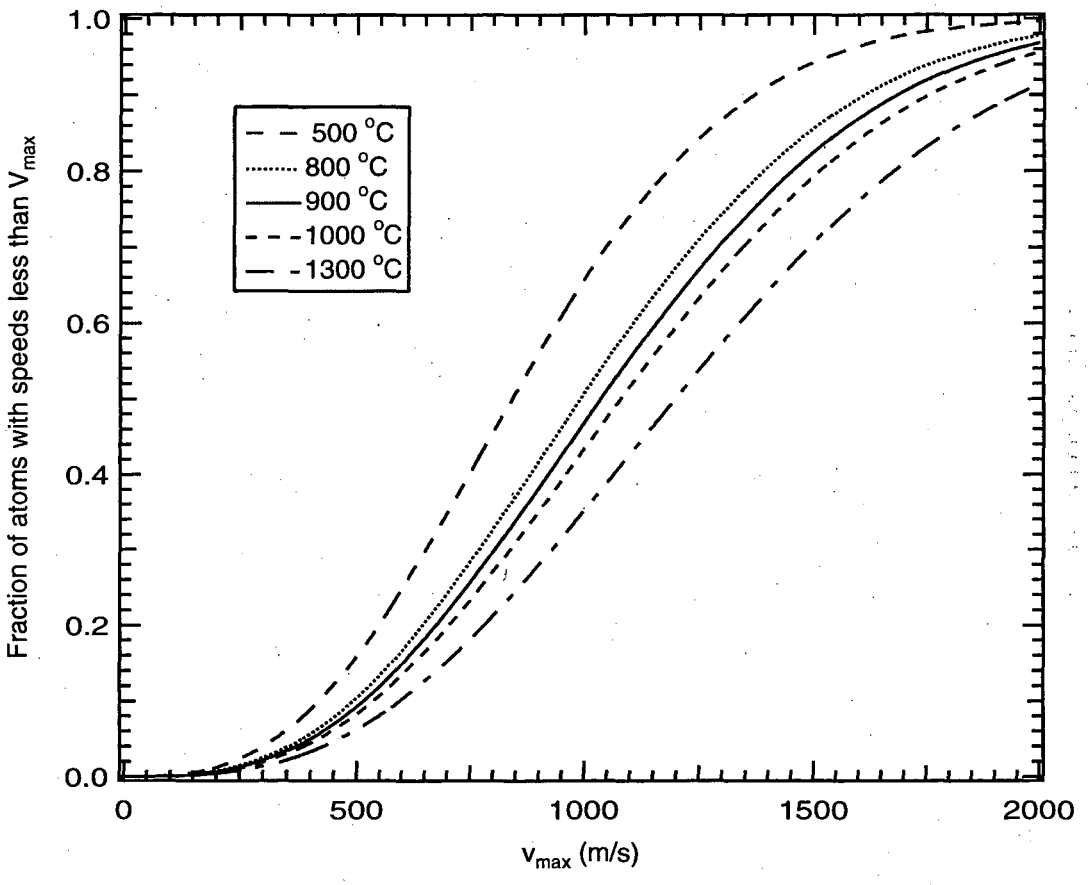

Figure 4.7: Graph of the fraction of atoms with speeds less than v_{max}.

takes to slow the atom down is $N = v/v_{photon}$ where v_{photon}=3 cm/s. The resulting heating of the transverse velocity, v_T, can be approximated by taking the transverse projection of a sphere of radius $\sqrt{N}v_{photon}$ which gives $v_T = \frac{\pi}{4}\sqrt{N}v_{photon} = \frac{\pi}{4}\sqrt{v \cdot v_{photon}}$. The resulting average beam diameter, d_{beam}, at the trap (z=160 cm after the transverse cooling) is

$$d_{beam} = \frac{z}{v/2} \cdot \frac{\pi}{4}\sqrt{v \cdot v_{photon}} = \frac{\pi z}{2}\sqrt{\frac{v_{photon}}{v}}. \tag{4.10}$$

The resulting atomic beam diameter at the trap is 1.8 cm for atoms with 560 m/s and 2.2 cm for atoms with 400 m/s. Increasing the size of the trapping beams to a 2 cm diameter will increase the capture diameter of the trap to better match the atomic beam size. Finally a better vacuum directly translates into more atoms by lowering the trap decay rate, λ_{trap}. Recently the trap's ion pump was cleaned, the titanium sublimation pump replaced, and the chamber baked resulting in an improved vacuum. This improvement should increase the number of trapped atoms in the next run. More vacuum measures may eventually be needed. Not only will the number of atoms increase but all of the atoms will beta decay in the trap. This is important for reducing the beta decay background and is discussed in Chapter 6.

Chapter 5

Measurement of the $3S_{1/2}$(F=1,m=0)$\rightarrow 3S_{1/2}$(F=2,m=0) Groundstate Transition in ^{21}Na with Trapped Atoms

A precise determination of the hyperfine splitting between the $(F = 1, m = 0)$ and the $(F = 2, m = 0)$ levels of the $3S_{1/2}$ ground state of ^{21}Na was made using the trapped atoms. This measurement, the first microwave transition observed in laser trapped radioactive atoms, took advantage of the long observation time and sensitive detection available with atoms nearly at rest in a trap to make a measurement on relatively few atoms. The atoms are released from the trap by turning off the trapping fields and lasers. In the dark the atoms are excited from the $3S_{1/2}(F = 1, m = 0)$ level to the $3S_{1/2}(F = 2, m = 0)$ level with a single microwave pulse at 1.9 GHz. Successful transition are measured by collecting the fluorescence of a probe beam tuned on the D_2 line, $F = 2$ to $F' = 3$. Previous work on stable Cs atoms in an optical molasses [67] provided the guide for this work. The size of the fluorescence signal is determined at a set of different microwave frequencies. At each frequency a cycle of optical manipulations prepares, illuminates and measures the atoms. Cycles at different frequencies are then combined to make a complete sweep of the frequency range desired to map out the Rabi resonance.

5.1 Computer Control

The experiment is run with a Power Macintosh 7100/80 computer running Labview 4 software. Data acquisition boards from National Instruments are placed in the computer's NuBus slots to allow exchange of information between the experiment and the computer. A GPIB board, the NB-GPIB/TNT, allows the desired microwave frequency and amplitude values to be sent to the microwave sythesizer. A counter/timing board, NB-TIO-10, provides accurately timed (within 1 μsec) TTL pulses to the experiment. The laser beams are turned on and off with these TTL pulses controlling Isomet acousto-optic (AOM) deflector drivers. The AOM's serve as light switches by deflecting the laser beams. The laser light can be switched on in $< 1\mu$s and off in 5μs. The sideband frequencies on the laser are turned on and off by switching the microwave power fed into the EOM. A Mini-Circuits ZYSWA-2-50DR, a dc to 5 GHz absorptive <5ns switch, which switches the EOM is controlled by a TTL pulse. Another Mini-Circuits ZYSWA-2-50DR is used to pulse the microwave feeding the antenna on for the time controlled by a TTL signal. A Mini-Circuits ZYSW-2-50DR, a dc to 5 GHz reflective <5ns switch, sends the output of the phototube monitoring the trap to either a discriminator for photon counting or to an integrator (τ=1 ms) for a trap size reading. Another TTL pulse controls the current to the extraction coils. Another TTL pulse gates the photon counting used during the atom probing stage of the experiment. A general input/output board, the NB-MIO-16XL, makes analog output pulses for programming the op-amp power supplies to output custom voltage pulses. An analog trigger pulse triggers the counter board to start the data cycle so all of the TTL pulses are synchronized with the current pulses. An ADC on the general board digitizes the trap size analog input. Finally all experimental parameters and values are written to disc. Figure 5.1 diagrams the data acquisition system.

5.2 Microwave Antenna

The microwave frequency 2 GHz is difficult to implement. The wavelength is 15 cm, roughly the dimension of the vacuum chamber. It is intermediate between the waveguide and simple loop antenna regimes. Microwave horn antennas at this wavelength have dimensions of 30 cm, too big for this application. Loop antennas radiate efficiently for loop dimensions much smaller than the wavelength but our geometry requires a fairly large

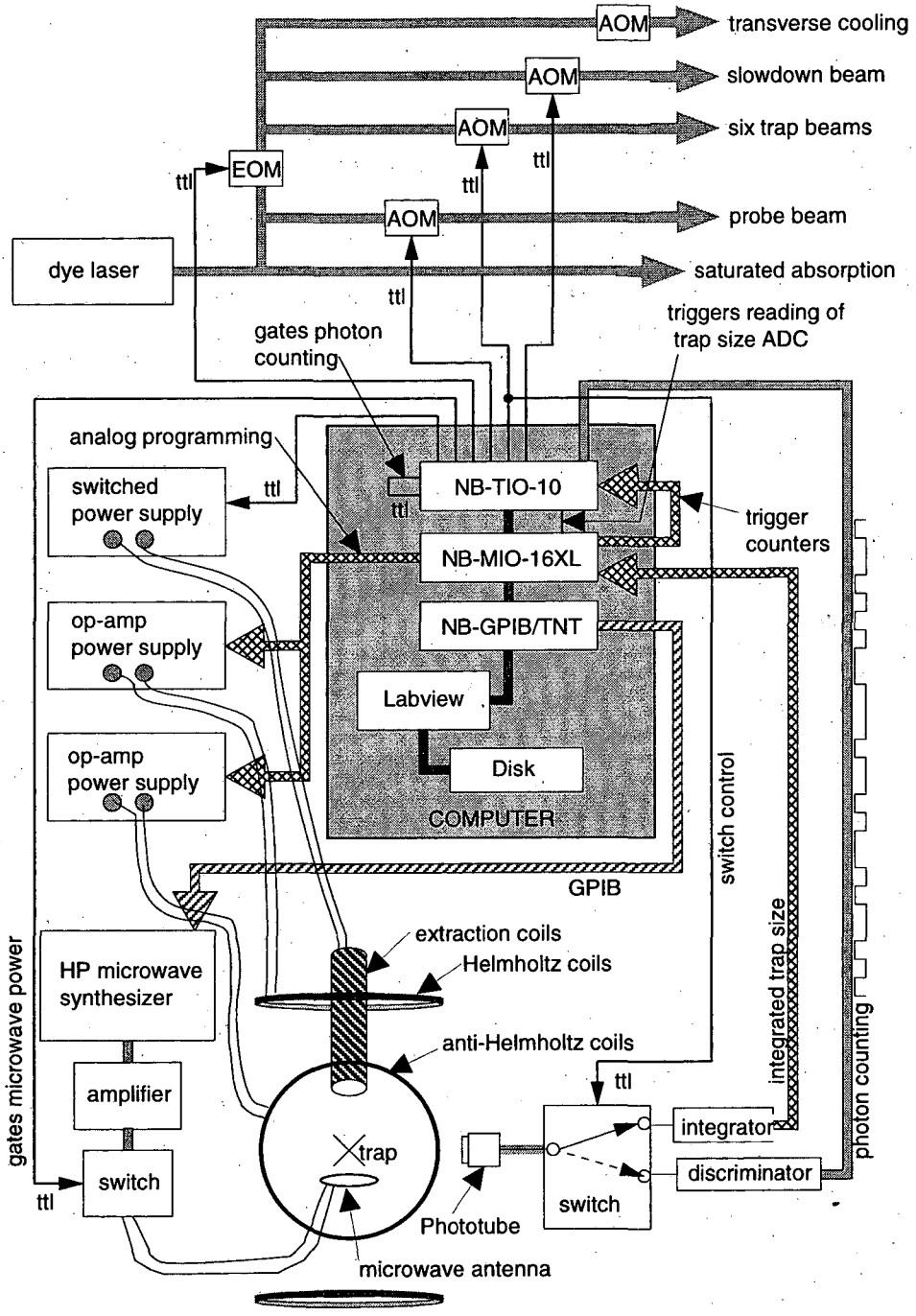

Figure 5.1: Computer control of the hyperfine measurement.

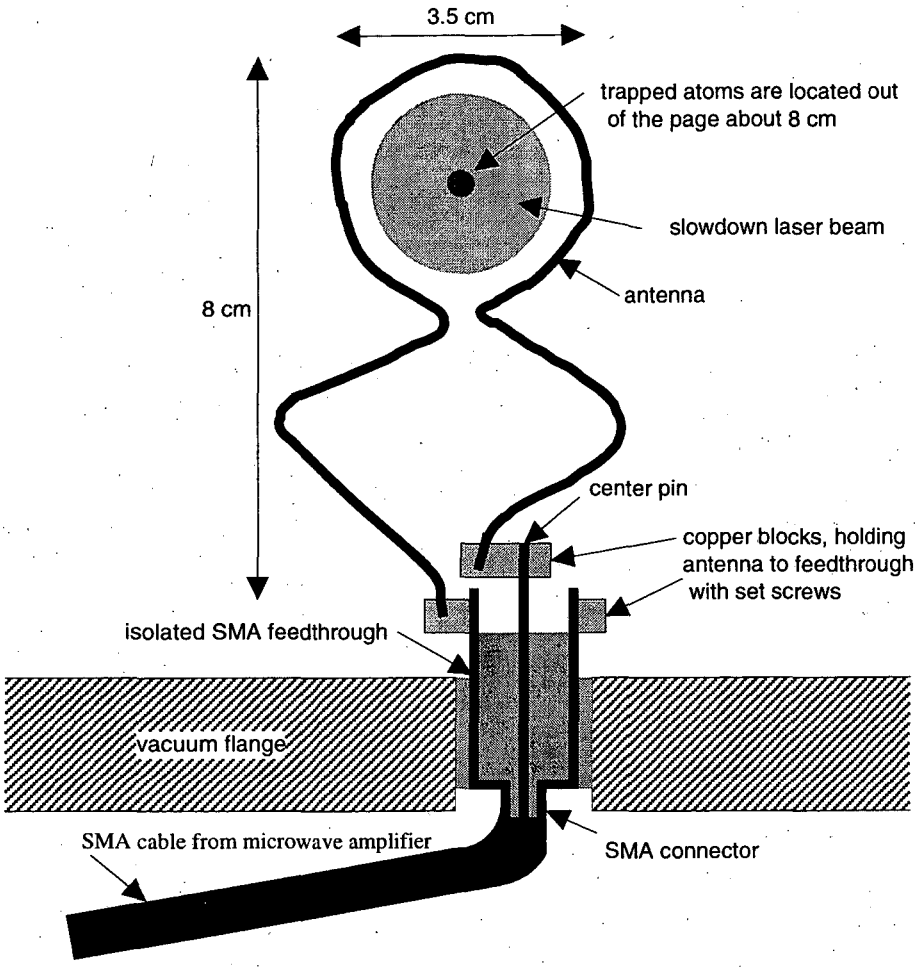

Figure 5.2: The microwave antenna used in the hyperfine measurement.

loop antenna size that fits around the laser beams. Luckly efficiency was not so much an issue. For a π resonance pulse lasting 1 ms, $4\mu\text{W/cm}^2$ of microwave power is needed. The microwave amplifier gives 500 mW of power. Also there is no shift in resonant frequency for $\Delta m_F = 0$ transitions due to amplitude modulation of the microwave field so the microwave radiation pattern is not crucial. This point is discussed further in Section 5.8. We require only moderate power to make the measurement.

Figure 5.2 shows the antenna. It is made from gauge 16 (diameter=1.3 mm) bare solid copper wire. The top part was carefully formed by hand in a 3.5 cm diameter circle. The leads were bent out then in, forming a figure eight shape, and connected to an isolated SMA vacuum feedthrough via small copper blocks and held with set screws. All parts were

acid dipped and ultrasonically cleaned. The antenna encircles the slowdown laser beam about 8 cm from the trapped atoms. The antenna was tuned for maximum radiation at the ^{21}Na and ^{23}Na hyperfine frequencies by squeezing the lower part of the antenna. A network analyzer measured the power reflected from the antenna for tuning. Power is supplied to the antenna by a Hewlett Packard 8660C synthesized signal generator, amplified with a Hewlett Packard 8349B microwave amplifier. When the hyperfine resonance was found the microwave power was adjusted to make a π pulse.

5.3 Current Switching

In order to measure the hyperfine splitting the trapping magnetic fields must be turned off and a homogeneous bias field turned on. It is desirable to do this as rapidly as possible because with the trap turned off the atom cloud expands ballistically. The measurement must be done before the cloud gets too large. In the process of making this measurement the effects of Eddy currents were found. Just because there is no current in the winding does not mean that no magnetic is present because currents induced in the stainless steel vacuum chamber persist. For the hyperfine measurement we could afford to wait for the Eddy currents to diminish. This effect will become problematic, however, for any rapidly switched beta decay experiment.

The effect of Eddy currents can be seen by monitoring the position of the hyperfine resonant frequency as a function of time after the field currents are shut off. The position of the resonant frequency depends quadratically on the size of the magnetic field during the microwave pulse (see Section 5.7). Figure 5.3 shows the resonances resulting from different time delays between the shut off of the current and the 1 ms microwave pulse. A Hall effect clamp-on amp meter was used to measure the decay of the current. The current is completely off in less than 1 ms, yet large magnetic field changes remain. The data from 1 ms are shifted far to the right, cooresponding to a field greater than 2 gauss. The data for a 2 ms delay have an odd shape, indicating that the magnetic field is still shifting during the microwave pulse. Its mean position indicates an average field of 1.3 gauss. The data from 3, 4 and 5 ms are finally stabilized and can be fit by Rabi resonance curves. The center frequency for these data correspond to a bias magnetic field of 0.9 gauss. This is evidence that Eddy currents persist in the vacuum chamber after the coil currents are zeroed. Even after 2 ms substantial changes in the magnetic field occur. Between 2 and 3 ms the size of

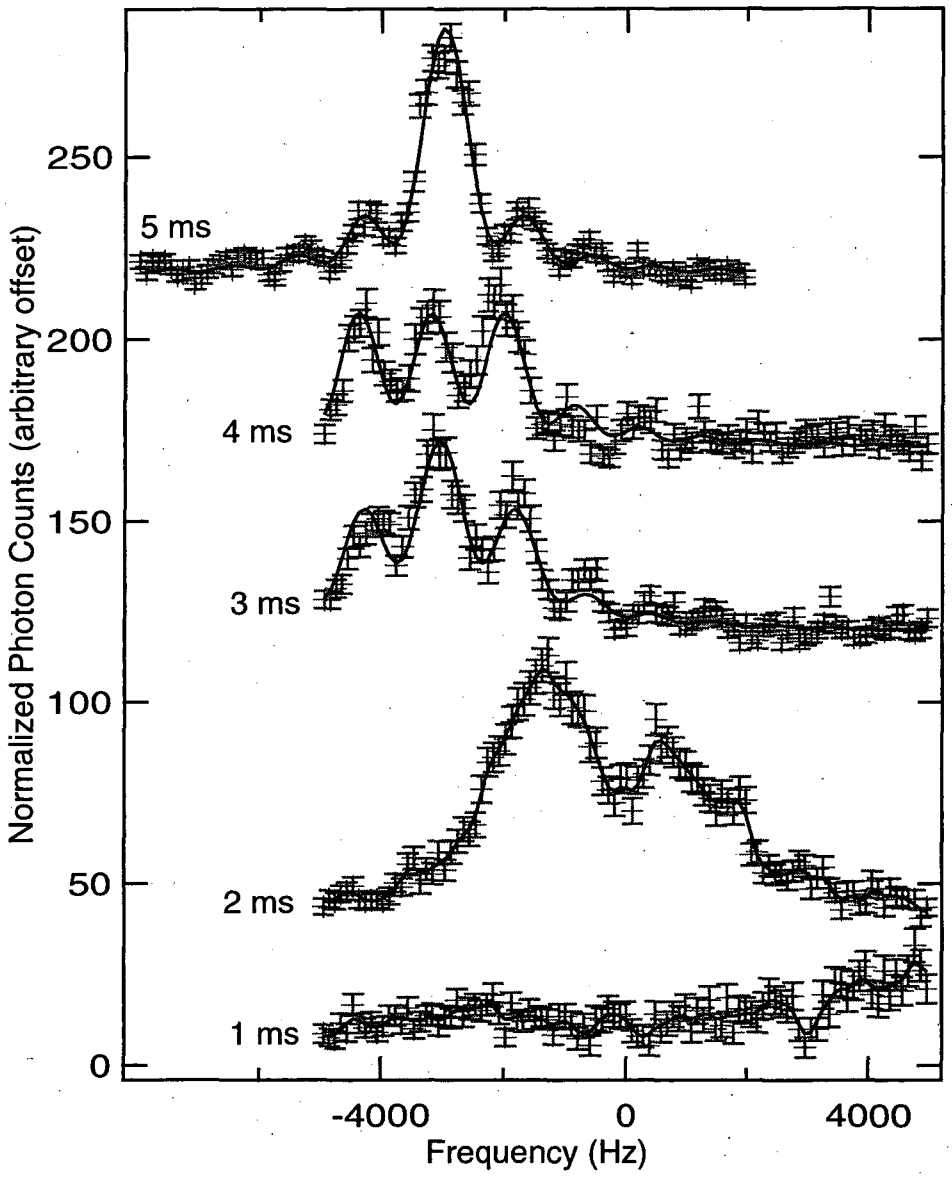

Figure 5.3: Graphs of hyperfine resonances with different microwave delay times. Data with different times, 1 ms-5 ms, between the current switching and microwave pulse are shown. Data for 1 ms and 2 ms have a smooth connecting curve. Data for 3, 4 and 5 ms are fit with a Rabi resonance curve. The microwave power for the 5 ms delay data is half that of the other scans.

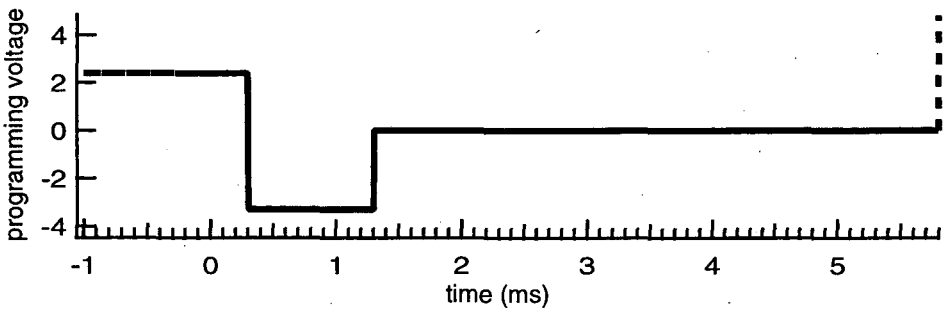

Figure 5.4: Programming voltages for switching the magnetic quadrupole trapping field.

the field changes by 0.4 gauss.

The quadrupole (#3) which makes the trapping field and the switched Helmholtz (#6) which makes the constant bias field must be switched at the last moment. See Figure 4.4 for the locations of the field coils referred to here. The other fields are shut off early with a small loss in trap collection efficiency. The critical magnetic fields (#3 and #6) are shut off as rapidly as possible by using shaped voltage pulses input to the bipolar operational amplifier power supplies. A Hall probe was used to monitor the magnetic field and the shaped voltage pulses were adjusted to minimize the decay time. Figure 5.4 shows the pulse for the quadrupole trapping field. The programming voltage overshoots the final value of zero in order to turn the fields off the fastest. Using this method the quadrupole and the switched Helmholtz fields were turned off in 2 ms. The noncritical extraction fields (#4 and # 5) were turned off with TTL controlled switches: The extraction fields are necessary for efficient collection of atoms but not for holding the atoms. So these fields were turned off 15 ms early. The TTL signal controls a power MOSFET which switches the currents on and off. The MOSFET used, a IRFP254, has a current rating of 22 amps and a breakdown voltage of 250 volts, giving plenty of headroom for switching $\approx$5 amps with inductive voltage kicks of $\approx$100 volts.

5.4 Data Cycle

The data cycle is repeated many times at different microwave frequencies to map the hyperfine resonance. The data cycle is a set of precisely timed optical manipulations. Table 5.1 shows the timeline of the data cycle. The cycle starts with about 30,000 trapped

time (ms)	event
-15	fields lowered
-3	trap size measured
0.00	shut off EOM
0.20	trap beams off
0.30	magnetic fields off
0.40	slowdown laser off
3.80-4.80	microwave pulse
4.80-5.05	probe atoms and count photons
after 5.05	trap back on
	recapture atoms and store data on disc
	collect more atoms
≈500	set new microwave frequency
	begin cycle again

Table 5.1: Data cycle for the hyperfine measurement.

atoms. Before the main cycle, the extraction coils (#4 and #5) are turned off in about ten milliseconds. At the same time the trapping quadrupole field (#3) is reduced to half of its normal value and the bias field (#6) is adjusted to maintain the trap's position. Then the phototube in current integration mode measures the optical fluorescence from the trap for trap size normalization. The main cycle begins now. Figure 5.5 shows how the atoms respond to the manipulations. The EOM is turned off to remove the repumping frequency and optically pump the atoms to $F = 1$. The six main trapping beams are then shut off. Then the quadrupole field (#3) and the bias field (#6) are rapidly turned off. The unswitched Helmholtz coils (#8) remain on. By adjusting the balance between the switched and unswitched Helmholtz fields the measurement can be performed at different magnetic field amplitudes. The fields are rapidly switched by using shaped voltage pulses as discussed before in Section 5.3. Next the slowdown laser is shut off. After a delay of 3.8 ms the atoms receive a 1 ms microwave pulse. After the microwave pulse, the atoms are probed to determine how many have been driven from $F = 1$ to $F' = 2$. The probe laser, aimed along the slowdown direction, is on for 0.25 ms. The probe laser intensity is 600 μW/cm^2. It is tuned to resonance for $F = 2$ to $F' = 3$. This cycling transition results in tens of photons produced for each atom now in $F = 2$. The photons are detected by the phototube and the individual pulses are discriminated and counted. Then the trap is

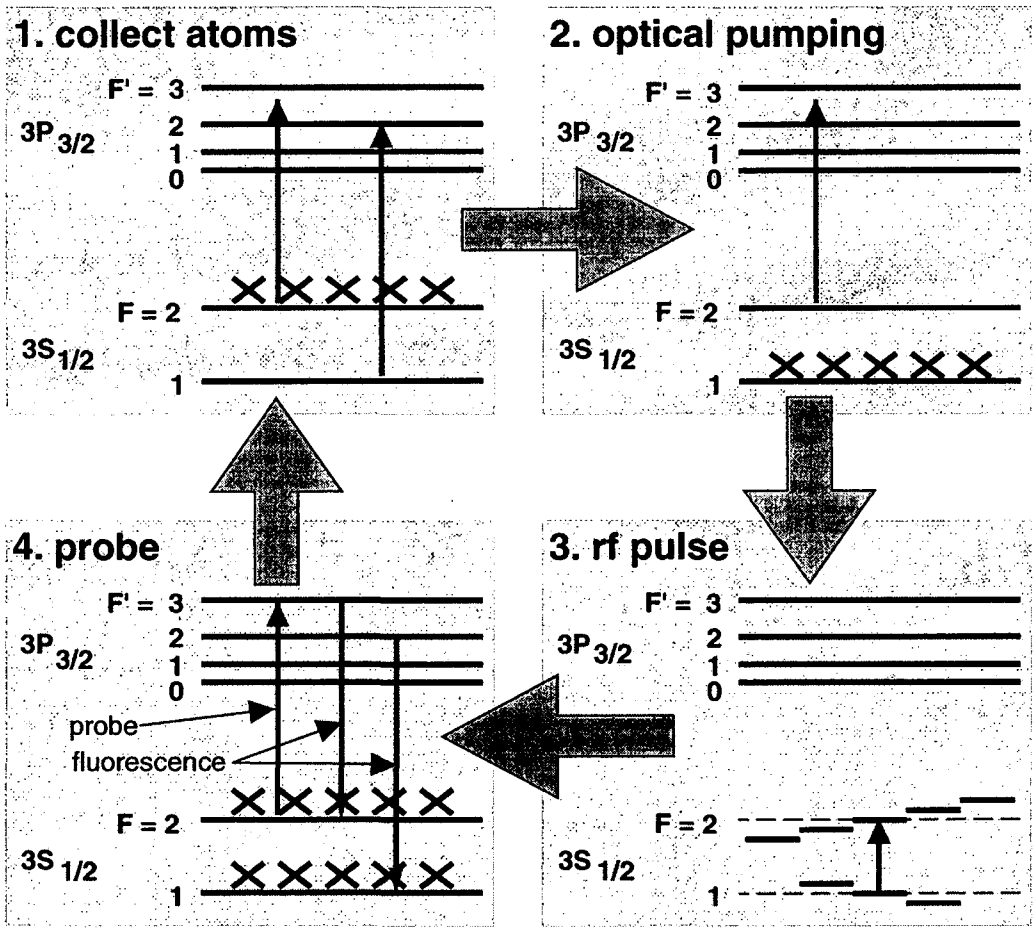

Figure 5.5: The manipulations of the atoms during the data cycle for the hyperfine measurement.

turned back on and the atoms are recaptured. The microwave frequency, trap size, and photon counts for the cycle are digitized and stored while more atoms are loaded into the trap for ≈0.5 seconds and a new cycle is begun.

5.5 Data Sets

Cycles are repeated until a complete sweep at the desired microwave frequencies has been made. This takes about 100 seconds. Initial inputs for scan width, typically 10 KHz, and number of steps, typically 201, define a data set at discrete frequencies. When we performed the experiment with a sequential scan of microwave frequencies we obtained distinctly asymmetric lineshapes for the hyperfine resonance. By investigating the trap size data we verified that the effect was caused by trap losses during the measurement cycle. When the microwave frequency is at resonance, atoms transferred to the $F = 2$ state by the microwave pulse are ejected out of the recapture region by the probe beam. This produces a diminished signal size for subsequent frequencies in the scan. We addressed this problem with randomly selected microwave frequencies. This procedure averages the trap size fluctuations across the entire lineshape. Differences in trap population at each microwave frequency are directly corrected for by normalizing the fluorescence pulse by the trap size brightness measurement taken before each point.

A data set is made up of many sweeps, usually five to ten, taken at a fixed bias field. At the end of each data set five cycles of background data where no atoms were trapped (trapping quadrupole (#3) remained off) were taken. This allowed us to identify the photon count background and the trap size background caused by laser light reflected off the vacuum chamber. After adequate data were taken at a given bias field setting a new one was set. First the current in the unswitched Helmholtz (#8) coils was changed. Then the dc level of the switched Helmholtz (#6) was changed so the trap remained in the same place. Then by watching the trap size signal on an oscilloscope as the power supplies were switched the intermediate value of coils #6 was adjusted so that the trap remained still when the current in the quadrupole field (#3) coils was halved.

Data sets were taken with six distinct magnetic bias field configurations. For each different bias field, data were taken for both ^{21}Na and ^{23}Na. The ^{23}Na data allowed us to calibrate the bias field strength by comparing to the known zero field splitting of ^{23}Na. Then given the bias field strength the zero field splitting for ^{21}Na was found from the data.

5.6 Magnetic Dipole Transitions

This experiment measures the energy separation between hyperfine levels by exciting transitions between them with resonant microwaves. The magnetic field, $\vec{B}_{rf}$, of the microwave interacts with the magnetic moment giving

$$H_{int} = g_J \mu_B \vec{J} \cdot \vec{B}_{rf} + g_I \frac{m}{M} \mu_B \vec{I} \cdot \vec{B}_{rf}. \tag{5.1}$$

This Hamiltonian provides an oscillatory perturbation that drives transitions between the two states. The second term in equation 5.1 is much smaller than the first, down by the ratio of electron to proton masses, and can be dropped.

The probability of a transition from state 1 to state 2 after the application of a constant amplitude oscillatory perturbation at angular frequency ω for a time t is given by the well known formula [68],

$$P_{1\to 2} = \frac{\Gamma^2}{(\omega - \omega_{HFS})^2 + \Gamma^2} \sin^2\left(\sqrt{(\omega - \omega_{HFS})^2 + \Gamma^2}\,\frac{t}{2}\right). \tag{5.2}$$

The resonant angular frequency ω_{HFS} results from the energy splitting, $\hbar\omega_{HFS}$, between the two levels. The strength of the transition,

$$V_{1,2} = \int \psi_2^* H_{int} \psi_1 d^3\vec{r} = \frac{1}{2}\hbar\Gamma e^{i\omega t} \tag{5.3}$$

defines Γ. Using H_{int} from Equation 5.1 and separating out the time dependence of $\vec{B}_{rf}$ using $\vec{B}_{rf} = \vec{B}^{rf}(r)e^{i\omega t}$ gives

$$\begin{aligned} V_{1,2} &= g_J \mu_B e^{i\omega t} < F = 1, m_F = 0 | \vec{J} \cdot \vec{B}^{rf}(r) | F = 2, m_F = 0 > & (5.4)\\ &= g_J \mu_B e^{i\omega t} < 1, 0 | J_- B_+^{rf}(r) + J_z B_z^{rf}(r) + J_+ B_-^{rf}(r) | 2, 0 > & (5.5) \end{aligned}$$

where

$$\begin{aligned} B_+(r) &= \frac{1}{\sqrt{2}}[B_x^{rf}(r) + iB_y^{rf}(r)] & (5.6)\\ B_-(r) &= \frac{1}{\sqrt{2}}[B_x^{rf}(r) - iB_y^{rf}(r)] & (5.7) \end{aligned}$$

The three J operators are spherical tensors of rank 1. By applying the Wigner-Eckart theorem it is seen that only the J_z term contributes to the $\Delta m_F = 0$ transition. The m_F states are defined by the direction of a static magnetic field, $\vec{B}_{dc}$. So only the component of the oscillating field, $\vec{B}_{rf}$ parallel to $\vec{B}_{dc}$ contributes. On the other hand, transitions with $\Delta m = \pm 1$ are controlled by the components of $\vec{B}_{rf}$ perpendicular to $\vec{B}_{dc}$. This distinction

is important in the discussion of systematic shifts and broadenings of the resonance in Section 5.8. Calculating the action of J_z on the state $|F = 2, m_F = 0 >$ gives

$$V_{1,2} = \frac{1}{2} g_J \mu_B B_z^{rf}(r) e^{i\omega t} \tag{5.8}$$

so

$$\Gamma = \frac{g_J \mu_B B_z^{rf}(r)}{\hbar}. \tag{5.9}$$

Equation 5.2 on resonance ($\omega = \omega_{HFS}$) reaches its first maximum value when $\Gamma t = \pi$. A pulse satisfying this condition is called π pulse. The microwave power needed to make a π pulse is calculated here. The amplitude of B_z^{rf} is related to $\overline{S}$, the mean power flux of the microwave, by

$$B_{rf} = \sqrt{\frac{2\mu_0}{c}\overline{S}}\,. \tag{5.10}$$

Combining Equation 5.9 with $\Gamma = \frac{\pi}{t}$ gives

$$\overline{S}_\pi = \frac{\hbar^2 \pi^2 c}{2\mu_0 t^2 g_J \mu_B}. \tag{5.11}$$

For a 1 ms pulse the microwave power needed for a π pulse is $4\mu W/cm^2$ if all the microwave magnetic field is in the $\hat{z}$ direction.

5.7 Shifts in Levels in an External Magnetic Field

Magnetic sublevels of a state shift in energy when an external magnetic field is applied. For small fields the $m_F \neq 0$ states shift linearly with the applied field,

$$\Delta E_{F,m_F} = g_F \mu_B B_{dc} m_F \tag{5.12}$$

$$= \pm\frac{1}{2}\mu_B B_{dc} m_F = \pm 0.700 m_F \text{ MHz/gauss } (S_{1/2}, F = {}^2_1). \tag{5.13}$$

The $m_F = 0$ states shift only a small amount in comparison, moving quadratically with the applied field. In this experiment a small external magnetic field is applied which separates the magnetic sublevels allowing the transition of interest to be probed independently and cleanly. The relatively field insensitive $m = 0 \rightarrow m = 0$ transition is separated from the other transitions which broaden much more due to field nonuniformities. For the ground state of sodium the $m = 0$ level shifts are described by the Breit-Rabi formula, see for

	g_J	g_I	$\nu_0 = \omega/2\pi$
^{21}Na	2.002319...[70]	2.3861(1)[32]	1906.47(2) MHz[32]
^{23}Na	2.002319...[70]	2.2176[71]	1771.6261288 MHz[71]

Table 5.2: Landé g-factors for the $3S_{1/2}$ atomic level (equal to the electron spin g-factor), nuclear g-factors, and zero field groundstate hyperfine splittings for ^{21}Na and ^{23}Na.

instance [69]. In a constant magnetic field B_{dc},

$$\Delta E_{F=\frac{2}{1},m_F=0} = \pm\frac{\hbar\omega_0}{2}\left[\left(1+x^2\right)^{\frac{1}{2}}-1\right] \tag{5.14}$$

where

$$x = \frac{\left(g_J + g_I\frac{m}{M}\right)\mu_B B_{dc}}{\hbar\omega_0} \tag{5.15}$$

so the difference frequency, ν_{HFS}, between the two $m = 0$ levels is

$$\nu_{HFS} = \nu_0 + \Delta\nu_{HFS} \tag{5.16}$$

with

$$\begin{aligned}\Delta\nu_{HFS} &= \frac{\omega_0}{2\pi}\left[\left(1+x^2\right)^{\frac{1}{2}}-1\right] = \frac{\omega_0}{2\pi}\left[\frac{1}{2}x^2 - \frac{1}{8}x^4 + ...\right] \\ \Delta\nu_{HFS} &= \frac{\left(g_J + g_I\frac{m}{M}\right)\mu_B^2}{4\pi\hbar^2\omega_0}B_{dc}^2. \end{aligned} \tag{5.17}$$

These shifts, although small, must be accounted for in order to extract the zero field splitting, ν_0, from the data. For a field of 2 gauss, the highest used in the experiment, x is 4×10^{-3}. The $-\frac{1}{8}x^4$ term in Equation 5.17 then equals 0.1 Hz so it and higher order terms can be dropped for our level of accuracy. The numerical values of Equation 5.17 are found using the values in Table 5.2,

$$\begin{aligned}\Delta\nu_{HFS} &= 2.219\times10^3 B_{dc}^2\,(\text{Hz/gauss}^2) \text{ for } ^{23}\text{Na} \\ &= 2.062\times10^3 B_{dc}^2\,(\text{Hz/gauss}^2) \text{ for } ^{21}\text{Na}. \end{aligned} \tag{5.18}$$

The magnetic field strength is calibrated by making a measurement of the shift in the resonance of ^{23}Na in the same field. Because the zero field splitting is known for ^{23}Na, B_{dc} can be calculated using Equation 5.18. The shift in the resonance of ^{21}Na can then be calculated. By writing Equation 5.17 for the two isotopes with B_{dc} the same for both

measurements the shift in the resonance for ^{23}Na, $\Delta\nu_{23}$, is directly related to the shift in the resonance of ^{21}Na, $\Delta\nu_{21}$, by

$$\frac{\Delta\nu_{21}}{\Delta\nu_{23}} = \frac{(g_J + {}^{21}g_I \frac{m}{M})^2}{(g_J + {}^{23}g_I \frac{m}{M})^2} \cdot \frac{{}^{23}\nu_0}{{}^{21}\nu_0} = 0.92937(3). \tag{5.19}$$

Here the notations $^{21}\nu_0$ and $^{23}\nu_0$ are the zero field resonant frequencies for ^{21}Na and ^{23}Na respectively. The nuclear g-factors for ^{21}Na and ^{23}Na are notated $^{21}g_I$ and $^{23}g_I$.

The procedure is to measure the resonant frequency in a finite field, calculate the shift with Equation 5.19 and then determine the zero field splitting, $^{21}\nu_0$. But Equation 5.19 depends on $^{21}\nu_0$ and g_I, so how can this work? A highly accurate calculation of shifts needs only minimal accuracy in the isotope's parameters. The numerical value in Equation 5.19 is calculated from the rough parameters determined in [32] where the splitting is found to only 20 KHz. This accuracy, though, is enough to calculate the shifts to 0.5 Hz. in a 2 gauss field. Even if no values are known for an isotope this procedure can be followed. Just find the resonance in a 1 gauss field where the shift is $\approx$2 KHz and the splitting will be known without any correction well enough to be used in Equation 5.19. Meanwhile, the value of g_I is only needed to a few percent. The Fermi-Segré formula relates the nuclear g-factors of two isotopes of the same element to their hyperfine splittings and nuclear spins. In the case of ^{21}Na and ^{23}Na the relation is

$$\frac{{}^{21}g_I}{{}^{23}g_I} = \frac{{}^{21}\nu_0\,{}^{21}I}{{}^{21}I + \frac{1}{2}} \cdot \frac{{}^{23}I + \frac{1}{2}}{{}^{23}\nu_0\,{}^{23}I} = \frac{{}^{21}\nu_0}{{}^{23}\nu_0}. \tag{5.20}$$

The nuclear spins of ^{21}Na and ^{23}Na, ^{21}I and ^{23}I, are both 3/2. The Fermi-Segré formula is good to about 1 part in 10^3 for light isotopes and easily provides the accuracy needed as input for Equation 5.19. The value of $^{21}g_I$ given in Table 5.2 was not measured directly but derived from the Fermi-Segré formula combined with theoretical estimates of the small corrections due to charge and magnetization effects [32].

5.8 Lineshapes

Equation 5.2 gives the probability that an atom will make a transition as a result of exposure to a microwave pulse of angular frequency ω. For a group of atoms this probability represents the fraction of them that transfer to state 2. This model represents the ideal situation where all the atoms receive the same perturbation which has a constant amplitude.

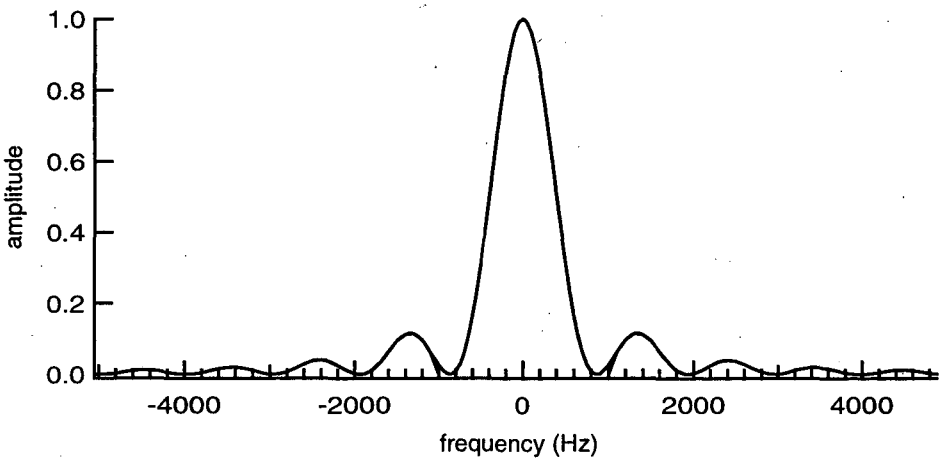

Figure 5.6: The resonance shape for a π pulse.

Also the bias field, B_{dc}, is constant over the extent of the atoms so the resonant frequency, ν_{HFS} is the same for all. In reality the atoms are in a finite expanding cloud during the microwave pulse. The microwave radiation pattern is not constant over the cloud of atoms. For an atom, moving outward during the microwave pulse, the direction of $\vec{B}_{rf}$ relative to $\vec{B}_{dc}$ and the amplitude of the perturbation changes. Inhomogeneities in B_{dc} give each atom a slightly different ν_{HFS}. This section discusses the effects of these imperfections. Broadening of the resonant shape still allows the center frequency to be extracted. The main worries are systematic shifts in the peak frequency.

Figure 5.6 shows the value of $P_{1\to 2}$ for a π microwave pulse with t=1 ms. The width of a π pulse, W_π, is determined by the duration, Δt, of the microwave pulse. It is

$$W_\pi = \frac{.80}{\Delta t} \text{ (Hz)}. \tag{5.21}$$

So a shorter pulse gives a broader resonance. One broadening mechanism comes from changes in the amplitude of the perturbation during the pulse. This can be understood in terms of a shorter effective pulse duration. An example of this broadening resulting from a triangular pulse is shown later.

Due to the finite extent of the atom cloud, different atoms see slightly different bias fields. Then each atom has a slightly different resonant frequency, ν_{HFS}. The broadening of the resonance due to this effect is

$$W_B = 4 \times 10^3 B\, \Delta B \text{ (Hz/gauss}^2\text{)}. \tag{5.22}$$

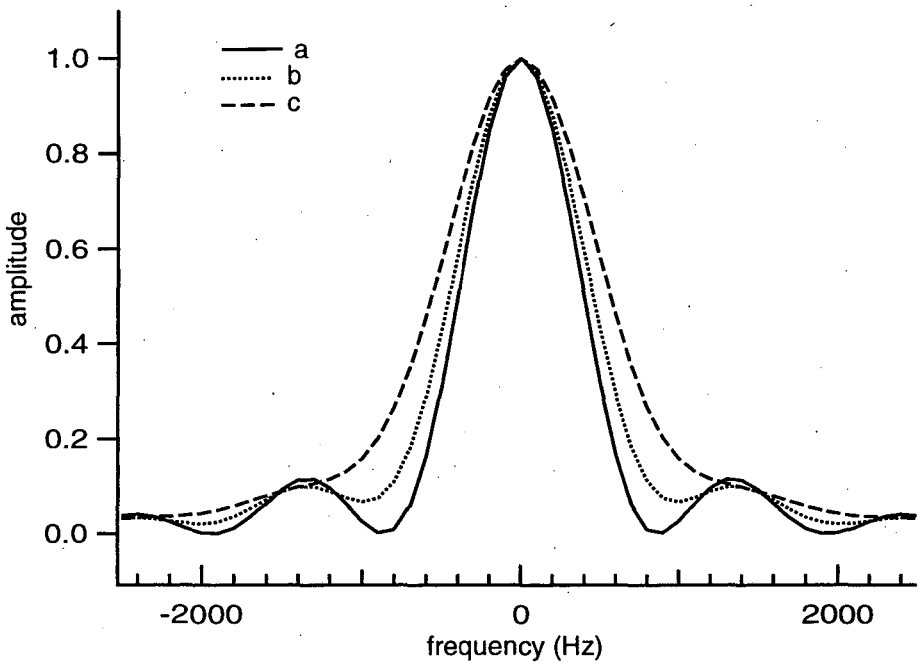

Figure 5.7: Resonant shapes resulting from a basic π resonance convoluted with gaussians. Descriptions are in the text.

Here B is the average bias field and ΔB is the spread in bias field values for the different atoms. If the distribution of resonant frequencies over the atoms is represented by $D(\nu_{HFS})$ then the final resonant shape, $S(\nu)$, is the convolution of D with the basic shape,

$$S(\nu) = \int d\nu_{HFS} P_{1\to 2}(\nu - \nu_{HFS}) D(\nu_{HFS}). \tag{5.23}$$

Since the measurements for ^{21}Na and ^{23}Na are made with the same distribution, $D(\nu_{HFS})$, the shapes are the same. So the shifts from the 0-field resonant frequency described by Equation 5.18 are actually shifts from the mean resonant frequency, $\overline{\nu}_{HFS}$. Note that $D(\nu_{HFS})$ can have an asymmetric shape and this procedure, being linear, still works. The final data set was symmetric though. Figure 5.7 shows the shape of the resonance curve when $D(\nu_{HFS})$ is a gaussian. Shape a is the standard π pulse with $t = 1$ ms. Shape b is shape a convoluted with a gaussian of width 500 Hz. Shape c is shape a convoluted with a gaussian of width 800 Hz.

The effects mentioned so far broaden the resonance. This is not a serious problem when determining the hyperfine splitting by comparing to a known isotope. If there is a systematic shift from the center frequency as defined by the mean magnetic field then

the extracted value of ν_0 will have an error. With 2 GHz so difficult to broadcast the inhomogeneity of the microwave pattern is a concern. A Doppler shift can occur if the microwave does not form a standing wave but dissipates as it travels outward. The $e^{i\omega t}$ in the perturbation is replaced by $e^{i(\omega t - kr)}$. For sodium at the typical trap temperature of 300 μK an atom's average velocity is 0.5 m/s. If all the atoms traveled the same direction the Doppler shift would be

$$\Delta\nu_{Doppler} = \frac{kv}{2\pi} = 3 \text{ Hz}. \tag{5.24}$$

This effect is already small and is further reduced in the final error on $^{21}\nu_0$ to $(1 - .929) \times 3$ Hz $= 0.2$ Hz as a result of the isotope comparison. The shifts due to using the rotating wave approximation are also negligible. The microwave field is $\vec{B}_{rf} = \vec{B}^{rf}(r)\cos\omega t = \vec{B}^{rf}(r)[e^{i\omega t} + e^{-i\omega t}]$. Writing the field $\vec{B}_{rf}$ as $\vec{B}^{rf}(r)e^{i\omega t}$ uses the rotating wave approximation. The effect of neglecting the $e^{-i\omega t}$ component is minimal in this case [68] with

$$\Delta\nu_{RWA} = \frac{\Gamma^2}{2\omega_0} = \frac{\pi^2}{2\omega_0 t^2} = 0.002 \text{ Hz (for a } \pi \text{ pulse)}. \tag{5.25}$$

Amplitude changes and changes of the angle between $\vec{B}_{rf}$ and $\vec{B}_{dc}$ are possible in this experiment. In some cases effects like these, notably the Millman effect [72], cause large shifts. Millman shifts occur in atomic beam experiments when as a result of the loop antenna used the microwave field direction rotates 180° as the beam passes through the excitation region. In the trapped atoms case the atoms may see some rotation of the microwave field as they fly outward during the microwave pulse. Luckily, for $m = 0 \rightarrow m = 0$ transitions no shifts can occur [73][74]. This is true because for the interaction, $e^{i\omega t}A(t)$ where $A(t)$ is real, the evolution equation is symmetric around the original resonant frequency. Referring to Equation 5.5, $\Delta m = 0$ transitions have an interaction $V_{1,2} = g_J\mu_b e^{i\omega t}B_z^{rf}(r,t) < J_z >$ where B_z^{rf} is real. Even if $B_z^{rf}(r,t) = C\cos\omega' t$ the shape remains symmetric about ω_0 (for large ω' the resonance separates into two resonances centered at ω_0). This remains true as long as the RWA is valid, $\omega' << \omega_0$. The $\Delta m = \pm 1$ transitions on the other hand can have large Millman shifts. This fact is illustrated by the following simple example: If $B_x^{rf}(r,t) = B\cos\omega' t$ and $B_y^{rf}(r,t) = B\sin\omega' t$ then

$$V_{1,2}(\Delta m = 1) = g_J\mu_b e^{i\omega t}[B_x^{rf}(r,t) + iB_y^{rf}(r,t)] < J_+ > = g_J\mu_b e^{i(\omega+\omega')t}B < J_+ > . \tag{5.26}$$

The result is that the resonance shifts by ω'.

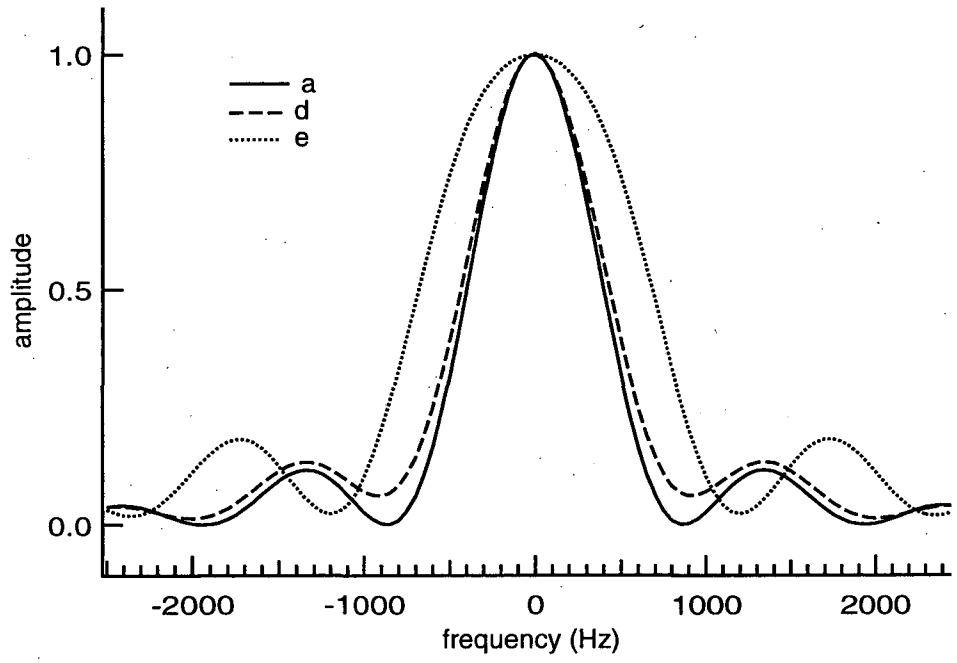

Figure 5.8: Resonant shapes resulting from time dependent interactions. See the text for details.

Time dependence of the interaction does not shift the resonant frequency but it does broaden the peak. Figure 5.8 shows some examples. The basic evolution equation was progressed in small steps to calculate these shapes. Both have the same average value of Γ as a π pulse. Shape d has the triangle time dependence,

$$\Gamma(t) = \frac{\pi}{3t}(2 - 1000t). \tag{5.27}$$

This models the possible amplitude dependence of an atom moving away from the antenna. Shape e is an extreme example where an additional amplitude oscillation of 300 Hz is added. The time dependence used is

$$\Gamma(t) = \frac{1.12\pi}{t}\cos(600\pi t). \tag{5.28}$$

Here the shape is broadened by about 600 Hz but centered.

5.9 Sorting and Fitting

The raw data were sorted by frequency and trap size. At the time of the experiment, the laser was suffering from brief losses of frequency lock for about 10 ms due to air

bubbles in the dye jet. These frequency excursions were usually to the blue of F = 2 → 3 and ejected the atoms from the trap. Therefore it was necessary to cut these episodes from the data. Only photon count data whose trap size is greater than a certain fixed cut-off are retained and binned by frequency. A statistical error for photon counts is created by taking the square root of the number of accepted photon counts. The output of the sorting routine then contains the average values for the accepted data. It is a list of the microwave frequencies and their corresponding average number of photons per cycle, the error on the average number and the average trap size. The photon counts and trap size backgrounds were identified from the final five data cycles of each set. Then a signal, $S(\nu)$, for each frequency in a data set was produced where

$$S(\nu) = \frac{C(\nu) - C_{back}}{T(\nu) - T_{back}} \tag{5.29}$$

and $C(\nu)$ is the average photon counts, C_{back} is the average photon counts background, $T(\nu)$ is the trap size and T_{back} is the trap size background.

For each set $S(\nu)$ was fitted to determine the center frequency. A basic Rabi resonance shape was used for the fitting,

$$\begin{aligned} R(\nu) \quad = B + A \sum_{i=\pm} \quad & \frac{\Gamma^2}{\left[2\pi(\nu - \nu_{HFS} \pm \frac{W}{2})\right]^2 + \Gamma^2} \\ & \times \sin^2\left(\sqrt{[2\pi(\nu - \nu_{HFS} \pm \frac{W}{2})]^2 + \Gamma^2}\,\frac{t}{2}\right). \end{aligned} \tag{5.30}$$

The broadening caused by the mechanisms discussed in the previous section is parameterized by a frequency spread variable, W. The other parameters are the amplitude A, the offset B, the center frequency ν_{HFS}, the microwave frequency ν, and the microwave power parameter Γ. The microwave pulse time, t, was fixed at 1 ms. All the data were fit with $R(\nu)$ and center frequencies were determined. Figure 5.9 and Figure 5.10 show fitted hyperfine resonances for ^{21}Na and ^{23}Na. The ^{21}Na data had less microwave power than the ^{23}Na data so the side bumps are less pronounced. Data at two bias field settings, 0.6 and 2.1 gauss, had extra broadening and were fit with Lorentzians. As W increases the fit, $R(\nu)$, becomes double peaked (the two individual Rabi shapes become resolved) and it no longer accounts for the additional broadening. In this case a Lorentzian is an appropriate fitting function as it represents a blurred Rabi shape with the side oscillations averaged out. The errors assigned to the broad data reflect the additional peak smearing. The final fits gave a listing of peak values and statistical errors for each data set. These are shown in Table 5.3.

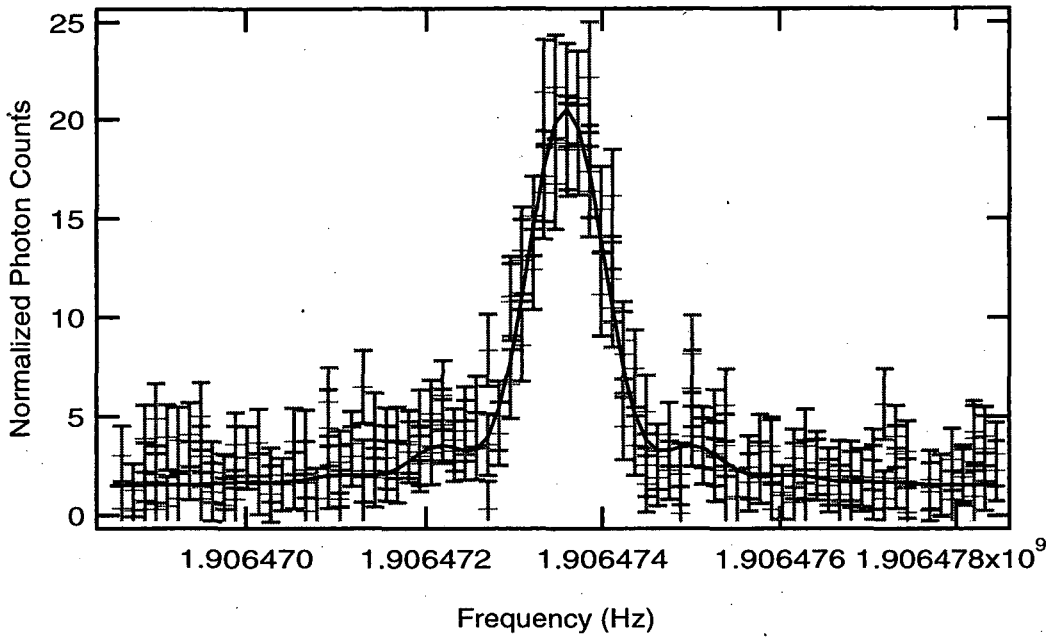

Figure 5.9: The ^{21}Na hyperfine resonance data from run number 5 taken in a 0.92 gauss bias field.

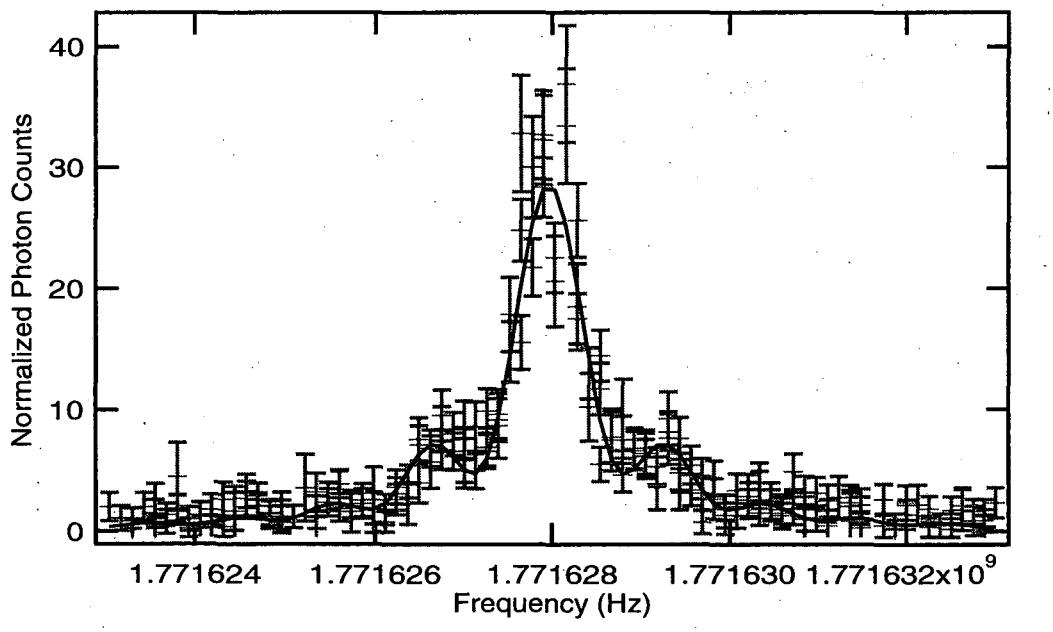

Figure 5.10: The ^{23}Na hyperfine resonance data from run number 9 taken in a 0.92 gauss bias field.

Bias field	Isotope	Run number	Peak frequency (Hz)	Peak error (Hz)
0.92 gauss	^{21}Na		1,906,400,000+	
		2	73566	36
		3	73561	30
		4	73566	21
		5	73591	17
		6	73608	27
		10	73494	27
	^{23}Na		1,771,600,000+	
		8	28028	45
		9	27965	14
		11	28005	11
2.1 gauss	^{21}Na		1,906,400,000+	
		14	81000	40
		15	80931	40
	^{23}Na		1,771,600,000+	
		13	35793	19
		16	35806	13
0.61 gauss	^{21}Na		1,906,400,000+	
		18	72763	200
		19	72699	100
		20	72674	40
	^{23}Na		1,771,600,000+	
		17	26963	6
1.3 gauss	^{21}Na		1,906,400,000+	
		25	75109	57
		26	75234	20
	^{23}Na		1,771,600,000+	
		23	29835	14
		24	29765	9
0.49 gauss	^{21}Na		1,906,400,000+	
		27	72458	46
	^{23}Na		1,771,600,000+	
		28	26671	26
0.72 gauss	^{21}Na		1,906,400,000+	
		30	72993	36
	^{23}Na		1,771,600,000+	
		29	27280	9

Table 5.3: Center frequencies of the hyperfine resonances determined from the fitted data.

local systematic errors	maximum experimental variation	error used
probe frequency	1MHz	7 Hz
slowdown frequency	1 MHz	2 Hz
repump power/main mode power	15±5%	50 Hz
probe power	100μW	10 Hz
trapping beams power	10 mW	20 Hz
slowdown power	1 mW	20 Hz
global systematic errors		
cooling laser detuning	5 MHz	140 Hz
EOM frequency	5 MHz	70 Hz
synthesizer calibration	constant offset	10 Hz

Table 5.4: Systematic uncertainties for the hyperfine measurement.

5.10 Systematic Uncertainties

Section 5.8 discussed systematic shifts due to atom distributions, velocities and the microwave pattern. For this experiment these shifts are minimal. The resonance position results from the strength of the bias magnetic field. Errors result from changes in the experimental parameters that make the effective magnetic field size different, causing the peak position to move. These errors were grouped into two categories, local and global. The local errors cause run to run variations in experimental parameters but are not specific to ^{21}Na or ^{23}Na. They add variation to the data beyond statistics alone. Global errors refer to consistent differences in the treatment of ^{21}Na and ^{23}Na which result in offset of the value of $^{21}\nu_0$ after isotope comparison. Additional data sets were taken off-line with ^{23}Na to estimate these systematic uncertainties by purposely varying experimental parameters. Table 5.4 gives a list indicating the typical variation of a parameter and the uncertainty it would contribute.

Systematic errors result from small changes in the experimental parameters which alter the position of the trap, effectively locating it in a slightly different bias field strength. A change of a few hundredths of a gauss shifts the resonant frequency by one hundred Hz. The balance and power of the laser beams affect the trap placement. Variation in the power of the trapping and slowdown beams contributes to this error. Probe power variation can cause small frequency shifts as well, possibly because of the pushing of the atoms during probing. If the collection of probe fluorescence photons from the atom cloud is uneven

an error arises from different pushing rates. The laser frequency changes cause minimal resonance shifts. But changes in the repump to main mode power ratio do cause significant resonance shifts. This ratio is controlled by the EOM which is fairly unstable. Variation in the fraction of repump power alters the position and size of the trap. The error attributed to this effect is 50 Hz. The local errors combine to give a total error of 60 Hz. This error was added in quadrature with the statistical error of the peak for each of the twenty-five data sets to give the proper weighting to each set.

Different treatment of ^{21}Na and ^{23}Na can create a different frequency shift for the two isotopes. The dominant error here is caused by the uncertainty in the equality of absolute trap laser detunings for ^{23}Na and ^{21}Na. The trapping frequencies were chosen to maximize the trap size and then fixed. Since the trapping frequency range is fairly flat over about 10 MHz this technique can be off by 5 MHz, causing a shift of 140 Hz. Possible inaccuracies in the absolute EOM frequencies for the two isotopes added 70 Hz to the global error. The synthesizer calibration accuracy of 10 Hz was fine in light of these much larger errors. The total global error was 200 Hz. This error is dominated by the overall laser frequency detuning which can be made better with improvements to the laser lock combined with a better detuning determination. The global error is added to the total error at the end of the analysis to give the final error.

5.11 Result

The peak frequency values for each isotope taken at the same magnetic bias field were combined using a weighted average. The peak frequency was obtained for each of the 6 bias field values and both of the isotopes. The shift, $\Delta\nu_{23}$, from the known zero field value for ^{23}Na = 1,771,626,129 Hz [71] was calculated for each bias field value. The bias magnetic field strength was determined from Equation 5.18. The bias field strength ranged from half a gauss to two gauss. The corresponding frequency shifts ranged from 0.5 kHz to almost 9 kHz. Table 5.5 gives these data values.

The data in Table 5.5 are fit using the equation,

$$^{21}\nu_{HFS} = {}^{21}\nu_0 + 0.92937(3)\Delta\nu_{23}. \tag{5.31}$$

A least squares fit gives a value of $^{21}\nu_0 = 1,906,471,870 \pm 30$ Hz with $\chi^2 = 7$ (n=6). This procedure is equivalent to finding a value for $^{21}\nu_0$ at each bias field and taking a weighted

Bias Field (gauss)	$^{21}\nu_{HFS} - 1,906,400,000$ (Hz)	Error in $^{21}\nu_{HFS}$ (Hz)	$\Delta\nu_{23}$ (Hz)	Error in $\Delta\nu_{23}$ (Hz)
0.92	73,565	27	1867	38
2.1	80,966	51	9671	44
0.61	72,687	59	834	60
1.3	75,188	50	3670	43
0.49	72,458	76	542	65
0.72	72,993	70	1151	61

Table 5.5: The hyperfine peak frequencies for ^{21}Na ($^{21}\nu_{HFS}$) and the shifts from zero field frequencies for ^{23}Na ($\Delta\nu_{23}$) for different bias field values.

average. Figure 5.11 shows a graph of this data with the fit. The errors shown in the residue plot combine the error in $^{21}\nu_{HFS}$ and the error in $\Delta\nu_{21}$ which is 93% of the error in $\Delta\nu_{23}$. Figure 5.12 shows the same data in another way. The peak values of ^{21}Na are plotted against the bias magnetic field strength. The data are fit with

$$^{21}\nu_{HFS}(B) = {}^{21}\nu_0 + 2062(\text{Hz/gauss}^2)B^2. \tag{5.32}$$

The final result for the zero-field splitting of the ground state of ^{21}Na includes the global error and is $^{21}\nu_0 = 1,906,471,870\pm200$ Hz.

5.12 Discussion

This experiment demonstrates how trapping techniques can be applied to spectroscopy of unstable isotopes. The trap measurement of the ground state hyperfine splitting of ^{21}Na improves by a factor of one hundred the previous measurement performed with an atomic beam [32]. Another factor of ten improvement could be made with closer attention to systematics but with the same basic apparatus. This technique can be useful in rare and short-lived alkalis for precise hyperfine spectroscopy on strings of isotopes. A group at CERN [75] is working on hyperfine spectroscopy of cesium isotopes in small and large magnetic fields. Both magnetic moments and zero-field splittings will be found.

The magnetic field of the atomic electrons interacts with the nuclear magnetization to create hyperfine structure. Because the magnetic field is non-uniform over the nucleus the hyperfine structure depends to a small degree on the spatial distribution of the nuclear magnetization. This effect is called the hyperfine structure anomaly or the Bohr-Weisskopf

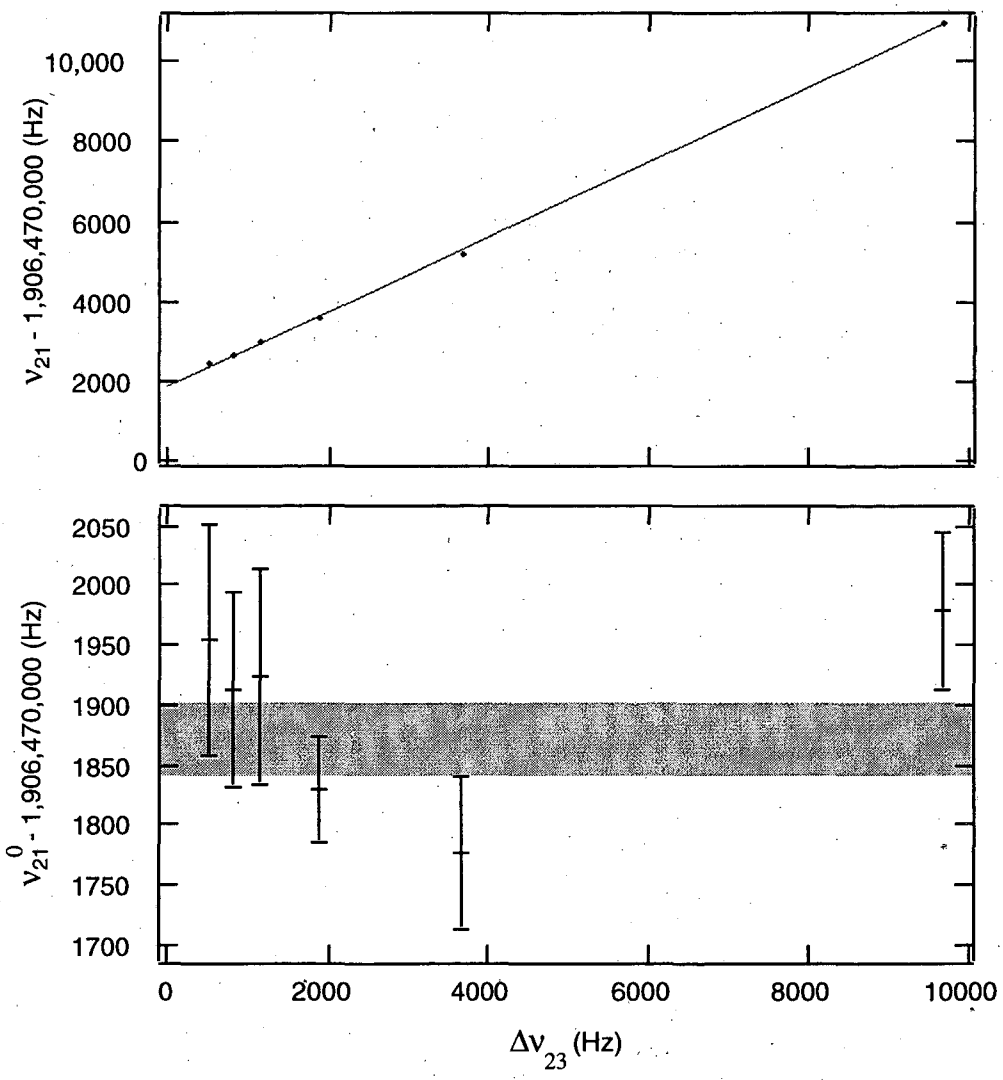

Figure 5.11: Graph of the peak values of the ^{21}Na hyperfine resonances plotted against the ^{23}Na resonance shifts.

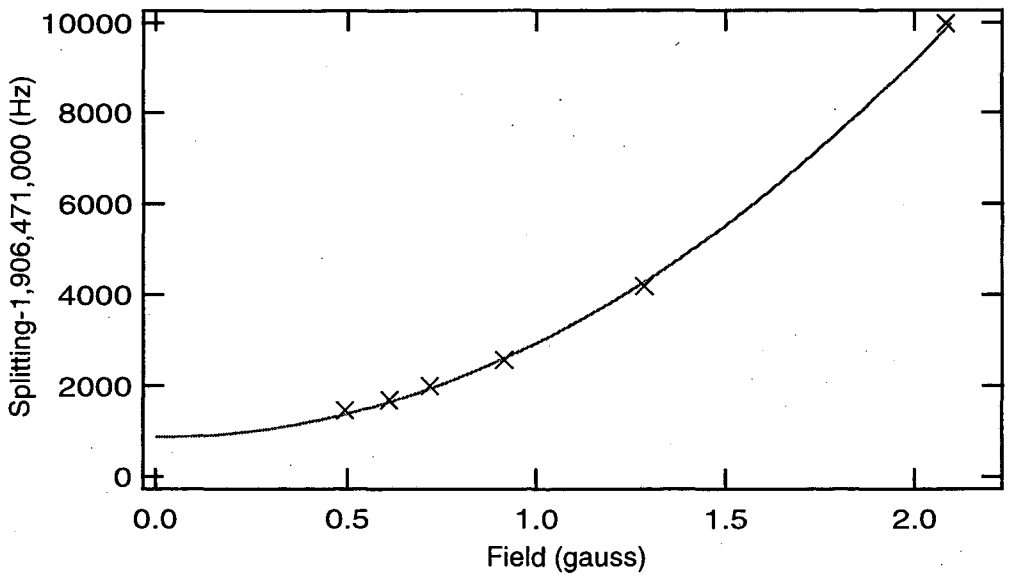

Figure 5.12: Graph of the peak values of the ^{21}Na hyperfine resonances plotted against the bias magnetic field strength.

effect [76]. The magnetic moment is determined from the interaction of an external uniform field with the nuclear magnetization and is insensitive to the magnetization distribution. A comparison between the magnetic moment inferred from the hyperfine structure and the measured magnetic moment reveals the hyperfine structure anomaly. In practice a comparison between two isotopes is made to avoid atomic calculations. The magnetic moment of one isotope is calculated using its hyperfine splitting and the other isotope's splitting and moment as inputs into the Fermi-Segré formula, see Equation 5.20. The difference between the actual and calculated magnetic moments is the the relative Bohr-Weisskopf anomaly between the two isotopes and can be used to check nuclear models.

The Bohr-Weisskopf effect is predicted to be -6 to -8×10^{-5} for ^{21}Na[32]. With a complementary measurement of the magnetic moment of ^{21}Na to about 10^{-5} via hyperfine structure in a large magnetic field it should be possible to measure the Bohr-Weisskopf effect for ^{21}Na. Another option which is currently being pursued in our lab[77] is a measurement of the hyperfine splitting between the $3P_{1/2}(F = 1)$ and $3P_{1/2}(F = 2)$ levels. A comparison of the magnetic dipole hyperfine interaction constants for two atomic states ($3S_{1/2}$ and $3P_{1/2}$) which have different overlap with the nucleus is made. By comparing these measurements on two isotopes the hyperfine anomaly can be determined[78]. If the $3P_{1/2}$ splitting can be

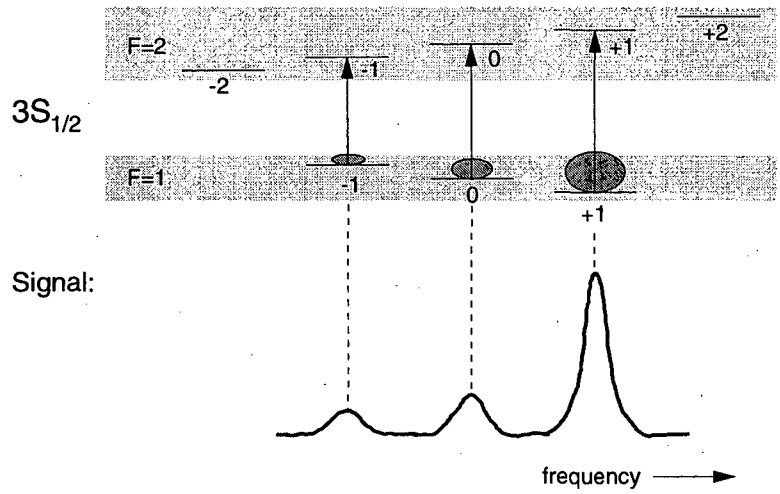

Figure 5.13: Diagram illustrating polarization determination by probing the $\Delta m = 0$ groundstate transitions.

measured to a challenging precision of 10 KHz the hyperfine anomaly should be detected with this method.

Microwave spectroscopy is a promising technique for characterizing nuclear polarization. Precise knowledge of nuclear polarization will allow the physics of interest to be extracted from beta decay measurements. For instance, the experimentally observed up/down asymmetry of the betas emitted from polarized nuclei requires a measure of polarization to extract the fundamental beta-asymmetry coefficient. In work with a cesium atomic beam [79] magnetic sublevel populations were determined to less than one percent by probing individual sublevels with microwaves. A similar scheme will work in sodium. The hyperfine measurement is the first step, showing that the signals are big enough to be seen from this experiment's small amount of trapped atoms. In addition to the $m = 0 \rightarrow m = 0$ transition the other $\Delta m = 0$ transitions, $m = +1 \rightarrow m = +1$ and $m = -1 \rightarrow m = -1$, can be probed with microwaves in the same way. Figure 5.13 shows the $3S_{1/2}$ groundstate with the hyperfine levels, $F = 1$ and $F = 2$, and their magnetic sublevels. Optical pumping can place most of the atoms in the $F = 1, m = +1$ state but not 100%. A method is needed to measure how many atoms are in the $F = 1, m = 0$ and $m = -1$ states. The circles in Figure 5.13 represent the different magnetic sublevel populations. After optical pumping most of the population is in the $F = 1, m_F = +1$ level. In a small magnetic field these three transitions are well separated in frequency. By scanning through the three transitions

the relative peak heights of the three transitions can be measured. Then by comparing these heights to the heights when the atoms are pumped evenly into the three levels the populations of each level can be calculated. The difficulty with this technique is that the other transitions are hard to see without extremely uniform magnetic fields. The frequency of the other transitions shift linearly with the applied magnetic field, 1400 Hz/milligauss, so field inhomogeneities cause more peak smearing. Just a 10 milligauss field nonuniformity causes a peak broadening of 14 KHz. Better field uniformity combined with higher microwave power to broaden the peaks can make these transitions measurable. The width of the resonance envelope is $2\Gamma \propto \sqrt{S}$. More microwave power can increase the resonance width so the resonance will not be blurred out by the field non-uniformities. For the case of a 10 milligauss field non-uniformity two hundred times more microwave power than the current π pulse power would be necessary. These transitions can be measured by arranging better magnetic fields, higher microwave power, and improved antenna efficiency.

Chapter 6

Preliminary Beta Decay Studies

This chapter addresses the detection of positrons from the beta decay of the trapped ^{21}Na. We used a simple beta detector to evaluate the prospects of beta decay studies with trapped atoms. Tests in the original trapping chamber and a secondary chamber into which atoms were transferred from the original chamber were made. The main conclusion, the backgrounds are large, stands out clearly. Further effort is then made to understand the source of the backgrounds in order to guide future design decisions.

6.1 The Beta Detector

We constructed a beta telescope to detect the positrons from the beta decay, $^{21}\text{Na}\rightarrow{}^{21}\text{Ne}+e^{+}+\nu_e$, of the trapped ^{21}Na atoms. The beta telescope consists of two plastic scintillators spaced apart as is shown in Figure 6.1. The ΔE scintillator is 1.0 mm thick and 1.27 cm in diameter. The E scintillator is 2 cm thick and 2.54 cm in diameter. The E scintillator is spaced 1.9 cm from the ΔE as shown in Figure 6.1. Each scintillator is glued to an acrylic lightguide attached to a phototube. The beta telescope provides spatial discrimination and gamma ray suppression. A positron generates coincident events in both the ΔE and E detectors. A typical positron from the decay of trapped ^{21}Na (located downward in Figure 6.1) passes through the ΔE, losing about 0.2 MeV of energy, and enters the E detector where it is stopped. The positron must originate within the geometric acceptance of the detector in order to pass through both the ΔE and E detectors to register a coincidence. Gamma rays are detected when they Compton scatter in the plastic and the resulting energetic electron produces a scintillation signal. The coincidence requirement

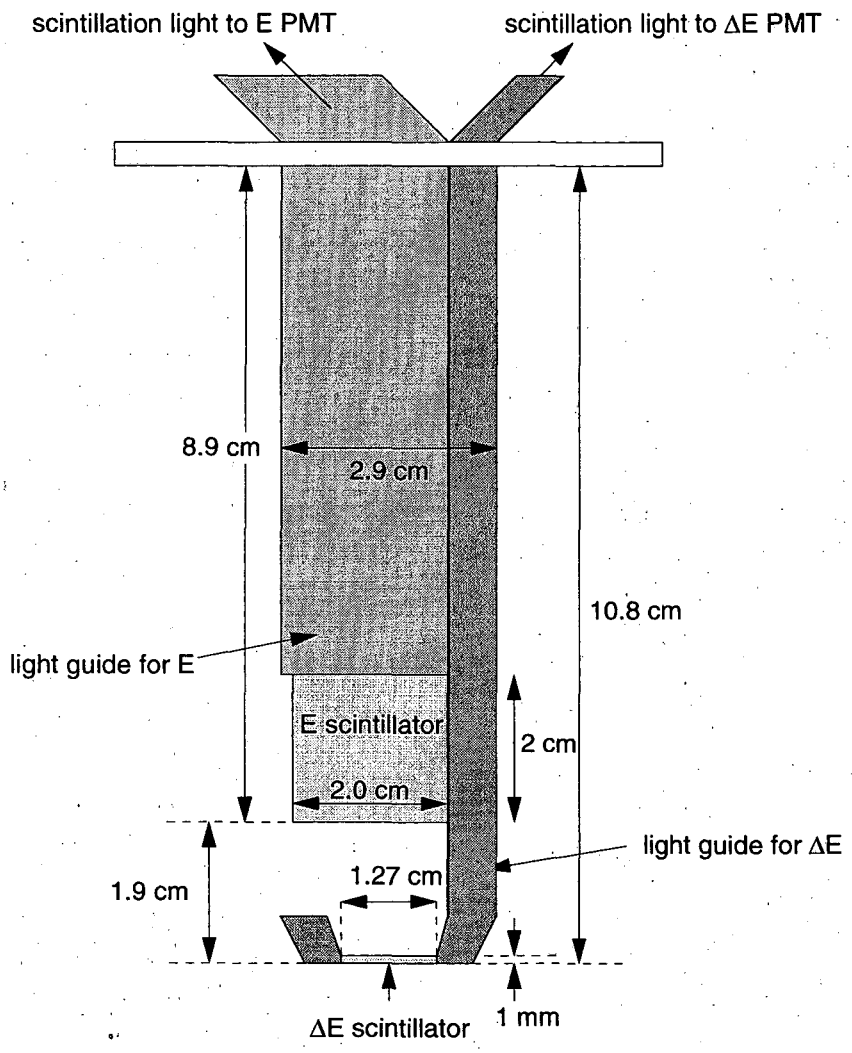

Figure 6.1: The beta detector used for detecting the beta decay of the trapped ^{21}Na atoms.

between two detectors suppresses gamma-ray generated backgrounds.

The electronics for the beta telescope are basically the same as for the NaI detectors discussed in Section 3.4. Instead of the phototube signals from the NaI crystals, PMT A and PMT B, the phototube signals from the E and ΔE detectors are fed into the circuitry shown in Figure 3.6. The ADC's, TDC and scalers data are again written to tape and sorted off-line. The phototubes for the E and ΔE detectors are 5.08 cm diameter Amprex 2230's, set at -2.00 KV (E) and -2.34 KV (ΔE). We used a calibrated ^{90}Sr source to verify that the detection efficiency after accounting for solid angle is unity for the detector. Suitable energy cuts to remove the low energy background were also determined. In the rate measurements stated below the following energy cuts were used: ΔE is in ADC channels 145-1200 (0.1-0.5 MeV) and E is in ADC channels 200-2000 (0.5-5 MeV). With these energy cuts the detected positrons have the kinetic energy range of 0.7 MeV to 2.5 MeV or 75% of the total beta spectrum. The beta detector fits into a stainless steel sleeve which seals the vacuum. The sleeve allows the detector to be brought close to the trapped atoms. The stainless steel window on the end of the sleeve which the positron must pass through to get to the detector is 4 mil thick. This thickness attenuates the positron energy by about 40 keV. At this stage of tests the energy attenuation and energy dependent backscattering from the sleeve window are not important. The future plan is to use a thin beryllium window to separate the detector from the trap vacuum. This requires evacuating the detector side to keep from breaking the thin window.

6.2 Tests in the Original Trapping Chamber

The beta detector attached to the original trapping chamber at the horizontal port perpendicular to the atomic beam. The ΔE detector was 8.6 cm away from the trapped atoms giving a detector solid angle, Ω_1, equal to 1.4×10^{-3}. We took data with the trap on for 85.1 s and then off for 85.1 s repeatedly to separate the trapped atom signal rate from the background signal rate. The data were cut with the ΔE and E energy cuts listed in Section 6.1 and the resulting rates analyzed. Depending on how we turned off the trap we measured different backgrounds. The basic conclusion from the data is that the backgrounds with the current set-up are very large. A simple model is used to take one step further and try to extract some information on the origins of the background. This information can be used to guide the design of the next generation experiment.

The count rate in the detector while the proton beam was on target swamped the beta decay count rate so the proton beam was cycled and data were taken when it was off. The 2 μA proton beam turned on for 1.0 s and then off for 1.1 s repeatedly. We recorded beta decay counts during the last 1.0 s of the proton off window. The 0.1 s delay between when the proton beam was turned off and the data taking began gave plenty of time for the target bombardment related background to decay away. In a previous test the target bombardment related background was found to decay in less than 400 μs. We recorded the beta decay data described in this section during the "Wedding" Run. We took data with the gate valve located on the tube separating the target and trap regions closed for the entire measurement. The resulting rate was 0.11±0.02 Hz. This rate is subtracted from the stated rates below so that all backgrounds calculated in the following discussion are associated with the atomic beam.

In the first test we turned off the trap by shutting the gate valve on the tube separating the target and trap regions. So the ^{21}Na atomic beam periodically shut off and on again. The background signal from the ^{21}Na atomic beam passing through the trap and the trap signal both cycle on and off. But because the trap signal and the background signal decrease with different decay constants the two signals can be separated. The top graph in Figure 6.2 shows how the signal from the trap relates to the signal from the background atoms when the gate valve is flipped every 85.1 s. The trap signal changes with the trap's decay rate, λ_{trap}=0.14 Hz. The background signal changes with the decay rate of ^{21}Na, $\lambda_\beta = 3.1\times^{-2}$ Hz. The bottom graph in Figure 6.2 shows the average rates for both the trap signal and the background signal during the times the gate valve is opened or closed. Since the background signal dominates the rate when the gate valve is closed if that rate is high there is a high background. The count rate with the gate valve open was 2.10 ± 0.05 Hz and the count rate with the gate valve closed was 0.93 ± 0.05 Hz. The continuous running signal rates for the trap, r_{trap}, and the background, r_{back}, were extracted from this data by solving the following set of equations:

$$\begin{aligned} 0.33r_{back} + \ 0.08r_{trap} &= 0.93 \pm 0.05 \\ 0.67r_{back} + \ 0.92r_{trap} &= 2.10 \pm 0.07\ . \end{aligned} \tag{6.1}$$

The result is $r_{trap} = 0.3 \pm 0.2$ Hz and $r_{back} = 2.8 \pm 0.2$ Hz. The trap rate corresponds to 9,000±6,000 atoms which is consistent with the optical signal (8,000 atoms) for this run.

In an effort to understand the source of the high background it was divided into

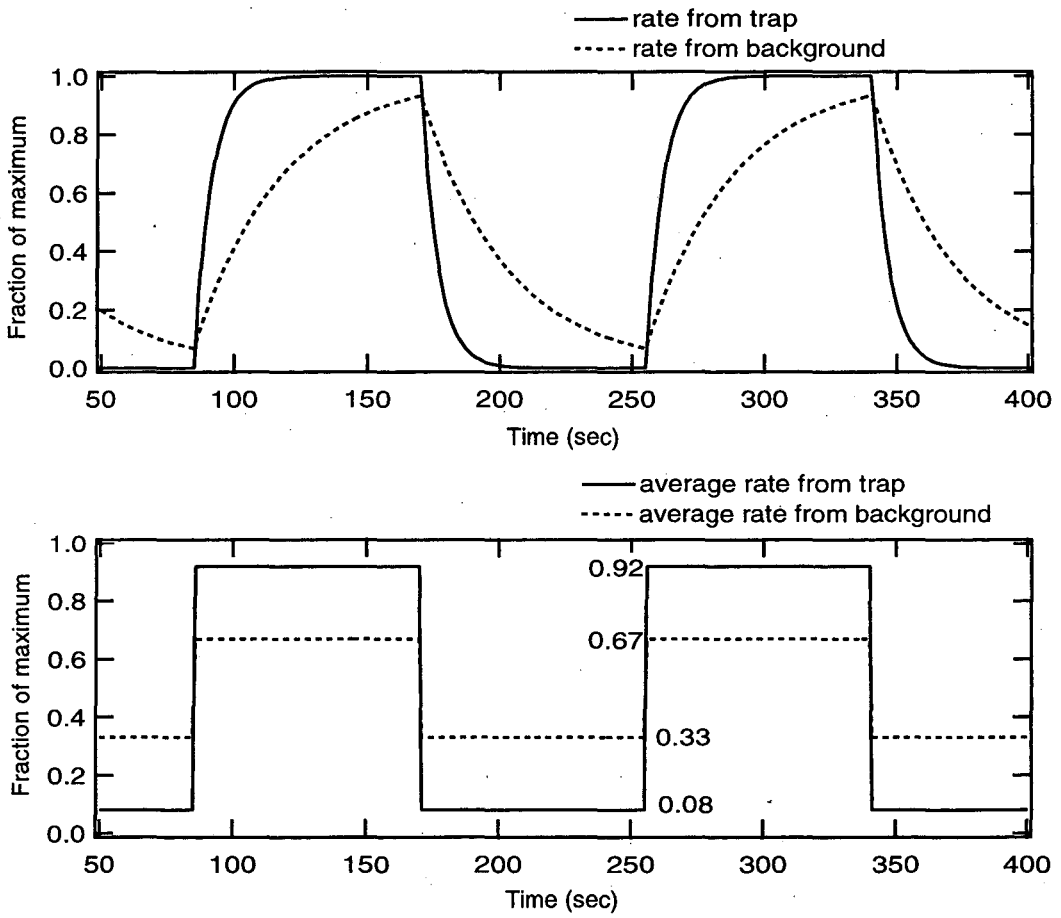

Figure 6.2: Model of the time dependency of the beta decay signals for the trapped atoms and background when the gate valve is opened and closed.

two categories. The background rate caused by the atomic beam without interaction with the trap or trapping lasers is notated r_{beam}. The background from atoms that were in the trap and then lost or never trapped but deflected by the trapping laser beams is notated $r_{deflect}$. One mechanism which contributes to $r_{deflect}$ is ^{21}Na atoms which are captured by the trap but knocked out of the trap by gas atoms before beta decaying. These atoms can stick to the detector window where they have a large detection solid angle. This process has half the effective solid angle of trap beta decay if the detector window is directly on top of the detector and all of the atoms stick to the window. So if the trap decay rate due to poor vacuum is fast compared to the beta decay rate this background can be large. This background can be partially suppressed by geometry. Using a larger detector which is moved back from its sleeve's window will lessen the solid angle from the window to the detector. Ultimately, however, the vacuum needs to be improved.

We took more data with the trapping lasers turning on and off. In this case the beam background signal is constant while the trap signal and deflected background signal vary as before. When the trapping lasers were on the counting rate was 2.87 ± 0.09 Hz. When the trapping lasers were off the counting rate was 2.47 ± 0.09 Hz. The following equations result:

$$\begin{aligned} 0.92r_{trap} + r_{beam} + 0.67r_{deflect} &= 2.87 \pm 0.09 \\ 0.08r_{trap} + r_{beam} + 0.33r_{deflect} &= 2.47 \pm 0.08\ . \end{aligned} \tag{6.2}$$

A third condition is needed to solve this set of equations. Using $r_{back} = 10 \times r_{trap}$ from above gives $r_{deflect} = 0.5 \pm 0.4$ Hz and $r_{beam} = 2.3 \pm 0.1$ Hz. In the first chamber it appears that the dominant background is from the atomic beam.

6.3 Transferring Atoms to a Second Chamber

We transferred atoms from the original collection MOT to a second MOT in an effort to lower the beta background associated with the uncollected ^{21}Na in the atomic beam. By gently tossing the ^{21}Na from one trap to the other most of the ^{21}Na sent through the tube between the traps should be trappable in the second trap. In addition, by transferring atoms the ^{21}Na loading the experimental trap will be bunched in time instead of continuous. This bunched beam will be useful for a polarized nuclei experiment where the efficient collecting but unpolarized trap, the MOT, will not be on during the data taking. A polarized trap

such as a magnetic trap or a polarized dipole trap can not be efficiently loaded from an atomic beam and therefore must be loaded from a MOT. With bunched transfer no ^{21}Na beam will pass through the polarized trap and be wasted during the data taking. When more atoms are needed in the polarized trap the efficient MOT can be turned back on and the bunch of atoms collected in the first MOT sent over. The polarized trap is then loaded from the MOT and data taking begins again.

We transferred the atoms from the original collection MOT to a second MOT separated from the original by 51 cm using a technique demonstrated for rubidium[80]. After the original MOT was shut off a pulsed push beam aimed at the atoms and down the transfer tube sent the atoms down the transfer tube. The push beam was circularly polarized so that the atoms were optically pumped into a weak field seeking magnetic sublevel of the ground state, either $F = 2, m_F = -2$ or $F = 1, m_F = +1$, during the push. The polarization of an atom adiabatically follows the magnetic field direction resulting in deflection away from regions of high magnetic field magnitude for these weak field seeking states. During their transfer the atoms were magnetically confined in this manner by an axial hexapole field in the transfer tube. The relationship between kinetic energy and magnetic potential energy for sodium gives 20 gauss = $1\text{m}^2/\text{s}^2$ for the $F = 2, m_F = -2$ level. An atom with 1 m/s velocity will be reflected from a change in magnetic field of 20 gauss. For an atom with 2 m/s, 80 gauss is required and so on. For the other hyperfine level, $F = 1, m_F = +1$, the energy shift is half so its relation is 40 gauss = 1 m^2/s^2.

Figure 6.3 shows how the second MOT connects to the original MOT by way of the transfer tube. The atomic beam in the original chamber is out of the page in Figure 6.3 so the transfer tube is in the horizontal plane at 45° to the four trapping beams of the original MOT. The transfer tube is 1.3 cm in diameter and 33 cm long. It is surrounded by three 33 cm long rubberized iron bar magnets. Figure 6.3 shows the cross section of the transfer tube with the size and placement of the magnets. The magnets are magnetized perpendicular to their faces so the resulting field approximates a hexapole configuration. The critical feature for magnetic confinement, a high magnetic field at the tube walls and a low field in the center, is satisfied. The magnetic field strength on the inner surface of the transfer tube is 100-200 gauss. The atoms fed into the tube have transverse velocities less that about 1 m/s (see transfer geometry and velocity below) so the strength of these magnets is adequate.

The second trapping chamber is simply made out of ten 3.81 cm stainless steel

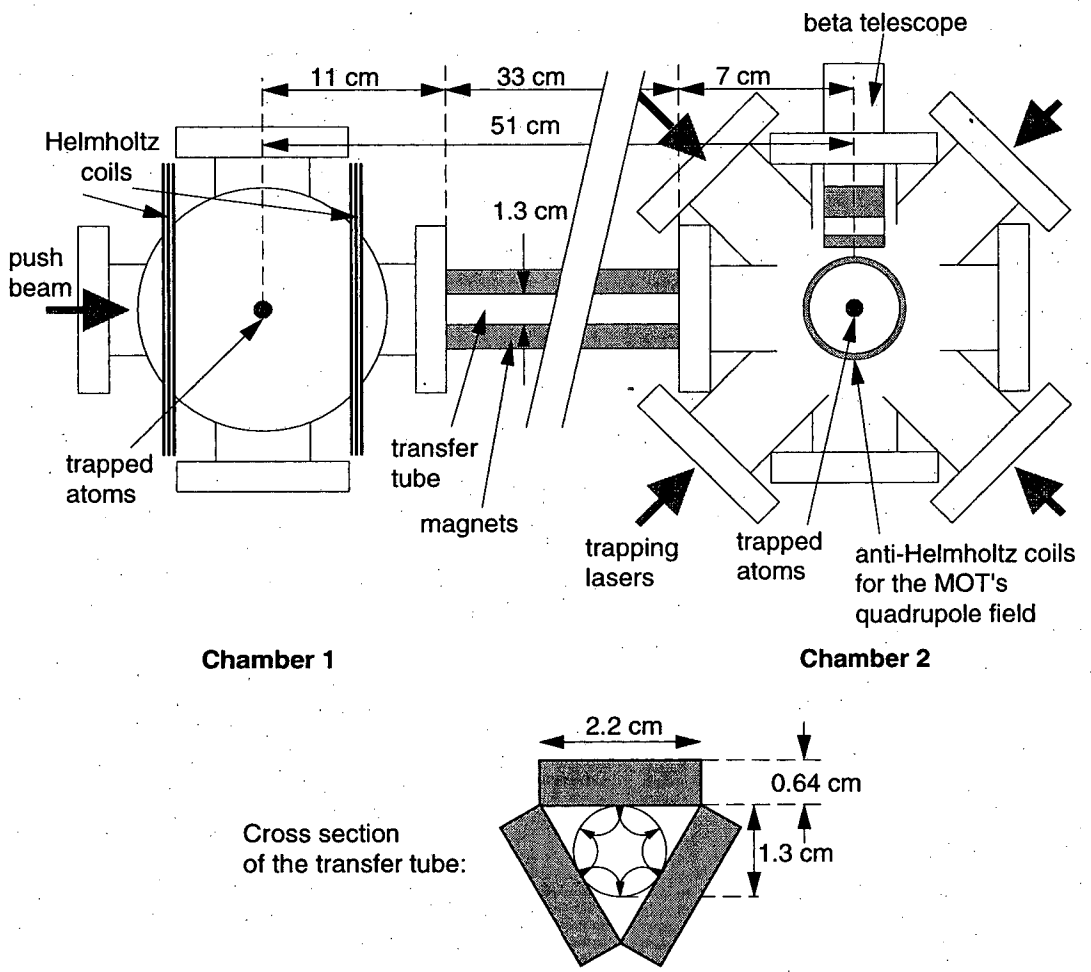

Figure 6.3: The geometry of the transfer tube and the second MOT chamber.

tubes welded together with 6.99 cm flanges on the ends. Eight of the chamber ports are equally distributed in the plane shown in Figure 6.3. Four of the MOT's trapping laser beams enter four of these ports as shown in Figure 6.3. These beams are 1 cm in diameter and have an intensity of 30 mW/cm^2. The other two ports are perpendicular to the page in Figure 6.3. The remaining two trapping beams with 10 mW/cm^2 intensity enter these ports. The chamber is pumped by an 30 l/s Varian ion pump. The anti-Helmholtz coils for the trapping quadrupole field were wound onto the chamber as shown in Figure 6.3. Each coil has 300 turns and is 7.6 cm in diameter. The two coils are spaced 2.5 cm apart and 1 A of current is run through them giving 20 gauss/cm in the axial direction and 10 gauss/cm in the radial direction.

A push beam which was turned on momentarily sent the atoms collected in the original trap to the second trap. Before the push beam was applied, we shut off the lasers and quadrupole field of the original MOT and turned on a homogeneous field for the optical pumping. The coils labeled Helmholtz coil in Figure 6.3 made about a 2 gauss bias field in the direction of the push for optical pumping. After a delay of 1.6 ms the push beam turned on for 1-2 ms. We determined the best set of parameters for transfer by maximizing the number of atoms transferred to the second trap. Two push laser frequency/polarization combinations worked well. Figure 6.4 shows these combinations. The magnetic sublevels of the ground state are shown with their splitting in a magnetic field. The circled level is the level the atoms are optically pumped into for each configuration. With a σ^+ push polarization no EOM sideband frequency was used and the laser frequency was tuned on resonance with $F = 2 \rightarrow F' = 3$. The atoms absorbed hundreds of photons on this cycling transition before making an off resonant transition to the $F' = 2$ level and decaying to the dark $F = 1$ level. The atoms absorbed a sufficient number of photons to gain enough velocity to be aimed efficiently down the transfer tube. A 1 ms push time was used. In the case of σ^- polarization where there is no dark state a laser tuning of +25 MHz above the $F = 2 \rightarrow F' = 3$ transition worked the best. This frequency is in resonance with atoms moving 15 m/s away from the push. An EOM sideband frequency pumped the atoms out of the $F = 1$ level so when the push was done most of the atoms were in the $F = 2, m_F = -2$ level. A 2 ms long push pulse worked best. A longer pulse was probably needed because the atoms began at rest and out of resonance with the laser so the initial acceleration was less. For both push beam configurations switching the push beam polarization or holding field direction reduced the transferred number of atoms by about a factor of five. This indicates

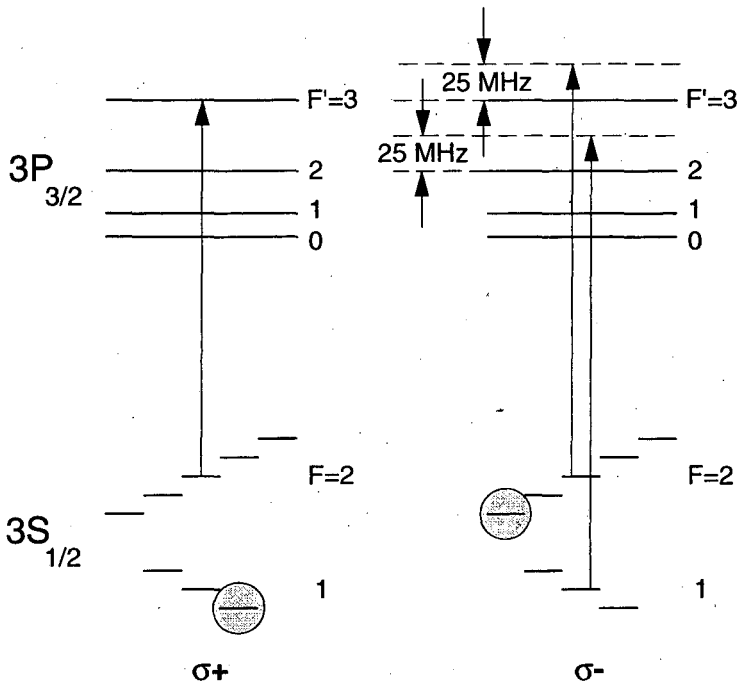

Figure 6.4: Push beam frequency settings for transferring the atoms from the original MOT to a second MOT.

that a high degree of optical pumping to the correct weak field seeking states occurred.

We determined the transit time of the atoms by monitoring the traps' fluorescence on an oscilloscope. Typically the atoms first reached the second trap 30 ms after the push and continued to load for another 30 ms. Given the 51 cm travel distance the final atom velocities after the push were 9-17 m/s. An efficient transfer system has a large enough transfer tube opening angle to accept all of the pushed atoms. For our set-up the angle for entry into the transfer tube from the first trap, the angle from horizontal to the tube wall from the trap center, is 3°. The initial transverse velocity of the atoms must be below 0.5 m/s for the low velocity (9 m/s) atoms to enter the transfer tube. For trapped sodium atoms at the Doppler temperature of 240 μK the median velocity is 0.5 m/s. Most of the atoms will therefore have initial transverse velocities below 0.5 m/s and will be transferred. In the current apparatus the trade-off is between how well the slow atoms can be pushed into the tube and how well the fast atoms can be loaded into the second trap. In the final design of a transfer system a larger entry angle, about 6° should be used. Then a slower transfer speed could be used. All of the atoms would enter the transfer tube and the second trap would load efficiently from a slower transferred beam.

The σ^- configuration worked slightly better than the σ^+ one. It was used for the ^{21}Na. The following data are also for the σ^- configuration. Phototubes monitored the fluorescence from each trap. The phototube for the first trap viewed the trapped atoms through the 45° upward angle port. It collected light with a 2.54 cm lens, 15.7 cm away from the trapped atoms with a solid angle, $\Omega_1 = 1.6 \times 10^{-3}$. The second trap was viewed through the port opposite the push beam port by a 2.54 cm lens, 13.2 cm from the trap. In order to keep the push beam from entering the PMT the lens was offset by 2.2 cm from the center of the port so only trap light was collected. Its effective solid angle was $\Omega_2 = 1.7 \times 10^{-3}$. We measured the transfer efficiency by recording the changes in both trap brightnesses as the atoms are repeatedly pushed from the first trap to the second. Figure 6.5 shows the two trap brightnesses as ^{23}Na atoms are transferred every 2 seconds. The data were taken when trap 1 was in equilibrium. After the push its brightness decreased as atoms were sent to the second trap. Then, until the next push, more atoms loaded into the first trap. The second trap was turned on in the middle of the data scan by switching on its quadrupole trapping field. The second trap received its first atom bunch at about 34 sec in Figure 6.5. The bunched loading makes the steplike structure in the trap brightness. Finally the brightness of the second trap reached equilibrium and its trap brightness decayed between atom bunches by

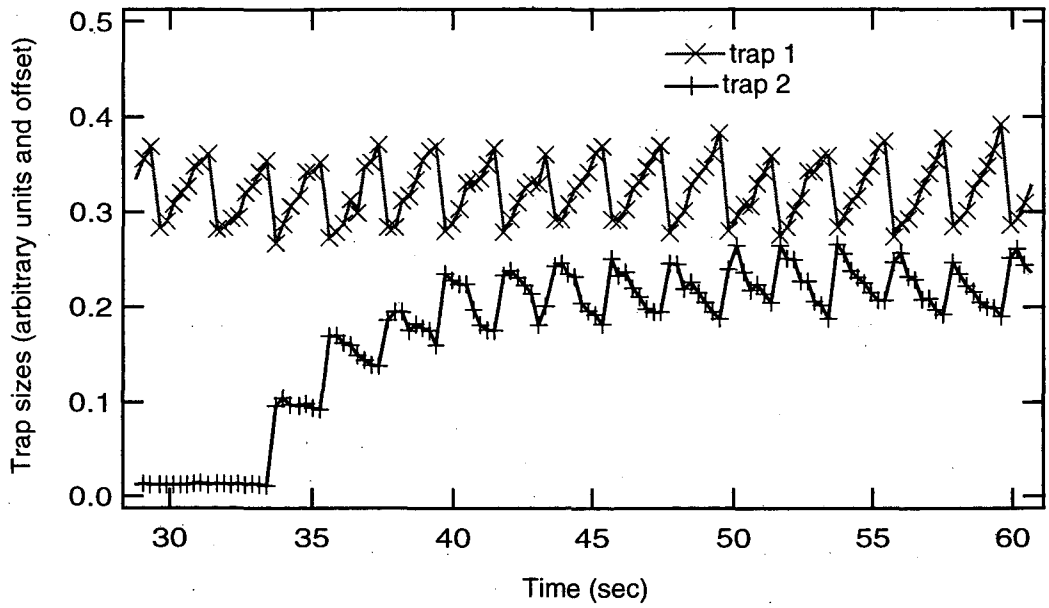

Figure 6.5: Brightnesses of first and second trap during atom transfer between them.

the amount it was loaded by each atom bunch. For the data shown in Figure 6.5 the first phototube was misalligned so the following numbers are only relative. We determined the transfer efficiency by taking the ratio of the step brightnesses adjusted for the solid angles of the two phototubes. The transfer efficiency, e_t, was 80%. The total number of atoms collected in trap 2 is related to the two trap lifetimes as well as the transfer efficiency. If no atoms are lost in the first trap before being transferred (the transfer rate $r_t \gg \lambda_1$) then the total number of atoms in trap 2, N_2, is

$$N_2 = \frac{e_t N_1 \lambda_1}{\lambda_2} \ . \tag{6.3}$$

Here N_1 is the number of atoms in trap 1 without transfer. The trap 1 (2) decay rate is λ_1 (λ_2). For the data in Figure 6.5, $N_2/N_1 = 90\%$ which is consistent with the measured $\lambda_1 = 0.25$ Hz, $\lambda_2 = 0.15$ Hz, and Equation 6.3 given that 30% of the atoms are lost in the first trap ($r_t \approx \lambda_1$). The actual ratio of trap brightnesses N_2/N_1 measured with correct phototube position before the beam time was 20%. This should be improved with better transfer geometry and a better vacuum in the second chamber.

Another benefit of transferring the atoms is that the vacuum in the first chamber

need not be extremely good. The vacuum in the first chamber is not important as long as the atoms are transferred at a rate fast compared to λ_1. The factor $N_1\lambda_1$ in Equation 6.3 is a constant, independent of vacuum, equal to the first trap's loading rate. The number of atoms in the second trap depends on that loading rate, the transfer efficiency and λ_2 (proportional to the second chamber's vacuum) but not on the first chamber's vacuum. So transferring atoms gives the opportunity to implement yet another stage of differential pumping where the effort is concentrated on the vacuum in the final chamber.

6.4 Tests in the Second Chamber

The beta detector attached to the second chamber at the top port as shown in Figure 6.3. The ΔE detector was 6.1 cm away from trapped atoms giving a detector solid angle equal to 2.7×10^{-3}. During the "Vortex" Run we performed a set of tests like those done in the original chamber and described in Section 6.2 in the second chamber. In this case the second trap was loaded with bunches of atoms transferred about every second from the original trap as described in Section 6.3. The count rate with the gate valve always closed was 0.06 ± 0.01 Hz. This rate is subtracted from the rates stated below.

We once again measured the background by opening and closing the gate valve separating the target region and the original trap. With the second trap active the beta count rate when the gate valve was open (closed) was 1.19 ± 0.07 Hz (0.45 ± 0.05 Hz). Solving a set to equations like Equations 6.1 gives $r_{trap} = 0.37 \pm 0.16$ Hz and $r_{back} = 1.3 \pm 0.2$ Hz. In the second chamber the background signal is "only" 3.5 times the trap signal. The trap signal rate corresponds to 6000 ± 3000 atoms. This number could not be resolved optically with the phototube on the second trap which viewed the trap from a high light background angle. The fluorescence of the trapped atoms was visible by eye, though, and several thousand atoms is a reasonable number estimate. The number of ^{21}Na atoms in the first trap was 35-55 mV or 11,000-17,000 atoms. So with this measurement technique $N_2/N_1 = 40 \pm 20\%$.

Once again the differentiation between deflected and beam backgrounds was made by turning on and off the lasers for the second trap. The rate with the second trap's lasers on (off) was 1.41 ± 0.07 Hz (0.63 ± 0.05 Hz). Using a set of equations like Equations 6.2 and an overall signal to background of 1 to 3.5 gives $r_{deflect} = 1.25 \pm 0.20$ and $r_{beam} = 0.19 \pm 0.09$. The direct beam related background is much less than in the original chamber as expected.

Transferring atoms dramaticly reduced the beam related background because in the second chamber there is no unslowed beam as in the first chamber. Still the background is high, probably from the deflection mechanism discussed in Section 6.2. Again it must be emphasized that a good vacuum is crucial. Even with many improvements to the system the backgrounds with a single detector may be too high for precision measurements. For this reason the new students on the project are working on a microsphere plate detector to detect the recoiling daughter ion from the beta decay. A coincidence measurement with the ion detector and the beta detector would further reduce background.

6.5 Assessment of a Cycling Scheme for a Beta-Asymmetry Measurement

Polarized nuclei are needed for measurement of the beta-asymmetry correlation. One way to polarize the collected atoms is to use a cycle where the atoms are optically pumped into a polarized state some fraction of the time. First the atoms would be trapped in a MOT. Then the trapping laser and field would be turned off and a circularly polarized laser beam would optically polarize the atoms. The decay measurement would then be made as the atom cloud expanded outward in the dark. Finally the MOT would be turned on to recollect the atoms. A simple experiment was run to test the feasibility of such a scheme. We measured the equilibrium number of atoms, N_{ac}, when the trap was rapidly shut on and off and compared it to the trap number, N_{dc}, when the trap was on constantly. For a 6.3 ms trap-on time and a 1 ms (2 ms) trap-off time the ratio, N_{ac}/N_{dc}, was 65% (50%). The cycling introduces an additional loss rate of atoms from the trap. The reduction of the equilibrium trapped number by half for the 2 ms trap-off data means that the total trap loss rate doubled due to the cycling. The loss rate constant without cycling was 0.14 Hz so an additional loss rate of 0.14 Hz is caused by the cycling. The fractional loss per cycle, f_{cycle}, given the cycle time, T_{cycle}, and the cycle loss rate, λ_{cycle}, is

$$f_{cycle} = T_{cycle}\lambda_{cycle} \cdot \tag{6.4}$$

Using λ_{cycle}=0.14 Hz and T_{cycle}=8.3 ms gives f_{cycle} equals 0.1%. The lesson is that very little fractional atom loss can be tolerated per cycle without losing a large fraction of the atoms in a repeated cycle. Better than 99.9% recapture efficiency is needed to make a

cycling scheme work well. Such a scheme will be difficult to implement without additional atom cooling and/or fast magnetic field switching (see Section 5.3).

6.6 The Future

The development of a polarized trap and a recoil ion detection system are the future areas of work for this experiment. A polarized group of atoms is needed for the measurement of the beta-asymmetry parameter. Recoil ion detection can lower the backgrounds and determine the daughter ion's energy and direction. The beta-neutrino correlation parameter is then measured.

There are many possible approaches to trap polarized atoms. Some of these are mentioned briefly here. Section 6.5 outlined a cycling scheme. Another approach which avoids rapid magnetic field switching is using an all optical trap. In the case of a far red-detuned laser the dipole force traps atoms in areas of high laser intensity. Recently a polarized dipole trap was suggested[81] and demonstrated for rubidium atoms[82]. In this trap a single focused laser beam which is polarized makes the trap. The AC-Stark shift is dependent on the magnetic sublevel in this trap so only one magnetic sublevel is trapped. This trap has a high polarization, 98%, but only 20% of the atoms originally in a MOT can be transferred into it. Also the trap lifetime is less than 10 seconds due to optical excitations between magnetic sublevels. Another polarization approach is to use a vortex trap[83]. Trapping in two dimensions results from the same force as in a MOT. The third dimension is coupled to the others by offset laser beams which rotate the atoms into the two trapping dimensions. Circularly polarized beams in the third direction and the application of a constant parallel bias field give polarizations up to 65%. Magnetic traps are yet another possibility. Atoms in weak field seeking states collect in the minimum of the magnetic field. When the minimum is a finite field the atoms are naturally polarized. An Ioffe-Pritchard trap is such a trap[84]. Another is the time-orbiting-potential (TOP) trap[85]. In the TOP trap the magnetic field minimum orbits around the trap center. The atoms are trapped at the time averaged field minimum at the center. The polarization of the atoms rotates at the orbital frequency. The Los Alamos radioactive atom trapping collaboration is building such a trap for a beta-asymmetry experiment[86]. Nearly 100% transfer efficiency from a MOT to a magnetic trap is possible[87] but additional cooling and optical pumping must be done before the transfer. The molasses cooling used for additional cooling requires the

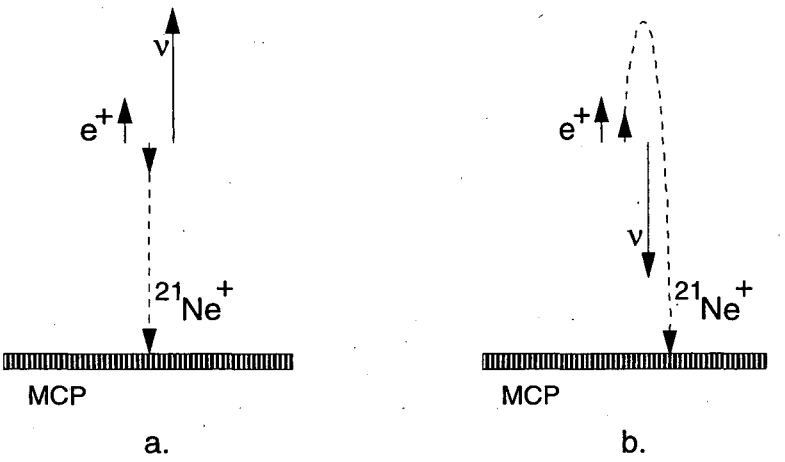

Figure 6.6: Cartoon of a low energy positron decay with the neutrino emitted parallel (a.) and antiparallel (b.) to the positron. The resulting daughter ion trajectories are indicated with dashed lines.

ability to rapidly switch the magnetic fields completely off.

The current focus of this project is the building of a recoil ion detection system. A microsphere plate (MSP) will soon be installed in the trapping chamber about 8 cm below the trapped atom cloud. The beta telescope detector will be installed above the trapped atoms. Electric field rings will apply a constant electric field of about 500 V/cm over the region from the trap center to the MSP. When ^{21}Na decays the daughter, ^{21}Ne, will be produced in many different charge states due to the shake off of atomic electrons[88] during the decay. If two electrons shake off the resulting ion is $^{21}Ne^{+}$. Experiments at TRIUMF[89] have shown that for the similar positron decay of ^{37}K about 20% of the daughter Ar is ionized in the charge states +1, +2, and +3. The ionized daughters are accelerated into the microsphere plate and detected. Coincidence detection of the decay positron and the daughter ion will reduce the current background levels by discriminating against background from the vacuum chamber walls. From the timing between the essentially immediate hit of the upward going beta and the arrival of the accelerated ion at the MCP in combination with the beta energy the beta-neutrino correlation can be extracted. The low energy beta decays are particularly sensitive. Figure 6.6 shows a decay with a low energy positron which is detected in the upward direction at the beta telescope detector. The neutrino

carries away most of the energy of the decay, represented by the long arrow. If the positron and neutrino are emitted in the same direction, as in Figure 6.6 a., then the daughter ion is emitted straight down and arrives quickly at the MSP. On the other hand, if the positron and neutrino are emitted in the opposite directions, as shown in Figure 6.6 b., then the daughter ion is emitted straight up and takes a longer time to reach the MSP. From the timing spectrum of the arrival times of the daughter ions the beta-neutrino correlation can be extracted. The next step after the MSP experiments will be to install a position sensitive multichannel plate detector in place of the MSP. With the landing position of the daughter ion as well as the timing the complete kinematics of the decay can be determined.

Bibliography

[1] E.Z. Fermi, Z. Phys. **88**, 161 (1934).

[2] B.M. Rustad and S.L. Ruby, Phys. Rev. **97**, 991 (1955).

[3] W.P. Alford and D.R. Hamilton, Phys. Rev. **94**, 779 (1954).

[4] T.D. Lee and C.N. Yang, Phys. Rev. **104**, 254 (1956).

[5] C.S. Wu, *et al.* , Phys. Rev. **105**, 1413 (1957).

[6] R.L. Garwin, L.M. Lederman, and M. Weinrich, Phys. Rev. **105**, 1415 (1957).

[7] J.I. Friedman and V.L. Telegdi, Phys. Rev. **105**, 1681 (1957).

[8] M.T. Burgy, *et al.* , Phys. Rev. **107**, 1731 (1957).

[9] M. Goldhaber, L. Grodzins, and A.W. Sunyar, Phys. Rev. **109**, 1015 (1958).

[10] W. B. Herrmannsfeldt, D.R. Maxson, P. Stahelin, and J.S. Allen, Phys. Rev. **107**, 641 (1957).

[11] R.P. Feynman and M. Gell-Mann, Phys. Rev. **109**, 193 (1958).

[12] C.S. Wu and S.A. Moszkowski, *Beta Decay*, (Interscience Publishers, New York, 1966).

[13] J.A. Behr, *et al.* , Phys. Rev. Lett. **79**, 375 (1997).

[14] R. Guckert, *et al.* , Phys. Rev. A **58**, R1637 (1998).

[15] A. Young (young@young96.princeton.edu), (private communication).

[16] P. Bopp, *et al.* , Phys. Rev. Lett. **56**, 919 (1986).

[17] B. Yerozolimsky, I. Kuznetsov, Y. Mostovoy, and I. Stepanenko, Phys. Lett. B **412**, 240 (1997).

[18] H. Abele, *et al.* , Phys. Lett. B **407**, 212 (1997).

[19] P. Liaud, *et al.* , Nuclear Phys. A **612**,53 (1997).

[20] G. Azuelos and J.E. Kiching, Phys. Rev. C **12**, 563 (1975).

[21] D.E. Alburger, Phys. Rev. C **9**, 991 (1974).

[22] G. Audi and A.H. Wapstra, Nuclear Phys. A **595**, 409 (1995).

[23] *Table of Radioactive Isotopes*, Eds. E. Browne, R.B. Firestone, and V.S. Shirley, (John Wiley and Sons, New York, 1986).

[24] E.D. Commins and P.H. Bucksbaum, *Weak Interactions of Leptons and Quarks*, (Cambridge University Press, Cambridge, 1983).

[25] J.D. Jackson, S.B. Treiman, and H.W. Wyld, Phys. Rev. **106**, 517 (1957).

[26] F.C. Barker, B.A. Brown, W.Jaus, and G. Rasche, Nuclear Phys. A **540**, 501 (1992).

[27] W. Jaus and G. Rasche, Phys. Rev D **41**, 166 (1990).

[28] J. Deutsch and P. Quin, in *Precision tests of the standard electroweak model*, edited by P. Langacker (World Scientific, River Edge, N.J., 1995).

[29] I.S. Towner and J.C. Hardy, Los Alamos e-Print Archive, http://xxx.lanl.gov/, nucl-th/9809087, (Sept. 29, 1998).

[30] O. Naviliat-Cuncic, T.A. Girard, J. Deutsch, and N. Severijns, J. Phys. G **17**, 919 (1991).

[31] B.R. Holstein, *Weak Interactions in Nuclei*, (Princeton University Press, Princeton, 1989).

[32] O. Ames, E.A. Phillips, and S.S Glickstein, Phys. Rev. **137**, B1157 (1965).

[33] P. Raghavan, At. Nucl. Data Tables **42**, 189 (1989).

[34] B.R. Holstein, Rev. Mod. Phys. **46**, 789 (1974).

[35] B.R. Holstein, Phys. Rev. C **9**, 1742 (1974).

[36] A.S. Carnoy, *et al.* , J. Phys. G **18**, 823 (1992).

[37] M.A.B. Bég, R.V. Budny, R. Mohapatra, and A. Sirlin, Phys. Rev. Lett. **38**, 1252 (1977).

[38] J. van Klinken, J. Phys. G **22**, 1239 (1996).

[39] V.A. Wichers, T.R. Hageman, J. van Klinken, H.W.Wilschut, and D. Atkinson, Phys. Rev. Lett. **58**, 1821 (1987).

[40] A.S. Carnoy, J. Deutsch, T.A. Girard, and R. Prieels, Phys. Rev. Lett. **65**, 3249 (1990).

[41] A. Jodidio, *et al.* , Phys. Rev. D **34**, 1967 (1986).

[42] N. Severijns, *et al.* , Nuclear Phys. A **629** 423 (1998).

[43] S. Abachi, *et al.* , Phys. Rev. Lett. **76** 3271 (1996).

[44] G. Beall, M. Bander, and A. Soni, Phys. Rev. Lett. **48** 848 (1982).

[45] P. Langacker and U. Sankar, Phys. Rev. D **45** 278 (1992).

[46] R. Barbieri and R.N. Mohapatra, Phys. Rev. D **39** 1229 (1989).

[47] P. Herczeg, in *Precision tests of the standard electroweak model*, edited by P. Langacker (World Scientific, River Edge, N.J., 1995).

[48] A.I. Boothroyd, J. Markey, and P. Vogel, Phys. Rev. C **29** 603 (1984).

[49] A.S. Carnoy, J. Deutsch, andP. Quin, Nuclear Phys. A **568** 265 (1994).

[50] E.G. Adelberger, Phys. Rev. Lett. **70** 2856 (1993).

[51] Z.-T. Lu, Ph. D. thesis, University of California at Berkeley (1994).

[52] K.J. Ross and B. Sonntag, Rev. Sci. Instrum. **66**, 4409 (1995).

[53] V. Hughes and H. Schultz, *Methods of Experimental Physics*, (New York Academic Press, New York, 1967), Vol.4, p.155.

[54] P. Clausing, Physica **9**, 65 (1929).

[55] *CRC Handbook of Chemistry and Physics*, 61st Edition, Eds. R. Weast and M. Astle, (CRC Press, Inc., Boca Raton, Florida, 1981).

[56] G.F. Knoll, *Radiation Detection and Measurement*, (John Wiley & Sons, New York, 1989).

[57] W. Gruhle and B. Kober, Nuclear Phys. A **286**, 523 (1977).

[58] J. Behr (behr@triumf.ca), (private communication).

[59] J.F. Ziegler, J.P. Biersack, and U. Littmark, *The Stopping and Range of Ions in Solids*, (Pergamon Press, New York, 1985).

[60] S.J. Farlow, *An Introduction to Differential Equations and Their Applications* (McGraw-Hill, San Francisco, 1994), pp. 545-550.

[61] S. Chu, L. Hollberg, J. Bjorkholm, A. Cable, and A. Ashkin, Phys. Rev. Lett. **55**, 48 (1985).

[62] P.D. Lett, *et al.* , J. Opt. Soc. Am. B **6**, 2084 (1989).

[63] W.D. Phillips and H. Metcalf, Phys. Rev. Lett. **48**, 596 (1982).

[64] V.S. Bagnato, *et al.* , J. Opt. Soc. Am. B **6**, 2171 (1989).

[65] D.J. Wineland and W.M. Itano, Phys. Rev. A **20**, 1521 (1979).

[66] E.L. Raab, M. Prentiss, A. Cable, S. Chu, and D.E. Pritchard, Phys. Rev. Lett. **59**, 2631 (1987).

[67] D.W. Sesko and C.E. Wieman, Optics Letters **14**, 269 (1989).

[68] N.F. Ramsey, *Molecular Beams*, (Oxford University Press, London, 1956).

[69] A. Corney, *Atomic and Laser Spectroscopy*, (Clarendon Press, Oxford, 1977).

[70] *Physical Review D, Review of Particle Properties*, August 1994, Eds. L.S. Brown and D.L. Nordstrom, (The American Physical Society, Ridge, NY, 1994).

[71] A. Beckmann, K.D. Böklen, and D. Elke, Z. Phys. **270**, 173 (1974).

[72] S. Millman, Phys. Rev. **55**, 628 (1939).

[73] D.J. Wineland and H. Hellwig, Metrologia **13**, 173 (1977).

[74] J. Vanier, A.G. Mungall, and J.-S. Boulanger, Metrologia **20**, 101 (1984).

[75] H.T. Duong, *et al.* , CERN-PPE/92-147, (1992).

[76] A. Bohr and V.F. Weisskopf, Phys. Rev. **77**, 94 (1950).

[77] J. Abo-Shaeer, Undergraduate thesis, University of California at Berkeley (1999).

[78] J.R. Persson, Eur. Phys. Jour. A **2**, 3 (1998).

[79] B.P. Masterson, C. Tanner, H. Patrick and C.E. Wieman, Phys. Rev. A **47**, 2139 (1993).

[80] C.J. Myatt, N.R. Newbury, R.W. Ghrist, S. Loutzenhiser, and C.E. Wieman, Optics Letters **21**, 290 (1996).

[81] D. Cho, J. of Korean Phys. Soc. **30** 373 (1997).

[82] K.L Corwin, S.J.M. Kuppens, K.W. Miller, and C.E. Wieman, in *1999 Centennial Meeting Bulletin of the American Physical Society* (Atlanta, Ga, 1999).

[83] T. Walker, P. Feng, D. Hoffmann, and R.S. Williamson, Phys. Rev. Lett. **69** 2168 (1992).

[84] D.E. Pritchard, Phys. Rev. Lett. **51** 1336 (1983).

[85] W. Petrich, M.H. Anderson, J.R. Ensher, and E.A. Cornell, Phys. Rev. Lett. **74** 3352 (1995).

[86] D.J. Vieira (vieira@lanl.gov), (private communication).

[87] C. Monroe, W. Swann, H. Robinson, and C. Wieman, Phys. Rev. Lett. **65** 1571 (1990).

[88] T.A. Carlson, F. Pleasonton, and C.H. Johnson, Phys. Rev. **129** 2220 (1963).

[89] J. Behr, in *Proceedings of the Workshop on Experiments and Equipment at Isotope Separators*, edited by L. Buchmann and J. D'Auria (TRIUMF Publications, B.C., 1997).

Ernest Orlando Lawrence Berkeley National Laboratory
One Cyclotron Road | Berkeley, California 94720

Prepared for the U.S. Department of Energy under Contract No. DE-AC03-76SF00098